STACKED INVERTED TOP-EMITTING WHITE ORGANIC LIGHT-EMITTING DIODES

A Dissertation
Presented to
The Academic Faculty

by

Ehsan Najafabadi

In Partial Fulfillment
of the Requirements for the Degree
Doctor of Philosophy in the
School of Electrical and Computer Engineering

Georgia Institute of Technology
DECEMBER 2014

STACKED INVERTED TOP-EMITTING WHITE ORGANIC LIGHT-EMITTING DIODES

Approved by:

Dr. Bernard Kippelen, Advisor
School of Electrical and Computer
Engineering
Georgia Institute of Technology

Dr. Andrew Peterson
School of Electrical and Computer
Engineering
Georgia Institute of Technology

Dr. Steve Kenney
School of Electrical and Computer
Engineering
Georgia Institute of Technology

Dr. Ali Adibi
School of School of Electrical and
Computer Engineering
Georgia Institute of Technology

Dr. Hamid Garmestani
School of Material Science and
Engineering
Georgia Institute of Technology

Date Approved: July 18, 2014

To my family and friends

ACKNOWLEDGEMENTS

First, I would like to thank my advisor, Dr. Bernard Kippelen, for his guidance and scientific advice over the duration of my Ph.D. Further thanks go to my reading and oral defense committee members consisting of Prof. Andrew Peterson, Prof. Ali Adibi, Prof. Hamid Garmestani, and Prof. Steve Kenney for their time investment and feedback. Additional thanks to Dr. John Cressler who served on my proposal committee.

It goes without saying that during my Ph.D. I've benefited greatly from the support and camaraderie of many students and postdoctoral researchers in the Kippelen Research Group. I want to especially thank Mr. Keith A. Knauer, Dr. Yinhua Zhou, and Dr. Wojciech Haske for their professional and personal guidance and help over the years.

The many conversations I've had with friends and colleagues at Georgia Tech and elsewhere were very helpful towards both my research and my career development. Special thanks goes to my friends Dr. Babak Shafei, and Dr. Hossein Sojoudi in this regard. Finally, I am thankful to my parents for their love, guidance, and support throughout my life and during my Ph.D.

TABLE OF CONTENTS

LIST OF TABLES

LIST OF FIGURES

carbons. In b) the un-hybridized, out-of-plan p_z orbitals of the carbon atoms are shown, which overlap as shown in c) where delocalized π-bond is labeled.

and reproducibility was poor.

spectrum.

LIST OF SYMBOLS AND ABBREVIATIONS

α-NPD   N,N′-Di-[(1-naphthyl)-N,N′-diphenyl]-1,1′-biphenyl)-4,4′-diamine
Ag   Silver
Al   Aluminum

Alq_3 tris-(8-hydroxyquinoline)aluminum
Au   Gold
BCP   Bathocuproine
CBP   4,4′-bis(N-carbazolyl)-1,1′-biphenyl
CE   Current Efficacy

EA   Electron Affinity
EML   Emissive Layer
EQE   External Quantum Efficiency
ETL   Electron Transport Material
FIrpic   Bis[2-(4,6-difluorophenyl)pyridinato-C2,N](picolinato)iridium(III)
HAT-CN   1,4,5,8,9,11-hexaazatriphenylene hexacarbonitrile
HOMO   Highest Occupied Molecular Orbital
HTL   Hole Transport Layer
IE   Ionization Energy

$Ir(mpqh)_3$ tris[2-phenyl-4-methylquinoline]iridium(III)

$Ir(ppy)_3$ tris(2-phenylpyridine)iridium(III)
ITO   Indium Tin Oxide
J Current Density
L Luminance
LiF   Lithium Flouride
LUMO   Lowest Unoccuppied Molecular Orbital
mCP   1,3-Bis(N-carbazolyl)benzene

MoO_3 Molydenum Trioxide
PEDOT:PSS   poly(3,4-ethylenedioxythiophene) poly(styrenesulfonate)
TAPC   1,1-bis(4-bis(4-tolyl)-aminophenyl)cyclohexene
TmPyPB   1,3,5-tri(m-pyrid-3-yl-phenyl)benzene)
TpPyPB   1,3,5-tri(p-pyrid-3-yl-phenyl)benzene
V Voltage

SUMMARY

The majority of research on Organic Light-Emitting Diodes (OLEDs) has focused on a top-cathode, conventional bottom-emitting architecture. Yet bottom-cathode, inverted top-emitting OLEDs offer some advantages: they are more convenient to integrate with preferred n-type driving technologies in active-matrix displays; they can be fabricated on opaque substrates or upon flexible substrates that are incompatible with the rigidity of indium tin oxide (ITO); finally, waveguide losses due to emission into substrates can be avoided. Moreover, inverted top-emitting OLEDs are amenable to easy stacking, leading to higher luminance levels at lower current densities than single-unit OLEDs and therefore extended operational lifetimes. Moreover, the increased total thickness of the organic layers yields devices that are more resistant to electrical shorts. Shorts are particularly devastating for large-area panels and it is especially important that the white OLEDs are suitable for use in large-area applications.

In this thesis, the development of high performance green electroluminescent inverted top-emitting diodes is first presented. The challenges in producing an inverted structure are discussed and the advantages of high efficiency inverted top-emitting OLEDs are provided. Next, the transition to a stacked architecture with separate orange and blue emitting layers is demonstrated, allowing for white emission. The pros and cons of the existing device structure is described, with an eye to future developments and proposed follow-up research.

Chapter 1: Introduction

1.1 Overview

Organic light-emitting diodes (OLEDs) are devices comprised of thin-film organic compounds sandwiched between two electrodes. OLEDs have the potential to represent the next generation of lighting and display technology.

Using organic materials in display and lighting applications provides several potential advantages. For one, researchers are seeking techniques to deposit organic materials from a roll-to-roll process at normal pressure and room temperature. Such a technique would pave the way for large-scale, low-cost manufacturing. Furthermore, organic compounds' physical properties can be tuned by synthetic chemists for better customization in select applications. In this regard, OLEDs hold the exciting prospect of one day replacing bulky, inefficient lights and displays with efficient, lightweight, and flexible panels that are environmentally friendly [1, 2]. Figure 1.1(a-b) shows examples of both displays and lighting products available today.

a)   b)

Fig. 1.1. a) Samsung Galaxy SIII. Source: Samsung b) Phillips Lumiblade. Source: Phillips.

In the current market, OLED displays have finally broken into the mainstream. Samsung Electronics Co., Ltd. is pioneering the widespread use of active-matrix OLED (AMOLED), a specific addressing technology for individual pixels in the display, in its line of mobile and tablet

displays (see Fig. 1.1a). Many of the top brand manufacturers (Nokia, HTC, Motorola, LG, and others) have since followed suit. AMOLEDs integrate individual OLED pixels onto a thin-film transistor (TFT) array that act as the driving and switching circuitry. In such displays, OLEDs have many benefits. These benefits include the darkest blacks, fastest response times, highest contrast ratio, wide viewing angle, widest color range, warmest whites, best tracking of the gamma curves, and lowest power consumption of all known display technologies [3]. OLEDs are poised at breaking into larger markets such as televisions and computer monitors. However, problems still remain in producing large-area, defect-free films that can be implemented on a large scale. The market size for OLED display technology is shown is Fig. 1.2.
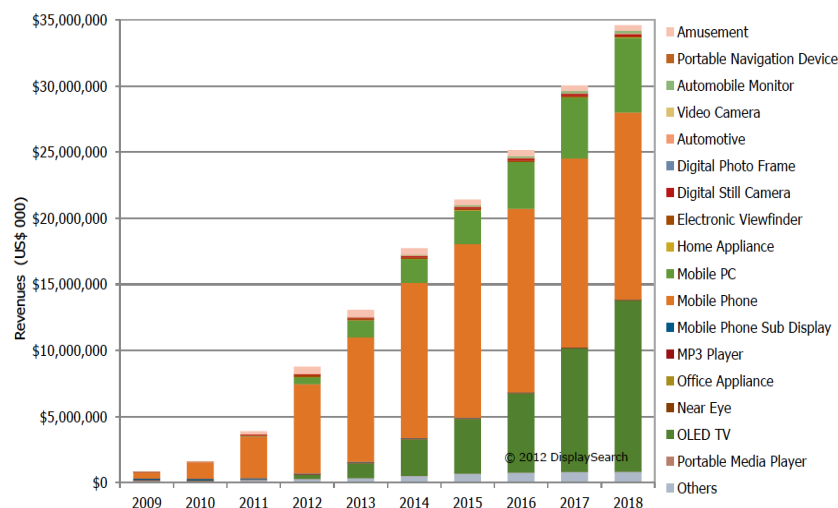
NPD DisplaySearch Quarterly OLED display shipment and forecast report Q1'12

Fig. 1.2. Current and predicted revenues for OLED-related sale versus year. The OLED market in 2018 is predicted to have revenues of nearly $35 billion mainly from OLED TV, mobile PC, and mobile phone elements.

Advances have also been made in solid-state lighting in recent years, but these advances have not yet reached the necessary momentum to launch OLED lighting into the mainstream. The industrialization and commercialization of solid-state OLED lighting has been spearheaded by companies such as Philips, Osram, General Electric (GE), and Panasonic. OLEDs need to

achieve 6" x 6" large area panels with at least 45 lm/W at 1,000 cd/m^2 and 10,000 hour lifetime to be commercially viable [4]. As described in section 3.3.4 of Chapter 3, the luminous power efficacy (in lm/W) is the ratio of light power output to the electrical power input. The International Energy Star Solid-State Lighting Standards would be met with 60 lm/W at 850 cd/m^2 for commercial lighting standards. The eventual goal for such OLED lighting panels is to achieve efficacies greater than 100 lm/W [4].

Osram was the first to produce a "functional table light" source in 2009, which set the stage for other market players (GE and Philips) [4]. Most of the lighting products that exist on the market however today are extremely expensive. For example, the most recent Philips GL350 Lumiblade panels, are 124.5 mm × 124.5 mm, have an efficiency of 16.7 lm/W at 4,000 cd/m^2, and cost $556.00 USD (see Fig. 1.1b) [5].

1.2 Competing Lighting Technologies

Lighting requires a significant portion of the world's economy, and is highly taxing on the ecosystem [6]. It is estimated that it accounts for 19% of total global electricity consumption and costs nearly $234 billion annually. In addition, 1,900 megatons of CO_2 per year are released in the process of generating the energy to run lighting [7].

A theoretical limit of 250 lm/W for a white OLED is stated by Tyan [8], assuming no loss mechanisms are present in the device. When considering all relevant loss channels, this metric is reduced to maximum a possible efficacy of 155 lm/W (at 5,000 cd/m^2) for an all-phosphorescent single stack white OLED [9].

1.2.1 Incandescent bulbs

An incandescent bulb produces light when a tungsten filament, enclosed in a gas-filled or evacuated glass bulb, is electrically heated to a high temperature until it produces light.

Incandescent lamps emit warm white light and have a high color rendition index (CRI) of 100, but are not efficient. It has a quantum efficiency of merely 5% (with a luminous power efficacy typically in the range of 15-20 lm/W), with 95% of the electrical energy being converted to heat. Also, their typical lifetime is below 1,000 h which can be extended to 2,000 h if the bulb is filled with halogen gas [6]. Due to these inefficacies, the incandescent lamp is being phased out in the United States and European Union [10].

1.2.2 Fluorescent tubes

General Electric produced the first fluorescent tubes in the late 1930s that are today the dominant lighting technology in commercial buildings and offices. Fluorescent tubes consist of two electrodes at the end of the tube filled with an inert gas (i.e. argon) and mercury vapor. As current passes through the tube, electrons in the mercury vapor are excited and emit light in the ultra-violet spectrum. The inside of the tube is coated with a fluorescent material that absorbs the UV light and emits light in the visible wavelength regime in a down-conversion mechanism. Fluorescent tubes have a power efficacy of 60–100 lm/W with an efficiency of about 25% [11]. They have a longer lifetime (up to 30,000 h) than incandescent bulbs.

Compact fluorescent lamp (CFL) entered the market in the 1980s. CFLs consists of multiple small fluorescent tubes that fit into the same socket as incandescent bulbs. The main advantage of CFLs is their compatibility with these sockets, in addition to their high efficiency (35-80 lm/W, 20% efficiency), and long lifetimes (6,000–15,000 h). On the other hand, the mercury in both CFLs and regular fluorescent tubes presents a big challenge from an environmental standpoint [11].

1.2.3 Inorganic LEDs

In inorganic LEDs, the light emission is based on recombination of electrons and holes at a p-n junction consisting of semiconducting materials. They were first demonstrated in the 1960s. Inorganic LEDs are a nontoxic alternative to fluorescent lamps and incandescent bulbs and are a direct competitor to OLEDs. Blue-emitting gallium nitride diode LEDs can be coated by a phosphor to produce white LEDs through down-conversion. These white LEDs can have lifetimes up to 100,000 h, efficiencies of 30%, and power efficacies of 100 lm/W. Almost all white LEDs sold today are blue GaN/InGaN LEDs coated with a yellow phosphor [11].

Solid state-LEDs have some drawbacks, keeping them from being dominant in home and office lighting. Advances are still required in efficiency (best efficacy of 100 lm/W, many commercial LEDs are 75 lm/W), heat management, color rendering index (CRI), lifetime, and cost [11]. Nowadays, LED lighting for the household is still expensive.

1.3 Advantages of OLEDs for Lighting and Display Technologies

OLEDs are an emerging technology with many potential advantages over current lighting and display technologies. In terms of lighting, white OLEDs have a broadband emission spectrum that is capable of producing lighting of high quality with excellent CRI (see section 3.3.7 and Appendix C4). In addition, OLEDs' luminance can be easily changed by changing the operating current. This is in contrast to fluorescent lamps that can only be in fully on or off states. Since OLEDs are diffuse light sources, they can be viewed directly without eye discomfort in contrast to conventional point sources of light, e.g. incandescent lamps, halogen lamps, and LEDs. OLED light sources are thin, flat, and lightweight and can be transparent or mirrored that can therefore be attractive design elements.

In terms of displays, OLEDs are able to produce deep, dark blacks leading to outstanding picture quality. Deeper blacks allow for higher contrast ratios and richer colors leading to more crisp displays. In the market, what is branded as LED TVs is actually composed of an LED backlight shining behind an LCD panel. For LCD displays, a contrast ratio of up to 15,000:1 can be achieved, while for OLEDs this metric can be enhanced to anywhere between 65,000:1 - 1,000,000:1. The contrast ratio is the ratio of the luminance of the brightest color to that of the darkest color that a display is capable of producing. In fact, LCD screens lose contrast in high temperature, and lose luminance in low temperature environments. Also, since OLEDs pixels produce light instead of filtering the LED backlight as LCD screens do, they then have large fields of view (about 170 degrees).

1.4 OLED General Structure and Working Principle

OLEDs consist of tens of nanometer-thin organic semiconductor films sandwiched by two electrodes. With the application of a voltage resulting in an electric field in the device, electrons and holes are injected into the organic layers from the cathode and anode, respectively. These carriers travel towards the electrode of opposite polarity. When charges of opposite type meet, they form bound electron-hole pairs held together by electrostatic Coulomb forces. This aggregate is referred to as exciton, and it can relax and recombine to emit either light or heat (see Fig. 1.3).
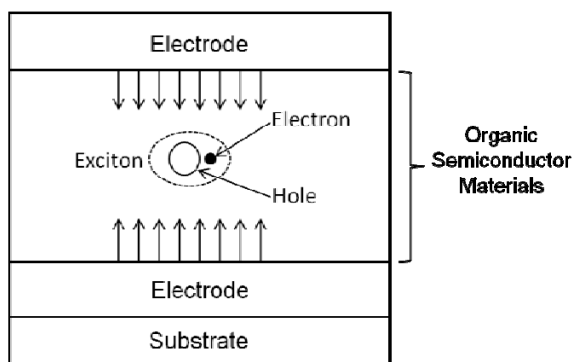
Fig. 1.3. Representative OLED structure showing electrodes injecting carriers (arrows), and the formation of an exciton in organic material.

The organic semiconductors themselves are composed of π-conjugated molecules, with alternating single and double bonds, whose delocalized π-electrons lead to electrical conduction [12] (see Fig. 1.4). Many organic semiconductors have optical bandgap energies in the rage of 1.5 to 3.5 electron volts (eV), which can lead to the emission of photons in the visible spectrum (400 to 750 nm). Furthermore, chemists can synthesize organic compounds with varying molecular structure to tune electrical and optical properties.

4,4'-Bis(9-carbazolyl)-1,1'-biphenyl (**CBP**)
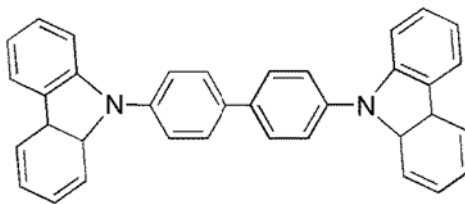
Fig. 1.4. The chemical structure of a well known organic semiconducting material, 4.4'-Bis(9-carbazolyl)-1,1'biphenyl (CBP), showing π-conjugation in the form of alternating single and double bonds.

The electrical properties of organic molecules can be characterized by their highest occupied molecular orbital (HOMO) and lowest unoccupied molecular orbital (LUMO) levels. The HOMO and LUMO levels are a property of an isolated molecule. In bulk material there is a

distribution of HOMO and LUMO levels which is analogous to the valence and conduction bands of inorganic semiconductors (e.g. silicon and germanium), respectively. In first approximation, the edge of the HOMO distribution of a solid thin-film can be identified with the ionization energy (IE). When measured experimentally, the IE is the energy (typically given in eV) necessary to remove an electron from the bulk material. The LUMO level, if experimentally determined in bulk materials is also commonly described in terms of the electron affinity (EA). Strictly speaking, however, the terminology is interchangeable in the gas phase, but is nevertheless sometimes used loosely in literature reports.

Electrical device such as an OLED operate by flowing electrical current through the films of organic compounds. This current flow is achieved by physical contact with electrodes that inject charge into organic semiconductors at an interface. The electrodes are mainly metals or transparent conductive oxides (TCOs) (i.e., indium tin oxide, ITO). Electrodes are often characterized by a parameter known as the work function. The work function represents the amount of energy required to move an electron from the surface of the solid to a point infinitely far away. Common metals (such as Au, Ag, Al, and Ca) and semi-metals (such as ITO, zinc oxide (ZnO) and other TCOs) that are used widely in organic electronics have work function values in the range of 2-5.5 eV. If the value of the HOMO level (or alternatively, the IE) of an organic material is similar to that of the work function of commonly used anodes, the semiconducting material can be used as a hole transporting layer (HTL) since hole injection in the semiconductor is not impaired by a large energy barrier height. If the value of the LUMO (or alternative, the EA) is close to that of the work function of commonly used cathodes, the organic semiconductor can be used as an electron transporting layer (ETL). Refer to Fig. 1.5 for a diagram with these definitions.
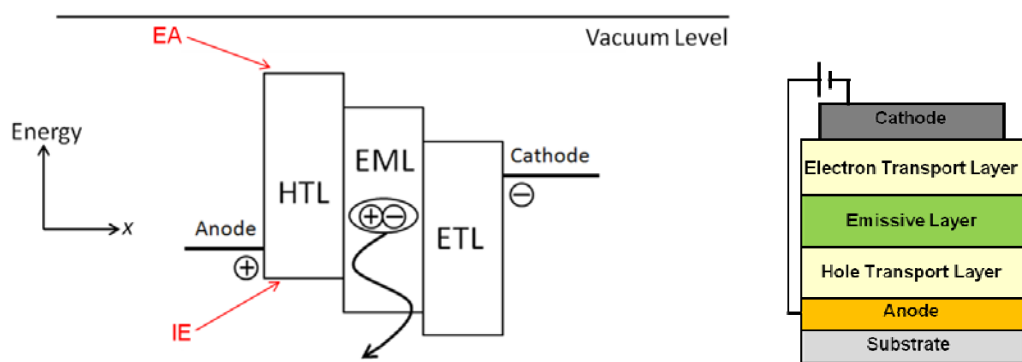
Fig. 1.5. Diagram showing relative energetic levels (IE and EA) of various organic layers in an OLED and exciton formation in the emissive layer.

Over time OLED device architectures have become increasingly complex, incorporating additional organic layers that optimize charge injection and transport through the device. This has led to devices with higher efficiency and lower turn-on voltages than earlier versions [13]. A hole-injection layer (HIL) and an electron-injection layer (EIL) are sometimes placed between the electrodes and the corresponding transport layers. These additional layers improve the injection of holes and electrons, respectively, through modification of the neighboring electrode's work function. The function of the HTL and ETL is to preferentially transport one carrier type into the emissive layer (EML) of the OLED. The EML facilitates the formation and recombination of excitons leading to photon emission [14]. As such the EML material is generally conductive to both carrier types.

In recent times, the development of phosphorescent emitters has led to OLEDs with higher device efficiencies and performance. Holes and electrons are fermions with spin states of either +1/2 or -1/2. When they meet in the EML to form excitons, a statistical mixture of singlet (anti-parallel electron spins) and triplet (parallel spins) states are formed leading to a distribution of 25% singlet and 75% triplet states. With fluorescent emitters, radiative emission can occur only from the singlet states due to spin conservation laws, severely limiting the potential device efficiency of the OLEDs [15]. Phosphorescent emitters on the other hand, collect from both the

triplet and singlet states through the mechanism of spin-orbit coupling. By mixing the singlet and triplet states, the spin selection rules are partially lifted and these emitters are able to emit efficiently from the lowest energy excited state allowing for 100% internal quantum efficiency [16]. These emitters were developed by Forrest, Thompson and co-workers in 1998 and are based on heavy metal organometallics (such as iridium and platinum). This does not directly translate into a device with 100% external quantum efficiency however, because the generated light is subject to loss mechanisms in exiting the device [17].

1.4.1 Conventional vs. Inverted OLEDs

Most of the research and development on OLEDs has been focused on geometries where the anode consists of a TCO on the substrate, followed by organic layers, and then a top metal cathode [18-24]. Such a structure is referred to as a conventional OLED architecture. This is opposed to inverted OLEDs where the positions of the anode and cathode are reversed (See Fig. 1.6).

a)   b)
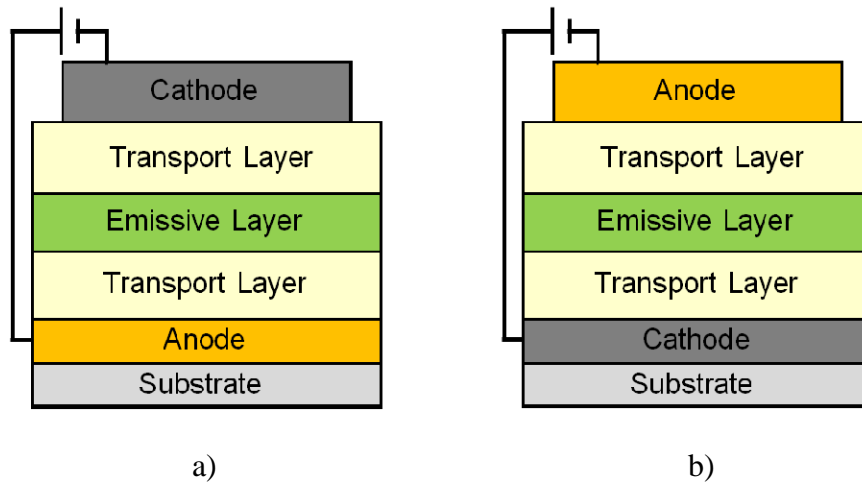
Fig. 1.6. Diagram showing difference between a) conventional and b) inverted OLEDs.

In OLED displays the individual pixels are turned-on by driving thin-film transistors. For instance, AMOLED pixels are fabricated atop n-type thin-film transistors (TFTs). These TFTs

are made of amorphous silicon (a-Si) deposited on a glass substrate by plasma-enhanced chemical vapor deposition (PECVD). Inverted OLEDs offer industrial advantages since they are more easily integrated with the n-type transistor electronics. For instance, a-Si TFTs are generally n-type and polycrystalline silicon (poly-Si) TFTs, n-type TFTs usually have higher carrier mobility and thus lower operation voltage.

To further explain the engineering advantages of inverting OLEDs' architecture, Fig. 1.7a shows how conventional OLEDs could be connected to an n-type driving transistor. In this case, the OLED would connect its anode to the source of the transistor. Note however, that in this configuration, the transistor acts as a source follower. This is because the OLED voltage follows the source voltage of the transistor. The transistor's gate voltage is a sum of the transistor gate-to-source voltage (V_{GS}) and the OLED voltage. Hence, the transistor current is not independently controlled by the gate voltage any more. Thus degradation of either the transistor or the OLED will directly affect the operation of the other, leading to varying OLED brightness. For OLED displays a-Si TFTs are often used. The voltage applied to the a-Si transistor induces a degradation of the a-Si over time, leading inevitably to requiring more complex driving circuits that include compensation functions.
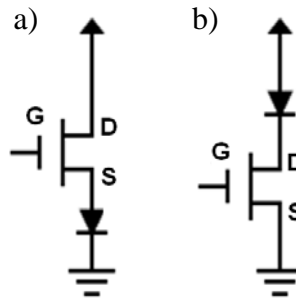
Fig. 1.7. Circuit diagram of an n-type transistor connected to a) conventional and b) an inverted OLED.

In an inverted OLED, the cathode can be simply connected to the drain of the driving n-type TFT (Fig. 1.7b). The transistor then acts instead like a voltage-controlled current source (VCCS). This is because the current supplied to the OLED is controlled by the gate voltage independent of the OLED's operation. Thus the combined benefits of decoupled driving TFT and OLED performance and better integrability with ubiquitous, high performance n-type TFTs can be realized [25] with increased simplicity.

1.4.2 Top-Emission Versus Bottom-Emission OLEDs

High efficiencies and long lifetimes resulting from decades of research have been achieved in conventional, bottom-emitting OLEDs. However, they are nevertheless constrained by their geometry. The main limitation for bottom-emission arises from having a TCO on a transparent substrate. This leads to emitted light getting trapped in both TCO and substrate modes, reducing light extraction. Some estimates state that as much as 80% of internally generated light can be lost as a result [17]. Optical outcoupling lenses provide one method of recovering some lost light. However, they are difficult and costly to fabricate, and complicate the device structure considerably.

Top-emitting OLEDs, on the other hand, have light coming directly out of the semi-transparent anode (Fig. 1.8). In this case, waveguiding modes are avoided, but if a thin metal anode is used absorption losses are introduced. More importantly, since the light exists through the top contact, a whole host of opaque substrates such as metal foils can be used. Finally, optical outcoupling can be achieved simply by depositing an organic film on top of the anode instead of expensive microlens arrays.

Semi-transparent Electrode		Reflective Electrode
Organics		Organics
Reflective Electrode		Semi-Transparent Electrode
Substrate		Substrate

a)   b)
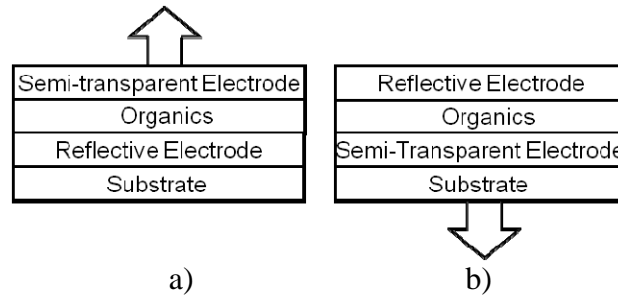
Fig. 1.8. Diagram showing the difference between top-emitting OLED and bottom-emitting OLEDs.

Another benefit of top-emitting OLEDs is an ability to be built directly upon driving circuitry. This simplifies fabrication and increases the effective emission area of OLED pixels in displays (see Fig. 1.9). Since more light is produced per area, the OLEDs can be driven at lower powers, saving both energy and extending device lifetimes.
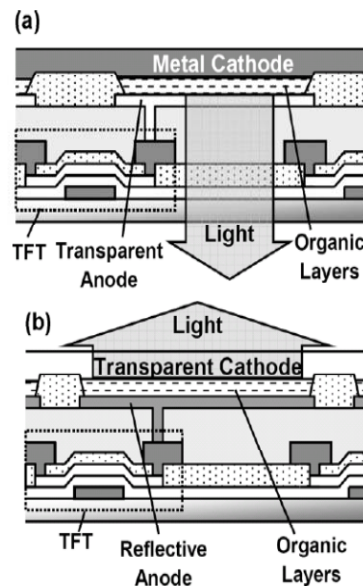
Fig. 1.9. Effective emission area of OLED pixels in displays is shown to increase in the top-emitting architecture in (b) versus the bottom-emitting architecture (a). Reproduced from [25].

For inverted, top-emitting OLEDs there is a final added benefit. The brittle ITO anode can be replaced with a thin metal cathode allowing for use on flexible substrates. Flexible substrates enable OLEDs that can be fabricated into a variety of form factors. They can find

13

application in settings where rigid fixtures are not useable. From a manufacturing standpoint, flexible OLEDs are compatible with roll-to-roll fabrication which can reduce costs and processing times dramatically.

With all these advantages, it is important to note the potential drawbacks of having top-emitting OLEDs based on two metal electrodes. The metal electrodes sandwiching a submicron-thick organic layer stack form a microcavity [26], which introduces a spectral shifting and narrowing to the emission profile of the OLEDs. This reduces the uniformity of the light as a function of viewing angle, and the emission of the devices are no longer be considered as Lambertian. This furthermore makes measuring these devices more difficult since commonly used metrics such as external quantum efficiency (EQE) and power efficacy (lm/W) inherently assume Lambertian emission. Thus, more comprehensive integrating sphere measurements that capture all emitted light must be used to report these specific performance metrics.

1.5 Scope and Organization of Thesis

This thesis is structured as follows. Chapter 2 reviews the basic background on organic semiconductors, OLED device physics, fluorescent vs. phosphorescent emitters, and optical loss mechanisms. Chapter 3 gives an overview of the performance parameters for OLED characterization, the test setup for OLED measurements.

In Chapter 4 we present the key research results obtained on inverted top-emitting OLED devices. A more specific description of history and state-of-the-art for electrophosphorescent inverted top-emitting OLEDs is first discussed in more detail. This is followed by a discussion of how higher efficiencies can be achieved in an OLED device structure where an Al/lithium fluoride cathode is employed on the bottom of the device. In addition, a novel anode consisting

14

of 1,4,5,8,9,11-hexaazatriphenylene hexacarbonitrile (HAT-CN)-modified Ag is shown to act as

an efficient hole-injecting electrode for application in inverted top-emitting OLEDs. Finally, we

demonstrate that such OLEDs can be fabricated on recyclable carbon nanocellulose (CNC)

substrates, demonstrating the versatility of this inverted top-emitting architecture. In chapter 5, a

stacked inverted top-emitting white OLED device comprising of individual orange and blue

subunits is demonstrated for the first time. A discussion for further optimization and

characterization of such a white OLED is discussed, along with some outstanding issues such as

lifetime and reproducibility.

     Finally, Appendix A goes into more detail about the materials used in the inverted top-

emitting OLEDs. In Appendices B and C a review of the electroluminescence spectral

measurements, color coordinate and color rendering index determination, and a brief discussion

on the difficulties associated with some of these measurements in an inverted top-emitting

OLED configuration are given.

1.6 References

[1] T.S. Perry, G. Zorpette, Oled TV arrives [2013 Tech To Watch], Spectrum, IEEE, 50 (2013) 46-47.
[2] R. Coehoorn, V. Elsbergen, C. Verschuren, High Efficiency OLEDs for Lighting Applications, in: E. Cantatore (Ed.) Applications of Organic and Printed Electronics, Springer US2013, pp. 83-100.
[3] O. Association, OLED Displays and Lighting – 2010/2011 State of the Art, 2011.
[4] R. Pode, B. Diouf, Solar Lighting, Springer London, Limited, 2011.
[5] T. Dobbertin, O. Werner, J. Meyer, A. Kammoun, D. Schneider, T. Riedl, E. Becker, H.H. Johannes, W. Kowalsky, Inverted hybrid organic light-emitting device with polyethylene dioxythiophene-polystyrene sulfonate as an anode buffer layer, Appl. Phys. Lett., 83 (2003) 5071-5073.
[6] P.G. Flesch, Light and Light Sources: High-Intensity Discharge Lamps, Physica-Verlag, 2007.
[7] N. Ide, H. Tsuji, N. Ito, H. Sasaki, T. Nishimori, Y. Kuzuoka, K. Fujihara, T. Miyai, T. Komoda, High-performance OLEDs and their application to lighting, 2008, pp. 705110-705119.
[8] Y.-S. Tyan, Organic light-emitting-diode lighting overview, Journal of Photonics for Energy, 1 (2011) 011009-011015.
[9] S. Reineke. "Controlling Excitons - Concepts for Phosphorescent Organic LEDs at High Brightness." TU Dresden (Dissertation) (2009).

[10] D.S. Ginley, D. Cahen, Fundamentals of Materials for Energy and Environmental Sustainability, Cambridge University Press, 2011.

[11] C.J. Humphreys, Solid-state lighting, Mrs Bulletin, 33 (2008) 459-470.

[12] M. Pope, C.E. Swenberg, Electronic processes in organic crystals and polymers, Oxford University Press, 1999.

[13] M.G. Helander, Z.B. Wang, J. Qiu, M.T. Greiner, D.P. Puzzo, Z.W. Liu, Z.H. Lu, Chlorinated Indium Tin Oxide Electrodes with High Work Function for Organic Device Compatibility, Science, 332 (2011) 944-947.

[14] S.F. Chen, L.L. Deng, J. Xie, L. Peng, L.H. Xie, Q.L. Fan, W. Huang, Recent Developments in Top-Emitting Organic Light-Emitting Diodes, Advanced Materials, 22 (2010) 5227-5239.

[15] M.E. Thompson, P.E. Burrows, S.R. Forrest, Electrophosphorescence in organic light emitting diodes, Current Opinion in Solid State and Materials Science, 4 (1999) 369-372.

[16] M.A. Baldo, D.F. O'Brien, Y. You, A. Shoustikov, S. Sibley, M.E. Thompson, S.R. Forrest, Highly efficient phosphorescent emission from organic electroluminescent devices, Nature, 395 (1998) 151-154.

[17] C. Adachi, M.A. Baldo, M.E. Thompson, S.R. Forrest, Nearly 100% internal phosphorescence efficiency in an organic light-emitting device, Journal of Applied Physics, 90 (2001) 5048-5051.

[18] T. Dobbertin, M. Kroeger, D. Heithecker, D. Schneider, D. Metzdorf, H. Neuner, E. Becker, H.H. Johannes, W. Kowalsky, Inverted top-emitting organic light-emitting diodes using sputter-deposited anodes, Applied Physics Letters, 82 (2003) 284-286.

[19] T. Dobbertin, O. Werner, J. Meyer, A. Kammoun, D. Schneider, T. Riedl, E. Becker, H.H. Johannes, W. Kowalsky, Inverted hybrid organic light-emitting device with polyethylene dioxythiophene-polystyrene sulfonate as an anode buffer layer, Applied Physics Letters, 83 (2003) 5071-5073.

[20] C.W. Chen, C.L. Lin, C.C. Wu, An effective cathode structure for inverted top-emitting organic light-emitting devices, Applied Physics Letters, 85 (2004) 2469-2471.

[21] M. Thomschke, S. Hofmann, S. Olthof, M. Anderson, H. Kleemann, M. Schober, B. Lussem, K. Leo, Improvement of voltage and charge balance in inverted top-emitting organic electroluminescent diodes comprising doped transport layers by thermal annealing, Applied Physics Letters, 98 (2011) 083304.

[22] K.H. Kim, S.Y. Huh, S.M. Seo, H.H. Lee, Inverted top-emitting organic light-emitting diodes by whole device transfer, Organic Electronics, 9 (2008) 1118-1121.

[23] Q. Wang, F.X. Wang, X.F. Qiao, D.G. Ma, Lead(IV) dioxide: an effective electron injection material to realize high-efficiency inverted top-emitting organic light-emitting diodes, Semiconductor Science and Technology, 24 (2009) 105027.

[24] M. Kroger, T. Dobbertin, D. Schneider, T. Rabe, E. Becker, H.H. Johannes, W. Kowalsky, Highly efficient guest-host-systems for hybrid inverted organic light-emitting diodes with sputtered indium-tin-oxide anodes, Organic Light-Emitting Materials and Devices Viii, 2004, pp. 143-152.

[25] C.C. Wu, C.W. Chen, C.L. Lin, C.J. Yang, Advanced Organic Light-Emitting Devices for Enhancing Display Performances, Journal of Display Technology, 1 (2005) 248-266.

[26] T.-Y. Cho, C.-L. Lin, C.-C. Wu, Microcavity two-unit tandem organic light-emitting devices having a high efficiency, Applied Physics Letters, 88 (2006) 111106-111103.

Chapter 2: OLED Device Physics

In this chapter, a brief overview of the relevant physical concepts relating to organic semiconductor and OLED device physics will be given. Some optical loss mechanisms such as waveguiding and surface plasmon mode losses are discussed. Finally, a brief description of OLED degradation mechanism is also given.

2.1 Organic Semiconductors

Organic semiconductors are comprised of carbon-based materials which have electrical conductivities greater than insulators (such as glass) but less than conductors (such as metals). This conductivity is a physical property that depends on a combination of intrinsic factors, including the semiconductor's molecular structure, the bulk phase morphology of films formed from such molecules, and extrinsic properties such as the presence of solid-state or gaseous dopants, impurities and defects. Many organic semiconductors have optical bandgap energies in the range of 1.5 to 3.5 eV, which can lead to the emission of photons in the visible spectrum (400 to 750 nm) [1]. Furthermore, chemists can synthesize organic compounds with varying molecular structure to tune the electrical and optical properties of these materials for a given application.

The bonding in a small molecule or polymer backbone of the semiconductor consists of alternating single and double carbon-carbon bonds. The four outer orbitals of a carbon atom that participate in bonding are the s, p_x, p_y, and p_z orbitals, as seen in Fig. 2.1. From these orbitals, hybrid orbitals can be formed that are linear combinations of the s orbital with a number of p orbitals varying between one and three. Such hybrid orbitals are referred to as sp^1, sp^2, or sp^3. Following that notation, the superscript refers to the number of p orbitals that are hybridized. Of particular interest are sp^2 orbitals where three orbitals T_1, T_2, and T_3 are a linear combination of the s orbital and the two orbitals p_x and p_y:

$$T_1 = (1/\sqrt{3})s + (\sqrt{2}/\sqrt{3})p_x \tag{2.1}$$

$$T_2 = (1/\sqrt{3})s - (1/\sqrt{6})p_x + (1/\sqrt{2})p_y \tag{2.2}$$

$$T_3 = (1/\sqrt{3})s - (1/\sqrt{6})p_x - (1/\sqrt{2})p_y \tag{2.3}$$

The three T_i orbitals are geometrically oriented in the x-y plane, with one orbital pointing in the x direction, and the two other orbitals in the directions forming an angle of $120°$ with the x axis (see Fig. 2.2a). The remaining unhybridized fourth p_z orbital points in the z direction, perpendicular to the hybrid orbital plane (see Fig. 2.2b). In organic semiconductors, double bonds form between two carbon atoms when hybridized carbons bond through the sp^2 hybrid orbitals and the p_z orbitals on adjacent carbons bonds overlap. Since the p_z-orbitals are out-of-plane, this bonding pattern yields a delocalized electron cloud (see Fig. 2.2c). These highly delocalized electrons confer unique electrical and optical processes in organic semiconducting materials [2].
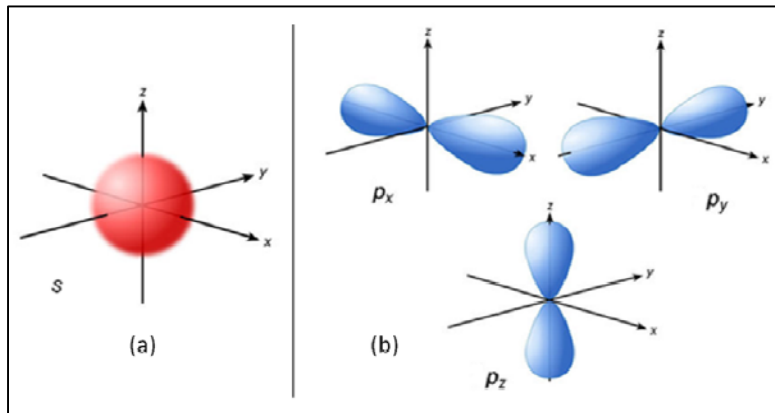
Fig. 2.1. The four outer orbitals of a carbon atom that participate in bonding: a) s, and b) p_x, p_y, and p_z orbitals. Reproduced from [3].
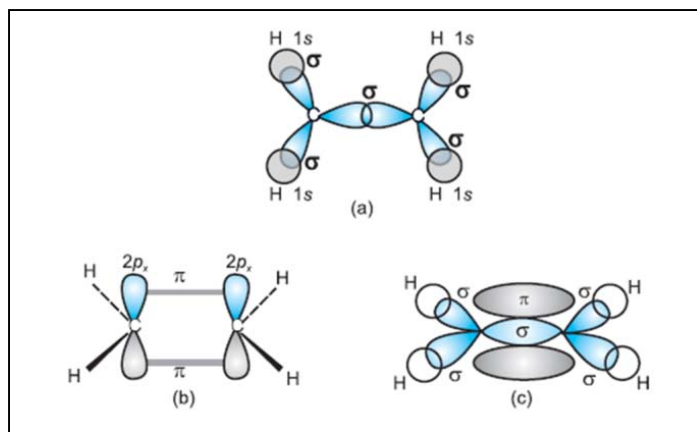
Fig. 2.2. Schematic for bonding in the ethane molecule. In a) the hybridized sp^2 orbitals of each carbon atom is shown, which forms sigma bonds with the $1s$ orbital of the Hydrogen atoms and σ-bond with between carbons. In b) the unhybridized, out-of-plan p_z orbitals of the carbon atoms are shown, which overlap as shown in c) where delocalized π-bond is labeled. Reproduced from [4].

The electrical properties of organic semiconductor thin films can be characterized by their ionization energy (IE), electron affinity (EA), carrier mobility, and density of free carriers. Individual organic semiconductor molecules can be characterized by their highest occupied molecular orbital (HOMO) and lowest unoccupied molecular orbital (LUMO). When molar quantities of such molecules are considered in a solid-state system, there is a distribution of HOMO and LUMO levels. The edge of this distribution for the HOMO level is often described in terms of the IE. For simplicity, a parallel can be drawn between the IE and the valence band energy of inorganic semiconductors. When measured experimentally, the IE is the energy (typically given in eV) necessary to remove an electron from the bulk material. The LUMO level, if experimentally determined in bulk materials is also commonly described in terms of the EA. As can be derived from the Koopmans' theorem, the HOMO energy of a molecule can provide a rough estimate of the IE of a solid film formed from such molecules and the molecular LUMO energy identified with the EA of the corresponding solid film [5]. The value of the EA can be assimilated with the conduction band energy of an inorganic semiconductor (e.g. silicon

and germanium). In addition, carrier mobility quantifies charge transport in bulk organic semiconductors. The transport can be described as a charge hopping process between molecules, and scattering losses in this process lead to low mobility values, which can range from 10^{-7} - 10 cm^2/V-s.

The organic compounds used in OLEDs are often amorphous semiconductors and can be classified into two major types based on molecular weight: small molecule and polymer. Semiconducting small molecules have a molecular mass less than 1000 Daltons (this is relative to the mass of the isotope ^{12}C (carbon 12, which is 12 Daltons), and are typically deposited by sublimation through thermal evaporation of powder materials by sublimation under high-vacuum. Some traditional examples include polycyclic aromatic compounds such as pentacene, anthracene, and rubrene. Polymeric organic semiconductors have greater molecular weight and can easily form films of high uniformity from spin-coating from solution and are more compatible with techniques such as inkjet printing [6] and screen printing [7], and electropolymerization. Common semiconducting polymers include polythiophene, polyphenylene vinylene (PPV), and polyacetylene. Representative chemical structures of both small molecule and polymer based organic semiconductors are shown in Fig. 2.3.
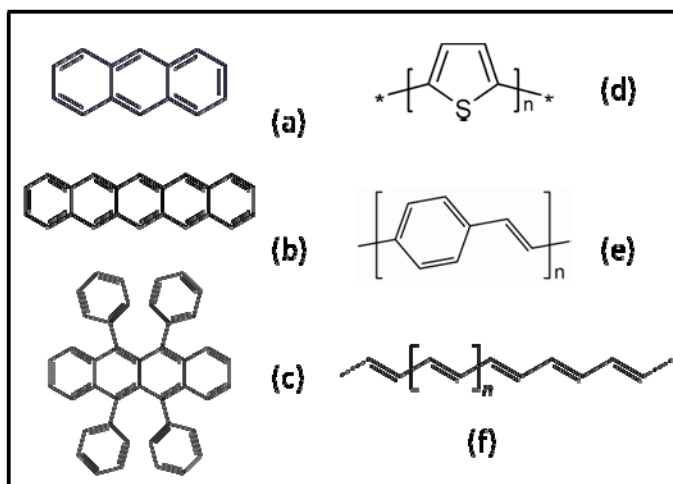
Fig. 2.3. Some common small-molecule organic semiconductors: a) anthracene, b) pentacene, c) rubrene, and polymer organic semiconductors: d) polythiophene, e) polyphenylene vinylene (PPV), f) polyacetylene.

Organic semiconductors offer a variety of advantages over their inorganic counterparts. These include tunability of molecular structures to achieve desired electro-optical properties, ease of material processing and deposition to pave the way to potentially low-cost manufacturing in large area applications [8-10], and sensitivity to chemical agents for sensor applications [11].

2.2 OLED Operating Theory

As mentioned in section 1.4, OLEDs emit light when a voltage is applied to electrodes that bias organic semiconducting thin films, creating an electric field. The electrodes inject holes and electrons into the organic layers from the anode and cathode, respectively.

If there is no external applied bias applied to the OLED, the anode and cathode, having different work functions, contact across the organic thin films and produce an internal electric field leading to a built-in contact potential. Carriers can propagate through the organic layers if a negative voltage is applied to the cathode and if this voltage is greater than the built-in potential. When electrons and holes meet in the emissive layer, they can form excited states in which

21

electrons and holes bound by Coulomb interactions form excitons which decay radiatively and lead to electroluminescence [12]. With effective choice of organic layers based on minimizing the barriers to carrier injection and optimizing transport, recombination can occur mainly in the emissive layer of the OLED, leading to high luminance and device efficiency.

2.2.1 Charge Injection

Charge injection from electrodes into organic materials is a complex phenomenon and no agreed universal physical description exists yet. There are several reasons for this, including the charge distribution at the metal-organic interface, its influence by chemical reactions, and morphological characteristics of organic semiconductors. This theoretical difficulty is compounded by the experimental difficulty of investigating a buried interface [13]. The charge injection process is usually divided into two regimes: the **injection limited current (ILC)** and the **space-charge limited current (SCLC)**.

Let's first consider the most relevant parameter of metal electrodes used in OLEDs, the work function. The **work function** ϕ_m is defined as the energy required to remove an electron from the bulk of conductor to a distance just outside the surface [14]. Equivalently the work function is equal to the difference in potential energy of an electron between the local vacuum level E_{vac} (in eV) and the Fermi level, E_F (also in eV),

$$e\phi_m = E_{vac} - E_F \tag{2.4}$$

If E_{vac} varies across the different faces of a single crystal, ϕ_m will also vary, but average values are used when designing OLED electrodes [15]. For effective OLED design, the anode should have a work function that is close to the IE of common HTLs. Alternatively the cathode should have a work function similar to the EA of common ETLs. This is to ensure that the barriers for

22

the hole injection into the HOMO and electron injection into the LUMO are small (i.e. not greater than 0.5-1.0 eV).

When charges move from one material to another, they face an energetic barrier, ϕ_B. Let's consider the case of a low work function metal injecting into the conduction band level of an inorganic semiconductor, which is lower in energy than the metal work function (see Fig. 2.4). In the Schottky-Mott limit, the vacuum level of the semiconductor and metal align. This leads to the formation a region of net space charge at the metal-semiconductor interface. No charge is transferred across the interface, and the semiconductor bands bend because of the potential difference. The Schottky barrier for electrons is then given by the difference between the work function of the metal and the electron affinity of the semiconductor [16].
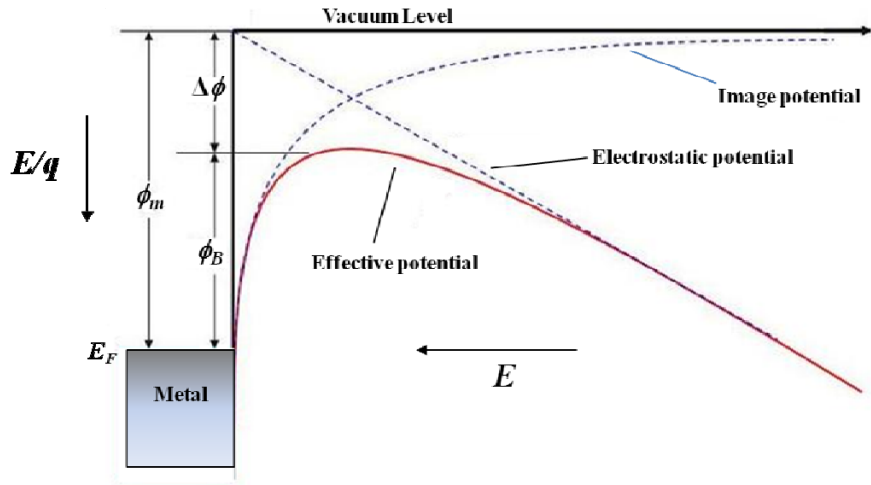
Fig. 2.4. Barrier height lowering by image charge potential, where ϕ_m is barrier in the absence of the image charge effect, ϕ_B is the barrier with the image charge effect, and $\Delta\phi$ is the change in the barrier height. Adapted from [17].

However, in organic semiconductors, the Schottky-Mott limit is rarely observed. Instead, when the metal electrode and organic materials make contact, some electrons are transferred from the metal to the organic semiconductors trap states by diffusion [18]. When one such

electron is at distance x away from the metal surface it induces a charge of opposite polarity at $-x$. Therefore the potential experienced by the electron due to its image charge is

$$\phi_{image} = \frac{q^2}{16\pi\epsilon x} \tag{2.5}$$

where $\epsilon = \epsilon_0\epsilon_r$ is the permittivity of the material and ϵ_0 is the permittivity of free space (8.854×10^{-12} F/m), and q is the elementary charge (1.60×10^{-19} C). The energy barrier ϕ_B experience by the electron is then given by

$$\phi_B = \phi_m - \frac{q}{Ex_m} - \frac{q^2}{16\pi\epsilon x_m} \tag{2.6}$$

where ϕ_m is metal work function, the second term is a electrostatic potential reduction term, and x_m is the distance where the sum of the field and image charge term has a maximum, and can be shown to be given by

$$x_m = \sqrt{\frac{q}{16\pi\epsilon E_{max}}} \tag{2.7}$$

The total barrier change can be given as

$$\Delta\phi = -\sqrt{\frac{q^3 E}{4\pi\epsilon}} \tag{2.8}$$

Fig. 2.4 summarizes all of these quantities in an energy diagram.

In addition to the image and electrostatic potential which change the barrier for charge injection from metals to organic semiconductors, interface dipoles are another way in which this interfacial barrier can be changed. The interface dipole can form as a result of chemical bond formation, charge transfer, oriented films of polar molecules, or a rearrangement of the surface image potential [19]. If the interface dipole has its negative pole pointing toward the organic material and its positive pole toward the metal electrode, it will increase the metal work function

24

and increase the HOMO energy of the organic layer by adding an electrostatic energy. In this case, barrier to hole injection is reduced as shown in Fig. 2.5. If the direction of the interface dipole is reversed, then it will instead reduce the barrier to electron injection. Depending on the nature of the electrode (anode vs. cathode) and the organic semiconductor (relative HOMO/LUMO level energies), the barrier reduction can have a desirable or undesirable effect on the charge balance and thus performance of the device.
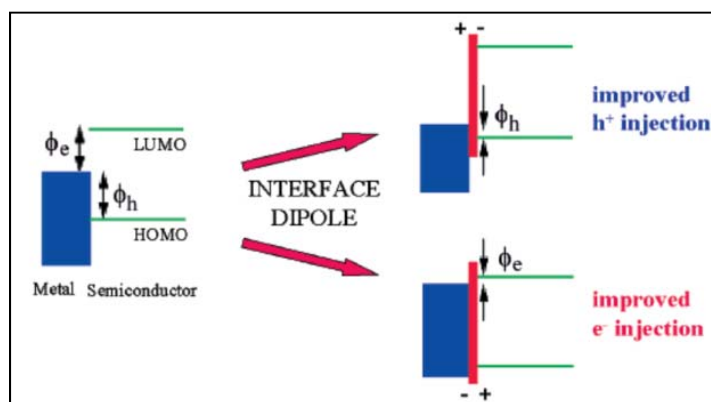
Fig. 2.5. The effect of an interface dipole on the energy level alignment of a metal-organic interface. Reproduced from [19].

2.2.2 Injection Limited Current

In the injection limited current (ILC) regime, the barrier to injection from the metal to the semiconductor is non-negligible (i.e. 0.25-0.3 eV and greater). In this regime charge carrier injection is modeled by either **Fowler-Nordheim (FN) tunneling**, or the **Richardson-Schottky (RS) thermionic-emission**.

For carrier injection from metals into organic semiconductors with an interfacial barrier height on the order of 0-0.3 eV and lower electric fields (less than 10^5 V/cm), Richardson-Schottky (RS) emission can be used. This model describes injection as a thermally activated process (also known as the thermionic injection) and is governed by the equation

$$J = A^* \cdot T^2 \cdot e^{\frac{-\phi_B}{kT}} \cdot \left(e^{\frac{qV}{nkT}} - 1 \right) \qquad (2.9)$$

where A^* is the Richardson constant (in units of A/m^2 K^2), T is the temperature (in K), ϕ_B is again the barrier height, k is the Boltzmann constant (8.617×10^{-5} eV·K^{-1}), and n is the ideality factor (dimensionless) [17].

Scott [20] modified the thermionic injection model by taking account of image charge and invoking detailed balance to more accurately determine the injection current. In his model,

$$J = 4N_0\psi^2 e\mu E e^{\frac{-q\Phi_B}{kT}} e^{f^{1/2}} \qquad (2.10)$$

where N_0 is the density of chargeable sites in the organic material interface (in cm^{-3}), μ is the mobility of the organic semiconductor (in cm^2/V·s), E is the applied electric field (in V/m) which is assumed to be constant, f is the reduced electric field and is given by

$$f = \frac{qEr_C}{kT} \qquad (2.11)$$

and

$$r_c = \frac{q^2}{4\pi\epsilon\epsilon_0 kT} \qquad (2.12)$$

and is the Coulomb radius (in m) (see section 2.3.2), and

$$\psi = f^{-1} + f^{-\frac{1}{2}} - f^{-1}\left(1 + 2f^{\frac{1}{2}} \right)^{\frac{1}{2}} \qquad (2.13)$$

This formalism takes into account the influence of the image charge through the reduced electric field f.

For the case of large barrier heights (larger than 0.3 eV) and high electric fields (on the order of 10^6 V/cm) at the metal-organic interface, it is theorized that FN tunneling current can describe the charge injection:

$$J = \frac{q^3 V^2 m_0}{8\pi \phi_B m^*} \exp\left(-\frac{4\sqrt{2m^*}\phi_B^{\frac{3}{2}}}{3hqV}\right) \tag{2.14}$$

where V is the applied voltage (in V), q is again the elementary charge, m_0 is electron mass in

free space (9.11×10^{-31} kg), ϕ_B is the barrier height (in eV), h is the Plank constant (4.135×10^{-15}

eV-s), and m^* is the effective electron mass (in kg) in the organic semiconductor [17].

2.2.3 Space-Charge Limited Current

For low applied voltages, the charge transport in organic semiconductors in one

dimension is given by the ohmic drift current:

$$J = n_0 q\mu \frac{V}{d} \tag{2.15}$$

where q is the elementary charge, n_0 is the charge carrier density, μ is the charge mobility, V

the applied voltage, and d is the thickness of the organic semiconducting layer. If we assume that

such an ohmic contact can supply an infinite number of charges at higher applied electric fields,

then more charges are injected than can be transported and excess charges start building up in the

semiconductor. This is the SCLC regime, where in a negligible barrier for injection from the

metal to the semiconductor causes the organic semiconductors to transport the maximum number

of carriers possible during device operation [1]. This will lead to the maximum current that the

organic semiconductor can support. If we consider only drift current and neglect diffusion

current, we can draw the diagram shown in Fig 2.6.

$E(x)$

J

0 d x
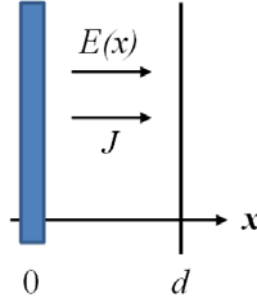
Fig. 2.6. Diagram representing charge injection from a metal to a semiconductor or thickness d, with the indicated direction of electric field $E(x)$ and drift current J. This model neglects diffusion current.

Assuming a single carrier type (electron only) injection we can invoke Poisson's law in one-dimension for the case of constant carrier mobility,

$$\frac{dE}{dx} = \frac{\rho}{\epsilon} = \frac{qn(x)}{\epsilon} \tag{2.16}$$

This implies then that

$$\frac{dE}{dx} = \frac{J}{\epsilon \mu E(x)} \tag{2.17}$$

We impose the boundary condition that

$$E(x = 0) = 0 \tag{2.18}$$

This can be justified because at the boundary $(x = 0)$, any electric field in the positive x-direction is assumed to be neutralized by an opposite electric field generated by the injected free charge carriers. A simple rearrangement and integration of the quantities in equation 2.17 then leads to

$$E(x) = \pm \left(\frac{2J}{\epsilon \mu}\right)^{1/2} x^{1/2} \tag{2.19}$$

Since in electrostatics, the electric field is given by the gradient of the voltage potential,

$$\mathbf{E} = -\mathbf{\nabla} V \tag{2.20}$$

we can write in one dimension that

28

$$E(x) = -\frac{dV}{dx} \tag{2.21}$$

and solve for applied potential, which is always positive. We therefore use the negative solution
of $E(x)$ as the integrand in the following expression,

$$V_a = -\int_0^d E(x')dx' \tag{2.22}$$

which leads to

$$V_a = \left(\frac{8J}{9\epsilon\mu}\right)^{1/2} d^{3/2} \tag{2.23}$$

solving this for the injection current we obtain,

$$J = \frac{9}{8}\epsilon_0\epsilon_r\mu\frac{V_a^2}{d^3} \tag{2.24}$$

which is known as the Mott-Gurney law [21] for charge conduction in a perfect insulator without

traps in the SCLC regime. In this expression, ϵ_0 is the permittivity of free space (8.85×10^{-12}

F/m), ϵ_r is the relative permittivity of the organic semiconductor, V_a is the applied voltage (in V),

and d is the thickness of the organic semiconductor (in m). Murgatroyd later modified this

expression to incorporate the field-dependence of the mobility,

$$J = \frac{9}{8}\epsilon_0\epsilon_r\mu_0 \exp\left(0.891\gamma\sqrt{E}\right)\frac{V_a^2}{d^3} \tag{2.25}$$

where γ is the field-dependence factor of the mobility [22].

Assuming a distribution of trap-states to follow the energy tail end of the Gaussian

density of states, i.e.

$$n_t(E) = \left(\frac{N_t}{kT_t}\right)e^{-\frac{q(E-E_c)}{k_BT_t}} \tag{2.26}$$

where E_c is the energy of the conduction level (in eV), and N_t is the density of traps (in cm^{-3}),

one can show a trap-charge limited current density (TCLC) can be modeled as

$$J = \frac{N_{\text{eff}}\, q\mu}{N_t{}^l} \left(\frac{\epsilon_0 \epsilon}{e}\frac{l}{l+1}\right)^l \left(\frac{2l+1}{l+1}\right)^{l+1} \frac{V^{l+1}}{d^{2l+1}} \tag{2.27}$$

where N_{eff} is the effective density of states in the transport band (in cm^{-3}) N_t is the total

concentration of traps (in cm^{-3}), and $l = qE_t/kT$ is a characteristic distribution parameter, where

E_t is the depth of the trap states (in eV) [23].

2.2.4 Charge Transport

Once charge carriers are injected into the organic semiconductors from opposing

electrodes, they must be transported to the EML where they can form excitons that decay to

produce light. The transport of these carriers is aided by the use of HTL and ETL materials. In

addition to having well matched energy levels to the electrode/injection-layer interface, these

materials are designed to rapid charge transport to the EML.

Charge carrier mobility is the speed at which the charge carriers move in the material in a

given direction in the presence of an applied electric field

$$\mu = \frac{v}{E}\left[\frac{\text{cm}^2}{\text{V}\cdot\text{s}}\right] \tag{2.28}$$

The mobility of a given material cannot be predicted from first principles, but there are a

number of experimental and semi-empirical models that are used to determine the mobility

parameter of a given organic semiconductor. Mobility is usually a influenced strongly by

material impurities and temperature, and is typically determined by experiment. Mobility is also

different for electrons and holes in a given semiconductor. For amorphous silicon $\mu \sim 5 \times 10^{-1} -$

10^{-3} cm^2/V·s.

Carriers move within an organic semiconductor by hopping from one molecule to the

next. The frequency of jumps, v_{ij}, between two adjacent sites i and j of site energies ε_i and ε_j

can be described by the Miller-Abrahams expression

$$v_{ij} = v_0 exp(-2\gamma\Delta R_{ij})exp\left[-\left(\frac{\varepsilon_i - \varepsilon_j}{kT}\right)\right]; \text{ if } \varepsilon_i > \varepsilon_j \qquad (2.29)$$

or

$$v_{ij} = v_0 exp(-2\gamma\Delta R_{ij}); \text{ if } \varepsilon_i < \varepsilon_j \qquad (2.30)$$

where v_0 is a pre-factor, γ is the inverse wave function decay constant, and ΔR_{ij} is the intersite distance between sites i and j [24], [25].

The transport in organic semiconductors in one-dimension can also be described by an electric field-induced directional drift velocity, $\boldsymbol{v_d}$, of mobile charge (in m/s), giving rise to a current density (in A/m^2):

$$J = q \cdot n \cdot v_d \qquad (2.31)$$

Here, q is the fundamental electrical charge and n is the local carrier density (in m^{-3}). The drift velocity can be written as the product of the mobility and the electric field,

$$v_d = \mu(T,E) \cdot E \qquad (2.32)$$

where μ is the field and temperature dependent mobility, T is the temperature, and E represents the applied electric field. For amorphous organic semiconductors it can be assumed that the mobility is isotropic, and thus transport is commonly treated in one-dimension [17].

For disordered organic semiconductors, all electronic states are localized and participate in conduction through thermally activated charge hopping. This yields a Poole-Frenkel like field dependence of the mobility with explicit dependence on electric field and temperature,

$$\mu(E,T) = \mu(0,T)e^{\gamma(T)\sqrt{E}} \qquad (2.33)$$

where $\mu(0,T)$ is the zero-field mobility, and $\gamma(T)$ is a field enhancement factor [26].

The most prominent model for fitting both the field and temperature dependence is Bässler's disorder formalism. Transport occurs by hopping through a manifold of localized states that are energetically and positionally disordered. Mobility can be expressed in terms of

intrinsic mobility and a Boltzmann-like expression that accounts for the energy barriers and the degree of disorder in the system. This accounts for the temperature dependence and the field dependence of transfer. The expression is given by

$$\mu(\sigma, E, T) = \mu_{0,0} \exp\left[-\left(\frac{2}{3}\frac{\sigma}{kT}\right)^2\right] \exp\left[C\left(\left[\frac{\sigma}{kT}\right]^2 - \Sigma^2\right)E^{1/2}\right] \tag{2.34}$$

where $\mu_{0,0}$ is the disorder-free mobility, C is an empirical constant with a value of 2.9×10^{-4} $(cm/V)^{1/2}$, and Σ is the width of the positional disorder distribution. This expression is only valid for high electric fields larger than 10^5 V/cm and for temperatures below the glass transition temperature T_g [41], and for a width of the position disorder distribution $\Sigma \geq 1.5$ [27].
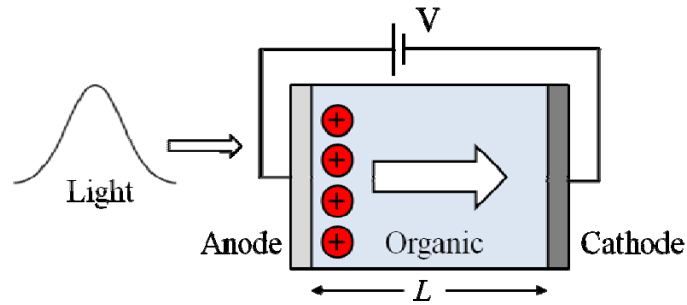
Fig. 2.7. Schematic representation of the time-of-flight (TOF) method.

For OLED applications, a possible experimental method for determining the hole and electron mobility values in organic semiconductors is the time-of-flight (TOF) method (see Fig. 2.7). In this technique, the semiconductor layer is excited by a light source. This can be done with a nitrogen laser emitting short pulses in the UV, creating a sheet of charges into the organic layer near a semi-transparent electrode where the light gets absorbed. The application of a voltage leads to an electric field E that sweeps across carriers of a single sign to the far electrode through the organic semiconductor film. The transit time, τ, is the time it takes the charge sheet to exit the sample. The drift velocity, v_d, is given by

$$v_d = \mu E = \mu \frac{V}{d} \tag{2.35}$$

We can relate v_d to τ by

$$\tau = \frac{L}{v_d} = \frac{L^2}{\mu V} \tag{2.36}$$

By measuring the arrival time of the charge, the carrier mobility of the organic semiconductor is determined for a specified value of E [28].

2.3 Excitons

Excitons can be described as quasi-particles in the solid that are excited states comprised of a Coulombically-bound electron and hole pair. They provide a transport of energy without a transport of net charge. Excitons typically form from electrons and holes that arrive in the emissive layer of the OLED, and decay when the electron and hole recombine to release light. In organic semiconductors the dielectric constant (ϵ_r) is ~ 3 while in inorganic semiconductors it is ~ 10. Therefore the excitons experience different levels of dielectric screening in the two classes of materials, which implies different exciton binding energy in these materials. This binding energy is much stronger in organic semiconductors (0.5-1.5 eV) and therefore excitons are localized in typical OLED materials. These so-called Frenkel excitons have a radius that is typically less than 5 Å, and is small when compared to intermolecular distance. In contrast, so-called Wannier excitons in an inorganic semiconductors such as Gallium-Arsenide (GaAs) are delocalized and have a radius of 40 to 100 Å [1] (see Fig. 2.8).
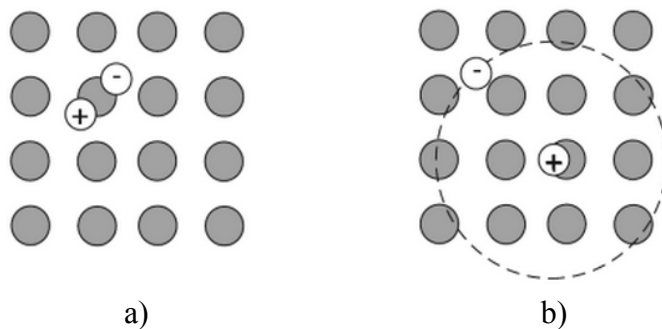
Fig. 2.8. Frenkel excitons that form in organic semiconductors and b) Wannier excitons that form in inorganic semiconductors. Reproduced from [29].

2.3.1 Singlet and Triplet Excitons

When an electron and a hole form an excited state through an electroluminescence process in a

molecule either an excited singlet state or an excited triplet state will form. Due to the spin, the

two-particle system can form four different states, three of which are symmetric with respect to

the exchange of spin of the particles, which are known as the triplet states with total spin $s = 1$:

$$\psi_t = \frac{1}{\sqrt{2}}(\uparrow\downarrow + \downarrow\uparrow) = |1, 0\rangle \tag{2.37}$$

$$\psi_t = \frac{1}{\sqrt{2}}(\uparrow\uparrow) = |1, 1\rangle \tag{2.38}$$

$$\psi_t = \frac{1}{\sqrt{2}}(\downarrow\downarrow) = |1, -1\rangle \tag{2.39}$$

and one of which is an anti-symmetric state, which is known as the singlet state.

$$\psi_s = \frac{1}{\sqrt{2}}(\uparrow\downarrow - \downarrow\uparrow) = |0, 0\rangle \tag{2.40}$$

Due to selection rules, light emission is allowed only from singlet states. Hence, if

fluorescent emitters are used as emitting molecules in an OLED, about 75% of the excitation is

lost in their triplet manifold, even if their fluorescent quantum yield reaches 100%. The majority

(75%) of excitons generated on emitters are generated in triplet states, and cannot radiatively

recombine to generate light. OLEDs containing phosphorescent dopants with heavy metal

complexes can make use of a mechanism known as intersystem crossing to mix singlet and triplet states and thereby harvest photons from both singlet and triplet emission. More details on intersystem crossing are given in section 2.5.2.

2.3.2 Langevin Recombination

After both holes and electrons have been injected into an organic semiconductor, the two charges interact and recombination can occur. The recombination rates of electrons and holes was studied first by Langevin in early 1900s [30].

Consider a fixed negative charge and a positive mobile charge both being attracted by the Coulomb force. The hole can avoid recombination at zero-field only if the thermal energy is sufficient to overcome the Coulomb potential:

$$\frac{e^2}{4\pi\varepsilon\varepsilon_0 r_c} = kT \tag{2.41}$$

The moving charge gets trapped in the Coulomb potential of the stationary charge if it is within a distance of less than the Coulombic capture radius r_c (see Fig. 2.9),

$$r_c = \frac{e^2}{4\pi\varepsilon\varepsilon_0 kT} \tag{2.42}$$
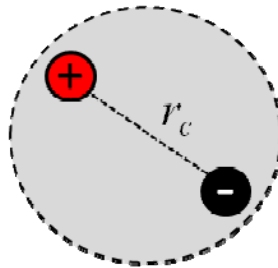
Fig. 2.9. Diagram of a Coulombically bound electron and hole pair, showing the coulomb radius.

From Poisson's law we can write the hole-current density in one-dimension as

$$J_{hole} = qp\mu E \tag{2.43}$$

35

where q is the elementary charge, p is the density of holes, μ is the mobility, and E is the magnitude of the electric field. Therefore, we can also write

$$J_{hole} = \frac{q^2}{4\pi\varepsilon r_c^2} p\mu \tag{2.44}$$

Hence, if we can obtain the total hole recombination current of holes flowing into a single sphere around the fixed electron with the radius r_c as

$$I_{hole,rec} = J_{hole} \cdot 4\pi r_c^2 = \frac{q^2}{\varepsilon} p\mu = \gamma q p \tag{2.45}$$

where γ is known as the Langevin recombination factor and is given by

$$\gamma = \frac{q}{\varepsilon}\mu \tag{2.46}$$

To extend this to the case for both electron and hole recombination currents, a total recombination current can be written as

$$I_{rec} = \gamma_t q p n \tag{2.47}$$

with

$$\gamma_t = \frac{q}{\varepsilon}(\mu_p + \mu_n) \tag{2.48}$$

Therefore, we can write the Langevin recombination rate as [1]

$$R = \gamma_t p n \tag{2.49}$$

2.4 Energy Transfer Mechanisms

Once a molecule is in an excited state, it can engage in different energy transfer processes with neighboring molecules before it relaxes back to the molecular ground state, releasing a photon in the process [1], [31], [32],[33]. Throughout this section, molecules are referred to as donors, M_D, whenever they give away energy or electrons. Similarly, molecules that accept energy or electrons are referred to as acceptors, M_A. Additionally, molecular states will be

denoted with preceding superscripts, i.e. 1 or 3, for singlet and triplet states, respectively. Excited states are marked with an asterisk.

2.4.1 Förster Resonant Energy Transfer

Förster resonant energy transfer (FRET) describes the transfer of energy by resonant coupling of electrical dipoles from a molecule in the excited state (donor) to a molecule in the ground state (acceptor). The Förster transfer mechanism can be written as (see Fig. 2.10)

$$M_D{}^* + M_A \rightarrow M_D + M_A{}^* \tag{2.50}$$
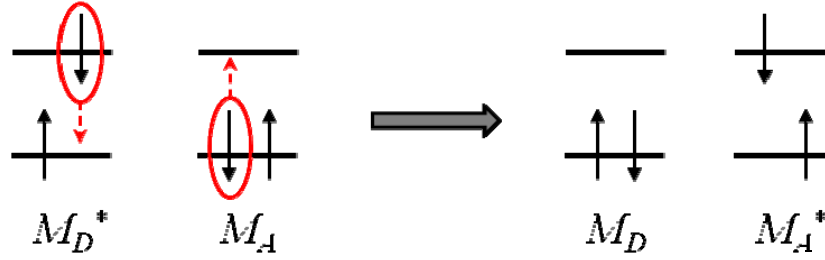
Fig. 2.10. The Förster resonant energy transfer process.

The electric field near an excited molecule can be described by the field generated by a classic dipole ($\mu = \mu_0 \cos \omega t$), where μ_0 is amplitude of the field and where ω the frequency of the field in radians ($\omega = 2\pi f$). This oscillation of electric charge will cause electrostatic forces to be exerted on nearby molecules. The interaction energy, E, between two dipoles μ_D and μ_A separated by a distance R_{DA} can be written as

$$E \propto \frac{\mu_D \mu_A}{R_{DA}^3} \tag{2.51}$$

Förster demonstrated that the rate of energy transfer in the case was proportional to E^2,

$$k_{ET} \propto E^2 \sim \frac{\mu_D^2 \mu_A^2}{R_{DA}^6} \tag{2.52}$$

For efficient FRET, the emission spectrum of the donor and the absorption spectrum of the acceptor have to overlap sufficiently. The rate of energy transfer can be given as

$$k_{ET} = \frac{k\chi^2 J(\varepsilon_A)}{\tau_D^0 R_{DA}^6}$$

(2.53)

where k is a constant determined by experimental conditions, τ_D^0 is the pure radiative lifetime of the donor, χ is a geometrical factor given by

$$\chi = \cos\theta_{DA} - 3\cos\theta_D \cos\theta_A$$

(2.54)

where θ_{DA} is the angle between the donor and acceptor moments, θ_D and θ_A are the angles between these moments and the vector connecting the donor and acceptor molecules (which is equal to 2/3 for the case a random distribution of oscillating dipoles). Finally, J is the spectral overlap integral,

$$J = \int f_D(v)\varepsilon_A(v)v^{-4}dv$$

(2.55)

where $f_D(v)$ is the donor emission spectrum as a function of the wave number v [cm^{-1}], and $\varepsilon_A(v)$ is the acceptor absorption spectrum.

The transition probability can be written as

$$k_{ET}(R_{DA}) = \frac{1}{\tau_D}\left(\frac{R_0}{R_{DA}}\right)^6$$

(2.56)

to emphasize the R_{DA}^{-6} long-range distance dependence. In this equation, τ_D is the experimental lifetime of the donor, and R_0 is the Förster radius and is given by

$$R_0 = cost.\left(\frac{\chi^2 \phi_D^0 J}{n^4}\right)^{1/6}$$

(2.57)

where ϕ_D^0 is the fluorescence quantum yield of the donor in the absence of energy transfer, and n is the average refractive index of the medium in the wavelength range where spectral overlap occurs. The Förster radius can be interpreted as the distance between the donor and acceptor at

which transfer and spontaneous decay of the excited donor are equally probable. A large Förster radius is associated with efficient energy transfer, which will compete with unimolecular relaxation processes at distances shorter than R_0. Finally, the transfer efficiency, $\eta_{\text{Förster}}$, can be expressed as

$$\eta_{\text{Förster}} = \frac{k_{ET}(R_{DA})^{-1}}{\tau_D^{-1} + k_{ET}(R_{DA})^{-1}} = \frac{1}{1 + \left(\frac{R_{DA}}{R_0}\right)^6} \tag{2.58}$$

2.4.2 Dexter Electron Transfer

In contrast to Förster transfer, which does not involve any charge transfer, a molecule can be excited if an exciton diffuses from donor to acceptor by transferring an electron and a hole at the same time. Because the transfer rate is proportional to the overlap of molecular orbitals, Dexter electron transfer is limited to relatively short distances (~10 Å) and attenuates exponentially with intermolecular distance [32]. Due to spin conservation, only singlet-singlet or triplet-triplet transfer is allowed [1]. The two dominant mechanisms for Dexter energy transfer are singlet-singlet Dexter energy transfer (see Fig. 2.11),

$$^1M_D{}^* + {}^1M_A \rightarrow {}^1M_D + {}^1M_A{}^* \tag{2.59}$$
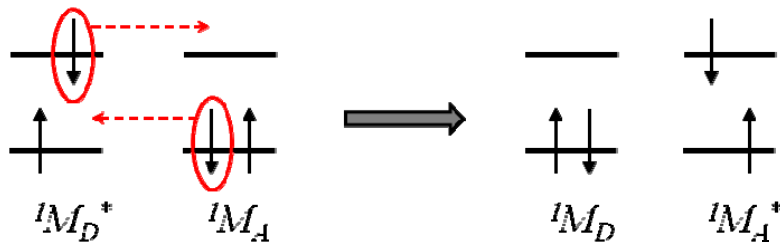
Fig. 2.11. Singlet-singlet Dexter energy transfer.

and triplet-triplet Dexter energy transfer (see Fig. 2.12)

$$^3M_D{}^* + {}^1M_A \rightarrow {}^1M_D + {}^3M_A{}^* \tag{2.60}$$
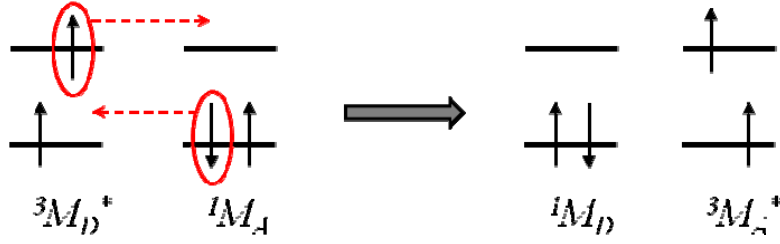
Fig. 2.12. Triplet-triplet Dexter energy transfer.

The efficiency of Dexter transfer depends on the degree of overlap between the emission and absorption spectra. The rate of Dexter transfer is given by

$$k_{\text{Dexter}} = k \cdot J \exp\left(\frac{-2R_{DA}}{L}\right) \tag{2.61}$$

Where k is a constant determined by experimental conditions (i.e. solvent index, concentration), R_{DA} is the distance between the donor and the acceptor molecules, J is the normalized spectral overlap integral between the normalized donor emission spectrum $\bar{f}_D(v)$ and the normalized acceptor absorption spectrum $\bar{\varepsilon}_A(v)$,

$$J = \int \bar{f}_D(v)\bar{\varepsilon}_A(v)v^{-4}dv \tag{2.62}$$

One other mechanism that also exists in phosphorescent OLEDs is triplet-triplet annihilation (TTA), which is due to triplet crowding on the phosphorescent emitters. In TTA, two triplets interact to produce a molecular entity in an excited singlet state and another in the ground singlet state [1] (see Fig. 2.13b). Such a mechanism can be described as (see Fig. 2.13a)

$$^3M_D{}^* + {}^3M_A{}^* \rightarrow {}^1M_D + {}^1M_A{}^*\ \text{TTA} \tag{2.63}$$
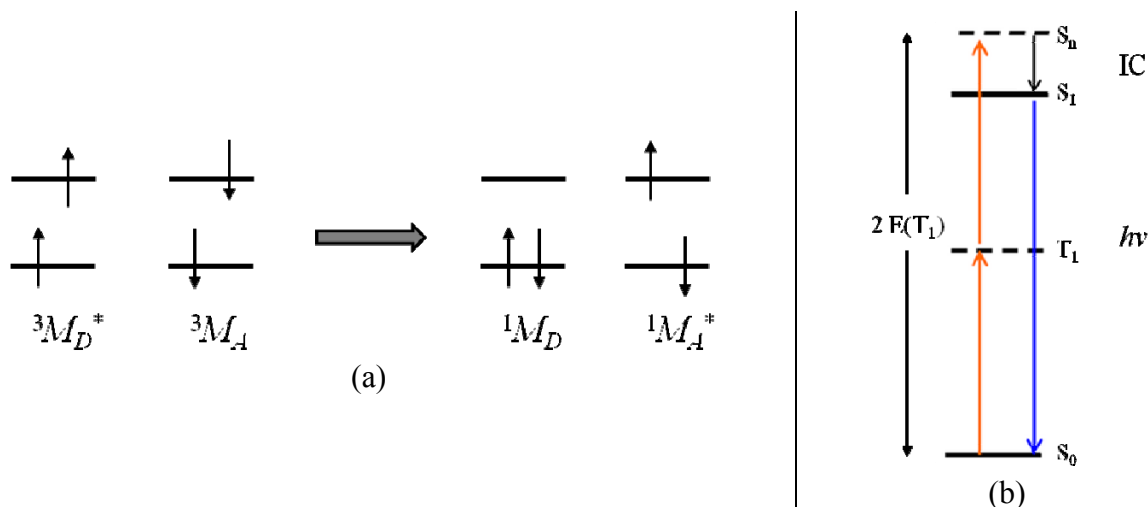
Fig.2.13. Triplet-triplet annihilation (TTA) mechanism and b) energetic representation of TTA. In b), when two molecules in the triplet state combine through triplet-triplet annihilation, one goes to the ground state while the other is excited to a higher energy singlet state (S_n) double the energy (shown as 2 E(T_1) in the diagram) of the molecule's triplet state. Internal conversion (IC) between S_n and the first excited singlet state (S_1) occurs due to Kasha's rule prior to photon emission.

2.5 Luminescence

Emitter molecules can emit photons by relaxation from an excited state to the ground state, releasing energy in the form of light. Experimentally, the intensity of a certain radiative transition is characterized by its oscillator strength, a dimensionless quantity that expresses the probability of absorption or emission of electromagnetic radiation in a transition. It is proportional to the intensity of the corresponding absorption band which is given by

$$f \propto \int_0^\infty \varepsilon(v)dv \qquad (2.64)$$

where $\varepsilon(v)$ is known as the molar extinction coefficient [liter/mol·cm], and v is the wave number [cm^{-1}]. To quantify an electronic transition, this integral is compared to an equivalent model described by classical oscillators, which leads to the dimensionless oscillator strength f:

$$f = 4.319 \times 10^{-9} \int_0^\infty \varepsilon(v)dv \tag{2.65}$$

2.5.1 Fluorescence vs. Phosphorescence

When an emitter molecule in an excited state undergoes a transition to a state with lower energy, it can emit energy in the form of light. The probability P of radiative relaxation from an initial state ψ_i to a final state ψ_j is proportional to the square of the transition dipole moment

$$P \propto \langle \psi_i | M | \psi_j \rangle^2 \tag{2.66}$$

where M is the dipole moment operator,

$$M = \sum_i er_i \tag{2.67}$$

where e is the electron charge and r_i is the distance of the i-th electron from the origin of a coordinate system that is fixed to the molecule. The dipole moment operator does not affect the spin part of the wavefunction of a state. Therefore, only transitions with similar spin symmetry result in a transition dipole moment that is unequal to zero.

Fig. 2.14 shows the Jablonski diagram, which represents the electronic states of a given emitter molecule and the transitions between these states. Radiative transitions are most favorable between the lowest singlet excited state S_1 and the singlet ground state S_0. This is represented in the diagram as the release of a photon at a rate k_r^S (the subscript r stands for radiative, and S signifies the emission from the singlet). The lowest triplet excited state T_1 has a longer lifetime than S_1. This is shown in the diagram as the release of a photon at a rate k_r^T, with $k_r^S \gg k_r^T$ (with T signifying the emission from the triplet). Emission resulting from transition from the first singlet excited state S_1 to the singlet ground state S_0 is called <u>fluorescence</u>. Emission resulting from transition from the first triplet excited state T_1 to the singlet ground state S_0 is known as <u>phosphorescence</u>.

For organic semiconductor emitters, the rate of internal conversion (k_{ic}) from higher

excited states S_n (or T_n) to the corresponding lowest excited state S_1 (or T_1) is much faster than

radiative processes from the higher singlet or triplet states themselves. Thus, emissive

recombination, i.e. fluorescence and phosphorescence, originates mainly from the lowest excited

states, S_1 and T_1, respectively. This is known as Kasha's rule [1]. For phosphorescent emitters

such as Ir(ppy)₃ with a heavy metal, a quantum mechanical process known as intersystem

crossing (ISC) allows an excited singlet to transform into a triplet state. Relaxation from this

lowest excited triplet state (T_1) to the ground state S_0, results in either radiative or non-radiative

decay.
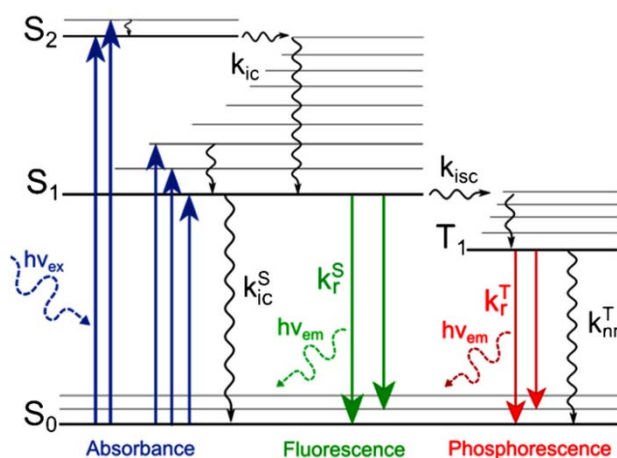
Fig. 2.14. The Jablonski diagram used to depict the electronic states of an emitter molecule and
the transitions between them. The ground state S_0 is a singlet state. Radiative transitions are most
favorable between the lowest singlet excited state S_1 and S_0. This is shown in the diagram as
releasing a photon with a rate k_r^S, whereas transitions from the lowest triplet excited state T_1 to
the ground state have longer lifetime (shown in the diagram as releasing a photon with a rate k_r^T,
with $k_r^S \gg k_r^T$). Reproduced from [34].

2.5.2 Intersystem Crossing

Intersystem crossing is a process that is exploited in the emissive layer of phosphorescent

OLEDs. It results from spin-orbit coupling caused by the presence of a heavy metal in the

structure of the emitting molecule. Due to this spin-orbit coupling, the spin-selection rules are

partially lifted, allowing for the mixing of singlet and triplet states. As discussed in section 2.5.1, ISC results when an emitter in the excited singlet state non-radiatively transforms to a triplet state through spin reversal. The emitter can then relax from the lowest excited triplet state, resulting in photon emission.

In phosphorescent OLEDs, the emissive layer consists of a host:guest system (such as CBP:Ir(ppy)$_3$) to achieve efficient phosphorescent in devices. As can be seen in Fig. 2.15, the host transfers energy from the both singlet and triplet excited states to the corresponding singlet and triplet excited states of the guest phosphor via long-range dipole-dipole exchange and short-range exchange, known as Förster and Dexter transfer, as discussed in section 2.4.
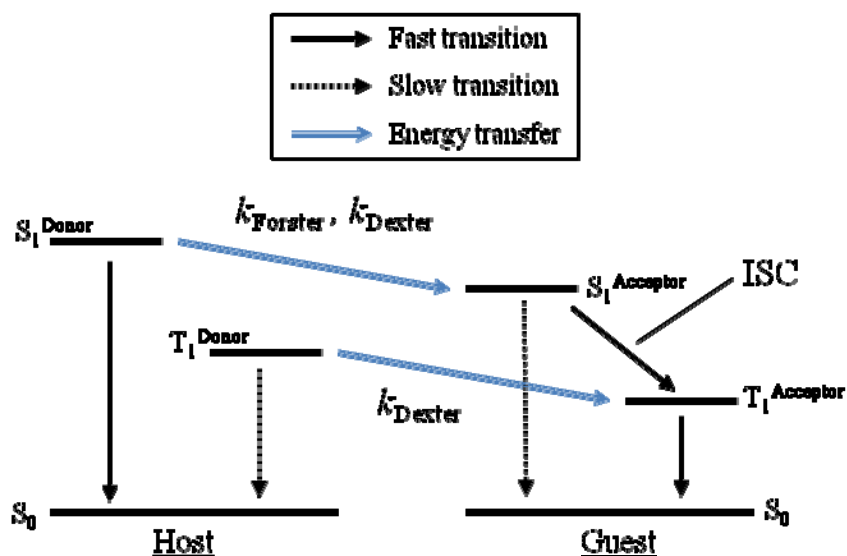
Fig. 2.15. A diagram to explain the energy transfer between host and guest molecules in a typical emissive layer of phosphorescent OLEDs.

2.6 Optical Loss Mechanisms in OLEDs

Despite the efficient generation of light in the emissive layer of state-of-the-art phosphorescent OLEDs, there are many loss mechanisms that limit the generated light from exiting the device. In this section, some of the dominant loss mechanisms will be briefly discussed.

2.6.1 Waveguide Modes

Due to its thin film layered architecture, a large fraction of the light created in the center of the organic stack can not to escape into air. However, it is desired to couple out as much light to the forward hemisphere, where the observer is typically located. In a very simple ray-tracing model, omitting microcavity effects and differences in the refractive indices of different functional materials, the efficiency to couple out light that is isotropically emitted in the OLED can be calculated [35].

Bottom-emitting OLEDs typically have a device architecture of planar glass substrate followed by ITO (on the order of a 100 nm), several organic layers, and a reflective cathode. The light generated in the organic emissive layer of these OLEDs encounters total internal reflection (TIR) at the ITO/glass interface and the glass/air interface. Thereby there are three waveguided modes that exist in these types of OLEDs. External modes where the generated light escapes through the substrate, substrate-waveguided modes, and ITO/organic-waveguided modes.
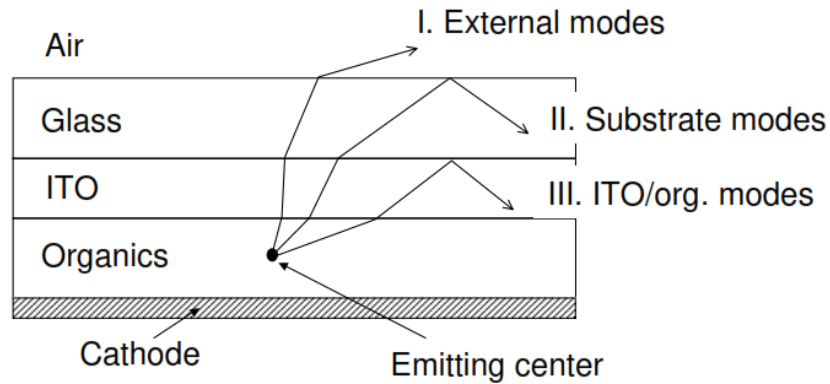
Fig. 2.16. A diagram showing the propagation of different waveguiding modes in the thin films and substrate comprising a typical bottom-emitting OLED. Reproduced from [36].

Assuming a normalized intensity profile of light in the emissive layer of the simple bottom-emitting OLED structure shown in Fig. 2.16, one can show that the outcoupling efficiency can be estimated by:

$$\eta_{ex} = \int_{0}^{\theta_{c1}} \sin\theta \, d\theta \qquad (2.68)$$

Where θ is the angle from normal in the emissive layer, and

$$\theta_{c1} = \sin^{-1}\left(\frac{n_{air}}{n_{org}}\right) \qquad (2.69)$$

is the critical angle for total internal reflection (TIR). These photons are emitted within the surface-escape cone and will emerge through the surface. This integral can be approximated as

$$\eta_{ex} = 1 - \cos\theta_{c1} = 1 - \sqrt{1 - \frac{1}{n_{org}^2}} \sim \frac{1}{2n_{org}^2} \qquad (2.70)$$

where n_{org} is the index of refraction of the organic materials. For standard organic semiconductors with an index of 1.71, the outcoupling efficiency comes out to 18.9%. The coupling to substrate modes can be given by η_{sub}

$$\eta_{sub} = \cos\theta_{c1} - \cos\theta_{c2} \qquad (2.71)$$

where

$$\theta_{c2} = \sin^{-1}\left(\frac{n_{glass}}{n_{org}}\right) \qquad (2.72)$$

Assuming n_{glass} to be 1.51, this comes out to 34.2%. Finally, the coupling efficiency to ITO/organic modes is given by

$$\eta_{ITO\text{-}Org} = \cos\theta_{c2} \qquad (2.73)$$

which comes out to 46.9%. These calculations assume isotropic orientation of the emitter molecules which is known to be violated, with OLEDs in the bottom-emitting configuration exceeding 30% EQE; however, it still shows the dramatic effects of optical loss through

waveguiding. The main reason for the inadequacy of such a ray-optics model is that the layer thicknesses in a typical OLED are shorter than the wavelength of emitted light [36].

One way to enhance the amount of extracted light from an OLED device is to attach an index-matched outcoupling structure to the bottom side of the substrate in order to circumvent the total internal reflection at the glass/air interface, hence getting access to the substrate modes, as shown in Fig. 2.17, by using glass lenses [36] or epoxy lenses [37]. Although these macro extractors are frequently used in research reports and have an excellent extraction efficiency, their size and weight contradict the flatness and low weight of OLED light sources which are key properties concerning their commercialization.
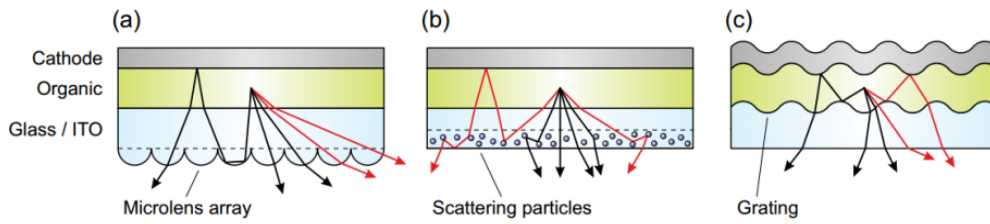
Fig. 2.17. Different strategies to increase light outcoupling from bottom-emitting OLEDs. Reproduced from [38].

Its noteworthy to mention that in inverted top-emitting OLEDs in this thesis, such substrate waveguiding and also ITO waveguiding modes do not exist. However, waveguiding through the organic materials still does occur to some degree. This is one important advantage of such an inverted top-emitting OLED structure.

2.6.2 Surface Plasmon Modes

Another significant loss mechanism in OLEDs is the near-field coupling of the emitting dipoles to the surface plasmons of reflective metals, i.e. the cathode in the bottom-emitting OLED or the anode in the top-emitting OLED. Surface plasmons are electromagnetic surface waves propagating along the interface between a conductor and a dielectric [39].

In Fig. 2.18a, a schematic representation of an electron density wave propagating along a metal – dielectric interface is shown. The charge density oscillations and associated electromagnetic fields are surface plasmon waves. These waves can be excited very efficiently with light in the visible range of the electromagnetic spectrum. In fig 2.18b, the distribution of the electric field in the metal and the organic semiconductor is shown. The electric field decays exponentially with increasing distance from the interface. The skin depth z_1 for the organic semiconductor is shown to be larger than the skin depth z_2 for the metal. The losses associated with surface plasmons are a function of distance from the interface, and are strong for distances between the emitter and the cathode up to 60-80 nm and steadily decreases [39].

Gartner and Greiner [40] expanded the field of the emitting dipoles into plane waves, which are parameterized by the horizontal wave vector k_{hor}. They calculated total radiant power F as an integral of the contributions $F(k_{hor})$:

$$F = \int_0^\infty F(k_{hor})k_{hor}dk_{hor} \tag{2.74}$$
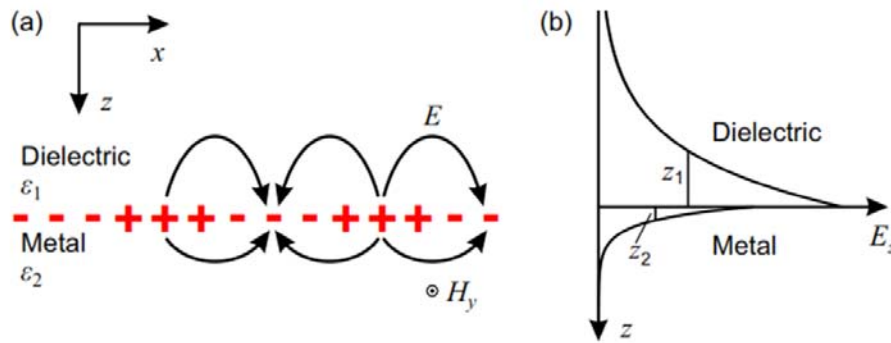
Fig. 2.18. (a) Representation of an electron density wave propagating along a metal – dielectric interface at a fixed time for a horizontally propagating surface plasmon wave. (b) Distribution of the electric field in the metal and the organic semiconductor is shown, with z_1 and z_2 representing the skin depth in the dielectric and metal, respectively.

They further introducing a normalized horizontal wavevector $\bar{k}_{hor} = k_{hor}/k_{air}$ allowed for the following classification of modes:

$$\bar{k}_{hor} \leq 1 \text{ power emitted to air}$$

$$1 \leq \bar{k}_{hor} \leq n_{sub} \text{ power into substrate modes}$$

$$\bar{k}_{hor} \geq n_{sub} \text{ power into organic and plasmon modes}$$

It is experimentally challenging to know precisely what amount of light is being lost, and there are instead computational methods to estimate these losses. Brütting et al. showed that for a bottom-emitting fluorescent OLED, approximately 10% of the light is lost to plasmon modes [41].

2.7 OLED Lifetime and Degradation

OLEDs are subject to degradation by both air and water-vapor. Therefore they must be encapsulated from ambient atmosphere in order to operate over long periods of time. OLED degradation mechanisms can be categorized into extrinsic and intrinsic, depending on whether they are due to the external stimulus or not.

External degradation in OLEDs can be caused by the formation of dark spots, the occurrence of electrical shorts leading to a sudden decrease in luminance (catastrophic failure) or intrinsic degradation. Dark spot formation and catastrophic failure can be suppressed by carefully optimized and controlled fabrication conditions and an adequate encapsulation of the devices and thus are no longer considered a major obstacle for commercial applications.

However, H_2O and O_2 remain as the major extrinsic sources in the atmosphere to degrade OLEDs. This was demonstrated in the early OLED research of Burrows, where simple glass encapsulation in N_2 atmosphere increased the OLED lifetime by 2 orders of magnitude [42]. Schaer reported that H_2O is 1000 times more destructive than O_2 for OLEDs [43]. Experimental measurements with OLEDs exposed to H_2O and O_2 separately, indicated that dark spot formation was 1000 times faster in H_2O than O_2. The effect of O_2 causes oxidation of metal and organic in

the bulk, whereas an electrochemical reaction of H_2O and with the metal released H_2 gas which leads to electrode delamination [43]. To prevent penetration, advanced barrier films (such as those made by Barix^{TM}) are typically used using roll-coating techniques. The films are transparent and flexible, made up by evaporated multilayers of polyacrylate and metal oxides such as Al_2O_3 with a moisture permeation rate of $<10^{-5}$ O_2 $g/m^2/day$ [44].

Intrinsic degradation is characterized by the decrease of overall luminance over time during continuous driving. This is accompanied by a rise of the operating voltage necessary to maintain operation at a constant current. This type of degradation is believed to result mainly from the deterioration of organic (and in some cases metal-organic) molecules in the device. Some mechanism include organic and metal diffusion [45], charge trap and luminescence quenching from chemical reactions, and thermal-induced morphology change [46]. The location and nature of these changes is highly dependent on the employed materials as well as the device structure. For chemical degradation, the different processes can be manifold and coupled even for a single device. It is due to this complexity that chemical degradation is still the least understood of the different modes of degradation [47].

2.8 References

[1] M. Pope, C.E. Swenberg, Electronic processes in organic crystals, Clarendon Press Oxford, 1982.
[2] B. Kippelen, Organic Optoelectronics, The electronic structure of organic compounds: General concepts, Class Notes, Georgia Institute of Technology, 2010.
[3] S. Bewick, R. Parsons, CK-12 Chemistry Quantum Numbers, Orbitals, and Probability Patterns, 2012.
[4] Chemical bonding and molecular structure, National Council Of Educational Research And Training, WorldPress, India, School Textbooks Online. 2014.
[5] P. Atkins, J. de Paula, Physical Chemistry, W. H. Freeman, 2006.
[6] S.-C. Chang, J. Liu, J. Bharathan, Y. Yang, J. Onohara, J. Kido, Multicolor Organic Light-Emitting Diodes Processed by Hybrid Inkjet Printing, Advanced Materials, 11 (1999) 734-737.
[7] D.A. Pardo, G.E. Jabbour, N. Peyghambarian, Application of Screen Printing in the Fabrication of Organic Light-Emitting Devices, Advanced Materials, 12 (2000) 1249-1252.

[8] A. Dodabalapur, Organic and polymer transistors for electronics, Materials Today, 9 (2006) 24-30.

[9] M. Berggren, D. Nilsson, N.D. Robinson, Organic materials for printed electronics, Nature Materials, 6 (2007) 3-5.

[10] S.R. Forrest, The path to ubiquitous and low-cost organic electronic appliances on plastic, Nature, 428 (2004) 911-918.

[11] J W Gardner, P N Bartlett, Electronic Noses. Principles and Applications, Measurement Science and Technology, 11 (2000) 1087.

[12] M. Schwoerer, H.C. Wolf, Organic Molecular Solids, John Wiley & Sons, 2007.

[13] J. Hwang, A. Wan, A. Kahn, Energetics of metal–organic interfaces: New experiments and assessment of the field, Materials Science and Engineering: R: Reports, 64 (2009) 1-31.

[14] C. Herring, M.H. Nichols, Thermionic Emission, Reviews of Modern Physics, 21 (1949) 185-270.

[15] W. Mönch, Semiconductor Surfaces and Interfaces, Springer, 2001.

[16] A.M. Cowley, S.M. Sze, Surface States and Barrier Height of Metal-Semiconductor Systems, Journal of Applied Physics, 36 (1965) 3212-3220.

[17] S.M. Sze, K.K. Ng, Physics of Semiconductor Devices, Wiley, 2006.

[18] J. Shinar, Organic Light-Emitting Devices: A Survey, Springer, 2004.

[19] X. Crispin, V. Geskin, A. Crispin, J. Cornil, R. Lazzaroni, W.R. Salaneck, J.-L. Brédas, Characterization of the interface dipole at organic/metal interfaces, Journal of the American Chemical Society, 124 (2002) 8131-8141.

[20] J.C. Scott, G.G. Malliaras, Charge injection and recombination at the metal–organic interface, Chemical Physics Letters, 299 (1999) 115-119.

[21] M.A. Lampert, P. Mark, Current injection in solids, Academic Press New York, 1970.

[22] P.N. Murgatroyd, Theory of space-charge-limited current enhanced by Frenkel effect, Journal of Physics D: Applied Physics, 3 (1970) 151.

[23] P. Mark, W. Helfrich, Space-Charge-Limited Currents in Organic Crystals, Journal of Applied Physics, 33 (1962) 205-215.

[24] A. Miller, E. Abrahams, Impurity Conduction at Low Concentrations, Physical Review, 120 (1960) 745-755.

[25] R. Coehoorn, W.F. Pasveer, P.A. Bobbert, M.A.J. Michels, Charge-carrier concentration dependence of the hopping mobility in organic materials with Gaussian disorder, Physical Review B, 72 (2005) 155206.

[26] P.W.M. Blom, C. Tanase, D.M. De Leeuw, R. Coehoorn, Thickness scaling of the space-charge-limited current in poly (p-phenylene vinylene), Applied Physics Letters, 86 (2005) 092105-092105.

[27] P.M. Borsenberger, L. Pautmeier, H. Bässler, Charge transport in disordered molecular solids, The Journal of chemical physics, 94 (1991) 5447.

[28] W.E. Spear, Drift mobility techniques for the study of electrical transport properties in insulating solids, Journal of Non-Crystalline Solids, 1 (1969) 197-214.

[29] M.C. Petty, Molecular Electronics: From Principles to Practice, Wiley, 2008.

[30] P. Langevin, Sur la loi de recombination des ions, Ann Chim Phys, 28 (1903) 433-530.

[31] T. Förster, Zwischenmolekulare energiewanderung und fluoreszenz, Annalen der physik, 437 (1948) 55-75.

[32] D.L. Dexter, A theory of sensitized luminescence in solids, The Journal of chemical physics, 21 (1953) 836.

[33] G. Ramos-Ortiz, Y. Oki, B. Domercq, B. Kippelen, Forster energy transfer from a fluorescent dye to a phosphorescent dopant: a concentration and intensity study, Physical Chemistry Chemical Physics, 4 (2002) 4109-4114.

[34] M. Quaranta, S. Borisov, I. Klimant, Indicators for optical oxygen sensors, Bioanal Rev, 4 (2012) 115-157.

[35] N.C. Greenham, R.H. Friend, D.D.C. Bradley, Angular Dependence of the Emission from a Conjugated Polymer Light-Emitting Diode: Implications for efficiency calculations, Advanced Materials, 6 (1994) 491-494.

[36] C.F. Madigan, M.H. Lu, J.C. Sturm, Improvement of output coupling efficiency of organic light-emitting diodes by backside substrate modification, Applied Physics Letters, 76 (2000) 1650-1652.

[37] J.M. Ziebarth, M.D. McGehee, A theoretical and experimental investigation of light extraction from polymer light-emitting diodes, Journal of Applied Physics, 97 (2005) 064502-064502.

[38] W. Brütting, J. Frischeisen, T.D. Schmidt, B.J. Scholz, C. Mayr, Device efficiency of organic light-emitting diodes: Progress by improved light outcoupling, physica status solidi (a), 210 (2013) 44-65.

[39] H. Raether, Surface plasmons on smooth and rough surfaces and on gratings, Springer, 1988.

[40] G. Gaertner, H. Greiner, Light extraction from OLEDS with (high) index matched glass substrates, 2008, pp. 69992.

[41] S. Nowy, J. Frischeisen, W. Brütting, Simulation based optimization of light-outcoupling in organic light-emitting diodes, International Society for Optics and Photonics, pp. 74151C-74151C.

[42] P.E. Burrows, V. Bulovic, S.R. Forrest, L.S. Sapochak, D.M. McCarty, M.E. Thompson, Reliability and degradation of organic light emitting devices, Applied Physics Letters, 65 (1994) 2922-2924.

[43] M. Schaer, F. Nüesch, D. Berner, W. Leo, L. Zuppiroli, Water Vapor and Oxygen Degradation Mechanisms in Organic Light Emitting Diodes, Advanced Functional Materials, 11 (2001) 116-121.

[44] P.E. Burrows, G.L. Graff, M.E. Gross, P.M. Martin, M.K. Shi, M. Hall, E. Mast, C. Bonham, W. Bennett, M.B. Sullivan, Ultra barrier flexible substrates for flat panel displays, Displays, 22 (2001) 65-69.

[45] S.T. Lee, Z.Q. Gao, L.S. Hung, Metal diffusion from electrodes in organic light-emitting diodes, Applied Physics Letters, 75 (1999) 1404-1406.

[46] F. So, Organic Electronics: Materials, Processing, Devices and Applications, Taylor & Francis, 2010.

[47] S. Schmidbauer, A. Hohenleutner, B. König, Chemical Degradation in Organic Light-Emitting Devices: Mechanisms and Implications for the Design of New Materials, Advanced Materials, 25 (2013) 2114-2129.

Chapter 3: Experimental Methodology

In this chapter, the experimental side of OLED fabrication is first discussed. Next, the measurement of OLEDs is described and key performance parameters are defined.

3.1 OLED Fabrication

OLED fabrication involves material purification, substrate preparation, and material deposition. These processes are described in the following sections.

3.1.1 Gradient-Zone Purification of OLED materials

In OLEDs, impurities in the organic semiconductor materials affect device performance. Although manufacturers sell purified materials, it is preferable to purify the materials one more time in-house. A common technique used in organic electronics is the gradient-zone purification method. In this method, the material to be purified is placed at the end of a glass tube and placed in a multiple zone furnace (see Fig. 3.1a and b). First, a mechanical pump lowers the pressure in the chamber to 10^{-2} Torr and then, a turbo pump lowers the pressure further to between 10^{-6} and 10^{-7} Torr. This is done to keep the process temperature lower than the decomposition temperature of the materials. When heated at these low pressures, the organic materials sublime. Impurities contained in a given material purify, condense back from the gas phase into the solid phase at a different temperature than the bulk material itself. Therefore, the glass tube is heated to different temperatures in different areas of the furnace. Compounds with different molecular structure and different molecular weight will then deposit in different locations along the glass tube, effectively separating the material from the impurities (see Fig. 3.1c). Finally, the purified material is retrieved from the tube. The purification process typically can take a few days.
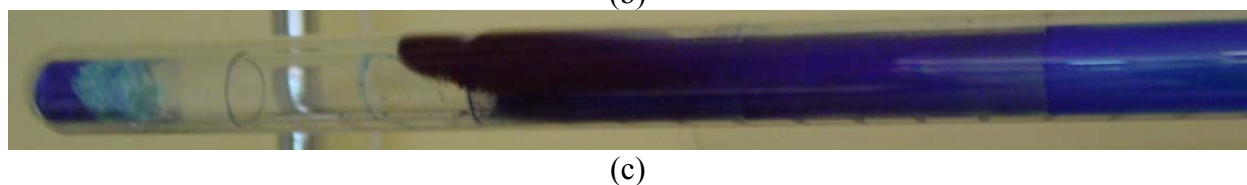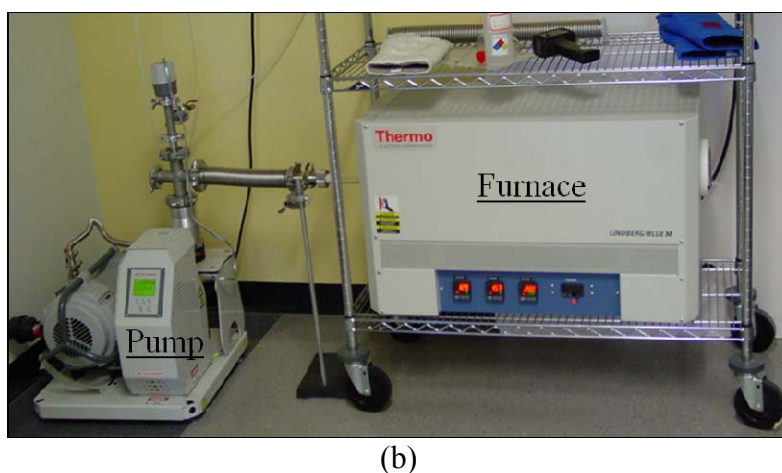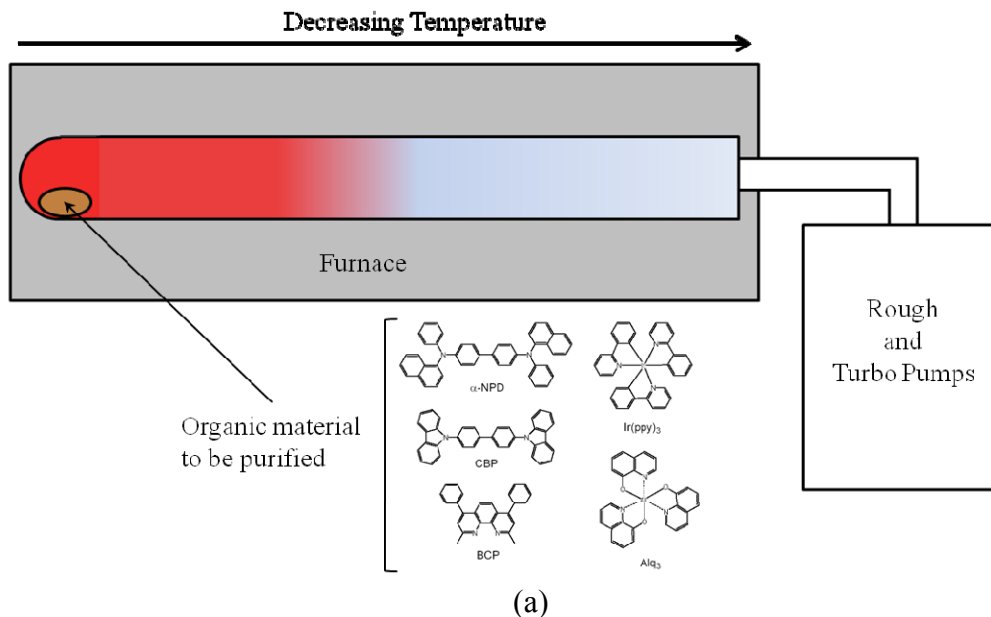
Fig. 3.1. a) A schematic of the gradient zone purification system and b) a photograph of the setup and c) an example of the different impurity levels of an organic material, copper phthalocyanine (CuPC), deposited along the tube.

3.1.2 Substrate Preparation

After material purification, a series of steps are undertaken to prepare OLED substrates for thermal evaporation of the organic semiconductor layers and inorganic metal electrodes.

These include cleaning the glass substrates with different solvents, plasma treating the substrates, and in some cases spin-coating a polymer buffer layer of poly(3,4-ethylenedioxythiophene) poly(styrenesulfonate) (PEDOT:PSS) on the substrates. Then the substrates are loaded into the thermal evaporator and evacuated to low pressures. The constituent OLED layers and are thermally evaporated sequentially onto the substrates. Finally, the OLED devices are unloaded and tested in a glove-box environment. These steps are shown in the flow chart in Fig. 3.2.
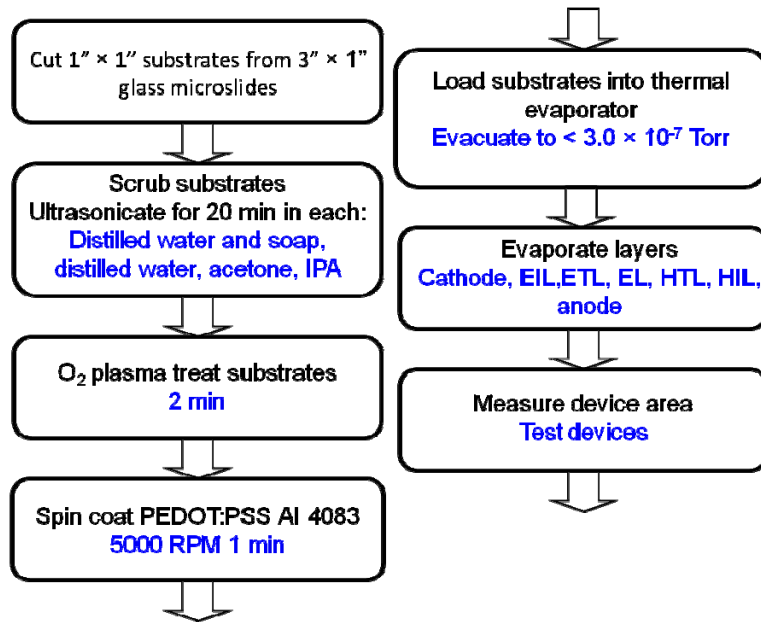
Fig. 3.2. Flowchart of the steps involved in fabricating OLEDs.

For ITO-based conventional (non-inverted) bottom-emitting OLEDs, ITO must be patterned. Thus the flow chart is modified from what is given in Fig. 3.2 to first include the steps shown in Fig. 3.3. As such, the fabrication of the inverted top-emitting is simpler than that of the conventional OLED. This is an added benefit to the OLEDs presented in this research.
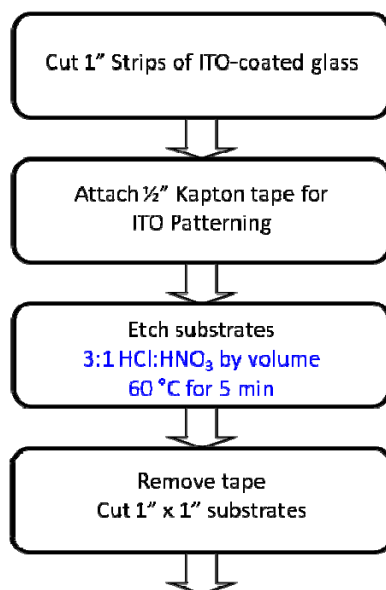
Fig. 3.3. Flowchart of the additional steps involved in fabricating conventional bottom-emitting OLEDs, prior to cleaning them.

Some of the steps in inverted top-emitting OLED fabrication are discussed in more detail in the following sections.

3.1.3 Oxygen Plasma Treatment

After the substrates are cut and before the spin-coating of the polymer PEDOT:PSS layer, the glass substrates are exposed to an oxygen plasma treatment. This is done in order to further clean the surface of the glass substrates and improve the wettability for spin-coating the PEDOT:PSS buffer layer [1]. Oxygen plasma treatment is often employed in ITO-based conventional bottom-emitting OLEDs as well in order to increase the work function of ITO for better hole injection to neighboring hole-injection materials or hole transporting materials [2].

Fig. 3.4. a) Photograph of plasma treatment system chamber. The substrates are loaded underneath the Pyrex dish and pumped down. b) A photograph of the active oxygen plasma. Reproduced from [3].

In order to perform plasma treatment, the cleaned substrates are placed into a parallel plate reactor as seen in Fig. 3.4a. They are then treated with a plasma that resembles what is shown in Fig. 3.4b. The processing parameters used for the plasma treatment were an oxygen flow rate of 25 sccm, a plasma power of 25 W, a chamber pressure of 150 mTorr, and a process time of 2 min.

3.1.4 Spin-coating of Polymer Buffer Layer

Spin-coating from solution is a common method to produce a thin, uniform polymer film on a planar substrate. In the inverted top-emitting OLEDs, it is used to make a uniform layer of the polymer PEDOT:PSS. This layer is deposited prior to the deposition of the Al cathode, so that it aids in the wetting and adhesion of the Al [1].

As shown in Fig. 3.5, in the spin-coating process, solution is first deposited on the substrate, and the substrate is then accelerated rapidly to the desired rotation rate. Liquid flows radially, and the excess is ejected off the edge of the substrate. The film continues to thin slowly until it reaches an equilibrium thickness or until it turns solid-like due to a dramatic rise in viscosity from solvent evaporation. The thickness of the film has been shown to be modeled by

57

$$d = \left(\frac{\eta}{4\pi\rho\omega^2}\right)^{1/2} t^{-1/2} \qquad (3.1)$$

where η is the viscosity coefficient in [Pa-s] of the solution, ρ is the density of the solution in

[kg/m^3], ω is the angular velocity [s^{-1}] of the spinning, and t is the spinning time in [s] [4].
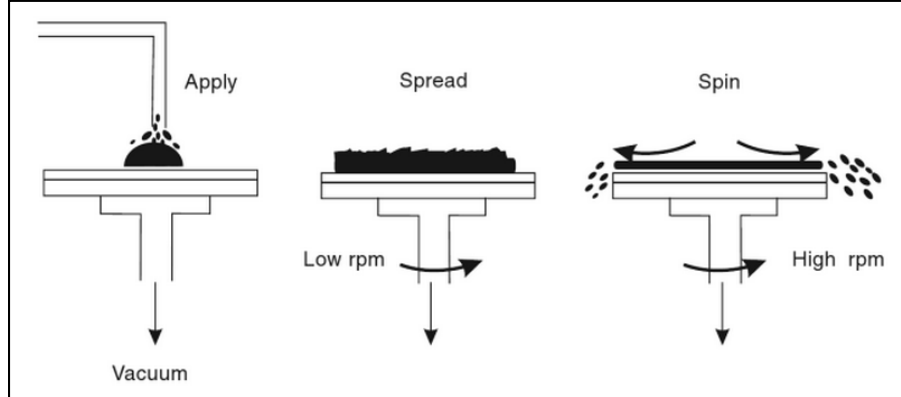
Fig. 3.5. A general diagram of the spin-coating procedure. Reproduced from [4].

In the case of the spin-coating of PEDOT:PSS, the parameters that are selected to achieve

a thickness of 40 nm (as measured by spectroscopic ellipsometry) are an acceleration of 1000

revolutions/min^2, a final spin-speed of 5000 revolutions/min, and a time of 1 min. After spin

coating the substrates are annealed for 10 min at a temperature of 140º C.

3.1.5 Thermal Evaporation of OLED materials

Let us first address a couple of physical models for the thermal evaporation of solid

materials to better understand the equipment that is used in OLED fabrication [5]. In general, the

rate of evaporation from solid surfaces can be given by

$$\Phi_e = \frac{\alpha_e N_A (P_e - P)}{(2\pi MRT)^{1/2}} \qquad (3.2)$$

where Φ_e is the evaporation flux in units of [#molecules/m^2-s], P_e is the equilibrium pressure of

the evaporant (in [Pa]) at temperature T, P is the ambient hydrostatic pressure acting on the

evaporant in condensed phase (in [Pa]), N_A is Avagadro's constant (6.02×10^{23} mol^{-1}), M is the molar mass (in [gm/mol]), R is the molar gas constant (8.31 J/K-mol), and α_e is the coefficient of evaporation, a dimensionless number between 0 and 1. The maximum evaporation rate is obtained when $\alpha_e = 1$ and the ambient pressure is 0 (i.e. a perfect vacuum) and therefore

$$\Phi_{e,max} = \frac{3.513 \times 10^{22}}{(MT)^{1/2}} (P_e) \text{ molecules/cm}^2\text{-s} \tag{3.3}$$

Next let us consider the source-substrate geometry for the deposition of thin-film solids, as it determines the uniformity of the organic films. For the purpose of calculation, the evaporation sources will be represented as a point source. In this case the particles of evaporated material originate from an infinitesimally small region (dA_e) of a spherical source with surface area A_e with a uniform mass evaporation rate Φ_e.
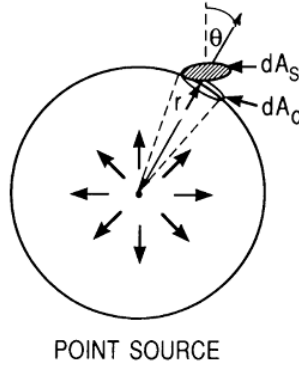
POINT SOURCE

Fig. 3.6. A diagram of a point source evaporator and the geometry of the substrate in relation to the source. Reproduced from [5].

The total evaporated mass $\bar{M}_e$ is then given by the double integral

$$\bar{M}_e = \int_0^t \int_{A_e} \Phi_e \, dA_e dt \tag{3.4}$$

Of this amount, a mass $d\bar{M}_s$ falls on the substrate of area dA_s (refer to Fig. 3.6). Since the projected area of dA_s on the surface of the sphere is $dA_c = dA_s \cos \theta$, one can write that

$$\frac{d\bar{M}_s}{dA_s} = \frac{\bar{M}_e \cos\theta}{4\pi r^2} \qquad (3.5)$$

where r is the distance from the source to the substrate, θ is the angle between the vector from

the point source to the substrate and the substrate normal. Thus it can be seen that the film

deposition rate (in [atoms/cm-s]), varies with the geometric orientation of the substrate and with

the inverse square of r, source-substrate distance. Maintaining thin-film thickness uniformity is

desirable in OLEDs, since accurate organic layer thicknesses are critical parameters for

achieving reproducible devices. Evaporation from a point source onto a plane substrate surface

can be represented two-dimensionally as in Fig. 3.7 where h is the distance between the source

and the substrate in the normal direction, r is the distance to any point on the substrate, and l is

the distance between that point and the center of the substrate.
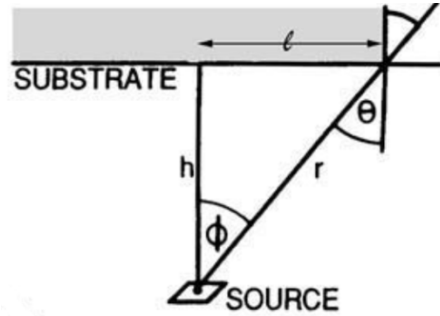
Fig. 3.7. The geometry of evaporation from a point source onto a plane substrate surface. Here, h is the distance between the source and the substrate in the normal direction, r is the distance to any point on the substrate, and l is the distance between that point and the center of the substrate. Reproduced from [5].

The film thickness d is then given by $\frac{1}{\rho}\frac{d\bar{M}_s}{dA_s}$, and therefore,

$$d = \frac{\bar{M}_e \cos\theta}{4\pi\rho r^2} = \frac{\bar{M}_e h}{4\pi\rho r^3} = \frac{\bar{M}_e h}{4\pi\rho(h^2 + l^2)^{3/2}} \qquad (3.6)$$

By choosing the h and l appropriately in the dimensions of the thermal evaporation chamber, a

desired film uniformity can be achieved.

A simplified schematic of a typical thermal evaporation system for fabricating OLEDs is depicted in Fig. 3.8. It consists of a chamber that is first evacuated to low pressures ($< 3 \times 10^{-7}$ Torr) using a combination of a roughing pump and a turbo pump. Inside the chamber are various sources that evaporate material. The substrates are placed in a substrate holder, and the assembly is mounted upside down with respect to the sources. They are separated from the sources by a shutter for control. The thickness of the organic layers is obtained through a thickness monitor as discussed later in this section. When heating the sources, the organic material starts evaporating and condensates on the sample and at the same time on a quartz crystal monitor (QCM), which is mounted above the source. With the QCM, the rate and thickness of the organic material can be controlled by measuring the frequency change of the quartz crystal resonator. Doping can be achieved by co-evaporation of two or more materials. Furthermore, the wafer rotates during evaporation leading to a more homogenous layer thickness.
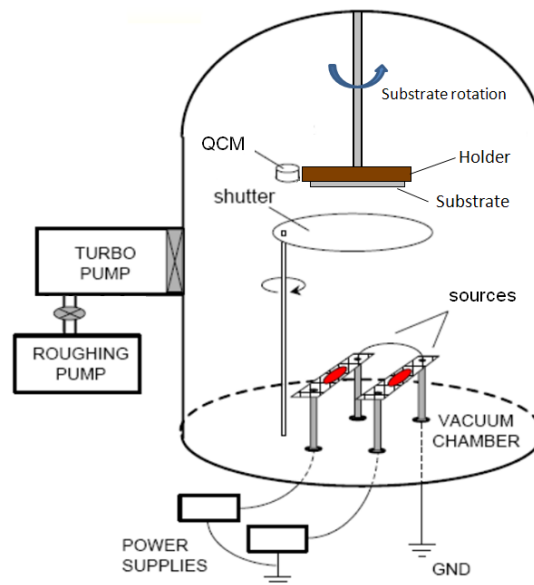
Fig. 3.8. A simplified schematic of the implementation of a thermal evaporation system. Adapted from [6].

During thermal deposition of the OLED materials, the evaporation rate fluctuates. To ensure accurate thickness measurement, feedback control is necessary for monitoring the thickness. A quartz oscillator is often used to measure the thickness. In thickness measurement using a quartz oscillator, the oscillation frequency of the quartz is reduced because of the change in mass due to the film formation on the surface of the quartz crystal. The correlation between the resonant frequency of the crystal, f_q, and thickness of the crystal, t_q, can be expressed as follows

$$f_q t_q = 1.69 \times 10^3 \text{ [m/s]} \tag{3.7}$$

Additionally,

$$\rho_f t_f = \rho_q t_q \frac{f_q - f_c}{f_q} \tag{3.8}$$

where ρ_q and ρ_f are density of the quartz oscillator and density of the deposited film, respectively, and t_q and t_f are thicknesses of the quartz oscillator and the deposited film, respectively [7]. This relationship allows for the determination of the film thickness t_f for the various organic and inorganic layers that are deposited in the fabrication of OLEDs.

Our EvoVac system (Angstrom Engineering, see Fig. 3.9) features eight organic sources and three metal deposition sources. It allows the co-deposition of three different materials simultaneously. It is comprised of a stainless steel deposition chamber with a motorized rotation stage for the substrates, an integrated mask storage unit for up to four shadow masks and one substrate holder.

Fig. 3.9. Inside of the EvoVac chamber showing three metal sources, and eight organic sources.

In Fig. 3.10(a-d), a visual schematic of an OLED sample is also illustrated in the different phases of fabrication within the EvoVac. All deposited layers are patterned using shadow masks. Finally, the overlap between the bottom Al cathode area and the top Au anode sandwiching the organic semiconducting layers, defines the active area. The top geometry of the OLEDs after each deposition step is shown in Fig. 3.10(a-e). A photograph of an operating OLED is shown shown in Fig. 3.10f.
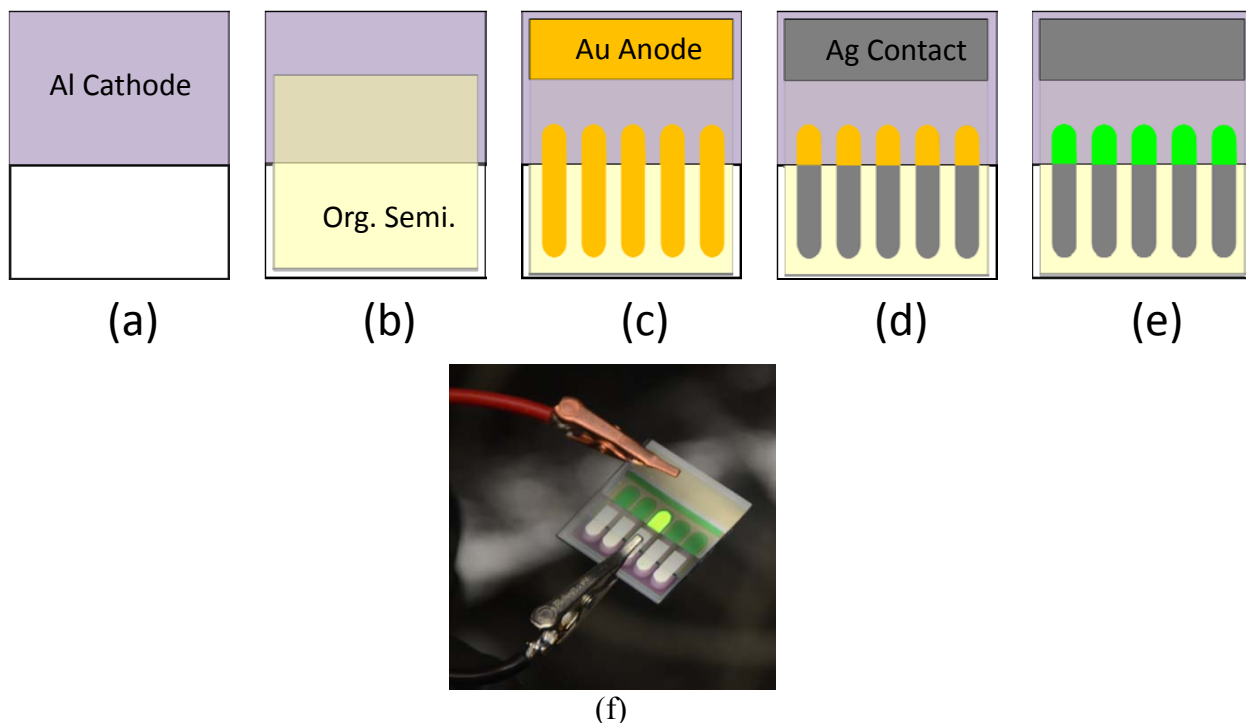
Fig. 3.10. The PEDOT:PSS coated glass substrates are shown after a) the deposition of the Al cathode, b) the organic semiconducting layers (EIL, ETL, EML, HTL, HIL), c) the Au anode, d) the Ag contact to the Au anode. Finally in e) the active area of the inverted top-emitting OLED is illuminated. A picture of an illuminated middle device is shown in (f). In this case, the cathode is contacted by the red trace via the "Ag contact" region labeled in (d), and the anode is contacted by the black trace.

3.2 OLED Testing

3.2.1 Characterization of OLED Performance

Current-voltage (I-V) characteristics of OLEDs are measured using a source meter (Keithley 2400). The current is measured while sweeping the applied voltage in the general range of -4 V to 12 V (exact range varies based on OLED structure) in 0.2 V increments. The luminance-voltage characteristics of the OLED devices are measured using a calibrated photodiode (FDS 100 from Thorlabs, Inc.). The photodiodes spectral response is shown in Fig. 3.11.
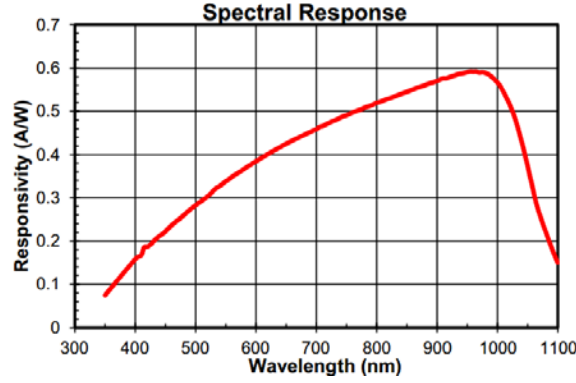
Fig. 3.11. The spectral response of a calibrated photodiode (FDS 100 from Thorlabs, Inc.).

The generated photocurrent from the photodiode is converted into a voltage by the transimpedance amplifier as seen in Fig. 3.12. A transimpedance amplifier is a current to voltage converter that uses an operational amplifier. It is used with sensors that have a current response that is more linear than the voltage response. This is the case with photodiodes where it is not uncommon for the current response to have better than 1% linearity over a wide range of light input. The transimpedance amplifier presents a low impedance to the photodiode and isolates it from the output voltage of the operational amplifier [8]. In its simplest form a transimpedance amplifier has just a large valued feedback resistor, R_f [Ω]. The gain of the amplifier is set by this resistor and because the amplifier is in an inverting configuration, the gain has a value of - R_f. In our setup the transimpedance amplifier consisted of an Analog Devices 549LH operational amplifier and a resistor R_f of 5 [MΩ]. This current-to-voltage converted outputs a detector voltage V_{det}, which is related to the detector photocurrent, I_{det}, by Ohm's law:

$$V_{det} = R_f I_{det} \tag{3.9}$$

This detector voltage is collected digital acquisition board (DAQPad 6020E, National Instruments).
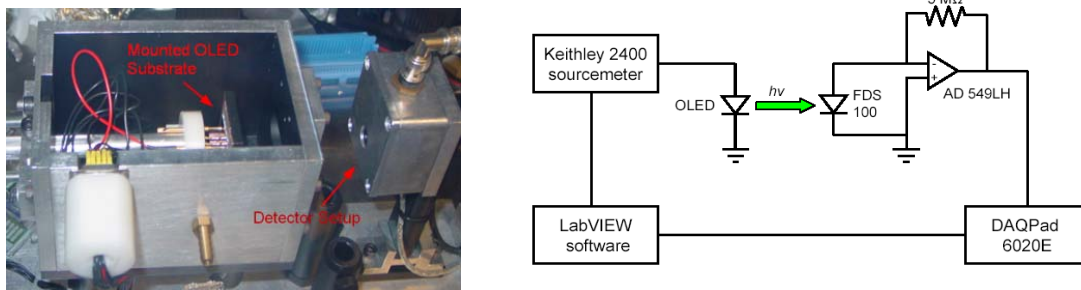
Fig. 3.12. Photograph of source and detector setup and schematic representation of the measurement system.

The luminance in forward direction L_v as a function of the current I is measured with a calibrated Si-photodiode (FDS-100). The measurements are recorded with a LabView program. The testing is done typically within a 24 hour time window after the deposition of the metal cathode onto the organic layers of the OLED in the same nitrogen glovebox atmosphere without exposing the devices to ambient atmosphere.

3.2.2 Characterization of OLED Electroluminescence Spectra

A radiometrically calibrated spectrometer (Ocean Optics USB4000) measures the absolute spectral irradiance $E_e(\lambda)$ [W/m^2·nm] in the forward direction at a defined luminance level that is high enough to be resolved clearly. Irradiance is the power of electromagnetic radiation (radiative flux) per unit area incident on a surface and is given in units of [W/m^2].

To obtain the angular dependent characteristics of OLEDs, a custom-made, computer controlled spectro-goniometer is used. An OLED device is mounted on the rotary stage and a manual alignment is undertaken so that the OLED active area is centered at the axis of rotation. The current and voltage to drive the device are again applied via a source meter (Keithley 2400). The spectrometer is used to measure the absolute spectral irradiance $E_e(\lambda, \theta)$ in the dark ambient light background at each angle which is calculated through an Ocean Optics software. For

66

purposes of presentation and data analysis, the spectra are generally normalized to the peak of the spectrum taken normal to the surface.

3.3 OLED Performance Parameters

The amount of light emitted from an OLED is typically characterized by its luminance value. Luminance is a photometric measure of the radiance travelling in a given direction. Radiance measures the quantity of radiation that passes through or is emitted from a surface and falls within a given solid angle in a specified direction. It is the radiant flux per unit solid angle per unit projected area of the radiator (or detector) source area, A_{proj}:

$$L_e = \frac{d^2\Phi_e}{dA_{proj}\,d\Omega} = \frac{d^2\Phi_e}{dA\,d\Omega\cos\theta} \tag{3.10}$$

and is in units of [W/m^2-sr] with θ representing the angle between the normal vector of the projected area plane and the vector normal to the source area plane. Luminance is radiance weighted by the visual response of the human eye and is used to formally characterize the amount of light emitted by OLEDs. It is expressed in units of [cd/m^2] (also called a nit). For details on photometry and radiometry, as well as the calculation of luminance for OLEDs please refer to Appendix B and Appendix C2, respectively.

3.3.1 Internal Quantum Efficiency (IQE)

In an optoelectronic device, internal quantum efficiency (IQE) is a metric to quantify the efficiency by which electrons are converted to photons in the active material inside the device itself, in contrast to the light that exits the device [9]. IQE is reported as a percentage.

To describe IQE in the most general sense, several terms must first be defined. The number of electrons injected per second in a device (such as an OLED) from the electrodes is the

total electron flux, Φ_{el}^{tot}, in units of [s^{-1}]. It can be calculated as the ratio of the injected current I, divided by the elementary charge q of an electron

$$\Phi_{el}^{tot} = \frac{I}{q} \tag{3.11}$$

where q is 1.60218×10^{-19} coulombs [C]. Not all injected charge carriers make it to the active region of a device, which in the case of OLEDs is the emissive layer. Therefore, an injection efficiency can be defined as the ratio of electron flux injected to the active region, Φ_{el}^{int}, to the total electron flux of the device:

$$\eta_{inj} = \frac{\Phi_{el}^{int}}{\Phi_{el}^{tot}} \tag{3.12}$$

Now, let's define radiative efficiency η_{rad} corresponding to the fraction of the injected electron flux, Φ_{el}^{int} that is converted into a photon flux Φ_{opt}^{int} in the active region (since not all electrons are converted to photons)

$$\eta_{rad} = \frac{\Phi_{opt}^{int}}{\Phi_{el}^{int}} \tag{3.13}$$

Finally, we can define IQE (η_{int}) to account for the carrier injection losses as well as non-radiative recombination losses in the active region. Therefore, η_{int} is the ratio of the photon flux generated in the emissive layer, Φ_{opt}^{int}, to the total electron flux , Φ_{el}^{tot}:

$$\eta_{int} = \frac{\Phi_{opt}^{int}}{\Phi_{el}^{tot}} = \eta_{inj}\eta_{rad} \tag{3.14}$$

In the more narrow sense of describing OLEDs, the IQE can also be written as

$$\eta_{int} = \gamma \cdot \eta_{rad,eff} \cdot \eta_{ST} \tag{3.15}$$

where with γ is the Langevin recombination factor, $\eta_{rad,eff}$ is the effective radiative efficiency of the emitter molecules, and η_{ST} the efficiency of the formation of excited electronic states that lead to radiative transitions. The Langevin recombination factor characterizes the efficiency of

bimolecular recombination in the emissive layer and is a number between 0 and 1 (see section 2.3.2 for more details). The effective radiative efficiency $\eta_{rad,eff}$ describes the number of generated photons to the number of generated excitons in OLED emissive layer and is given by [10], [11]

$$\eta_{rad,eff} = \frac{F\eta_{rad}}{1 - \eta_{rad} + F\eta_{rad}} \tag{3.16}$$

where F is the Purcell factor and η_{rad} is the emitter radiative quantum efficiency. The Purcell factor accounts for the fact that the rate of spontaneous emission depends on the local environment of the emitter. For instance, placing the light emitting molecules in a resonant microcavity environment modifies the rate of their spontaneous emission [12], [13]. In free space $F = 1$, and the effective radiative efficiency equals the intrinsic emitter efficiency η_{rad},

$$\eta_{rad} = \frac{\Gamma_{rad}}{\Gamma_{rad} + \Gamma_{nonrad}} \tag{3.17}$$

Where Γ_{rad} and Γ_{nonrad} are the radiative and non-radiative decay rates of the emitter.

Finally, the exciton formation efficiency, η_{ST}, is a number that varies between 0 and 1. As discussed in section 2.5.1, in OLEDs, assuming that exciton formation occurs statistically with respect to spin-orientation, then three times as many triplet excitons would form than singlet excitons. (This neglects the fact that the rate for singlet and triplet formation can be different and that more singlets can be formed by other processes such as triplet-triplet annihilation or reverse inter-system crossing (see section 2.4.2, and reference [14], respectively)). Therefore, in fist approximation η_{ST} has a maximum value of 0.25 for fluorescent emitters which radiate solely by singlet exciton decay. Note that this value can vary when additional physical processed are taken into account, such as triplet-triplet annihilation [15], [16], and the fact that the rate of singlet and triplet formation can be different in systems with extended conjugation such as conjugated

polymers [17], [18]. By harvesting both singlet and triplet excitons using phosphorescent emitters, the η_{ST} of some OLEDs can reach a value of 1 [19].

3.3.2 External Quantum Efficiency (EQE)

Non-transparent OLEDs emit light into a hemisphere, with the boundary consisting of a reflective metal electrode. The external quantum efficiency (EQE) gives the ratio of the number of photons emitted from an OLED device into this viewing direction, to the number of electrons injected into the device.

EQE is typically reported as a percentage, and can be written as

$$\eta_{EQE} = \frac{n_{ph}}{n_{el}} \times 100\% = \frac{\Phi_{optical}/hv}{I/q} \times 100\% \tag{3.18}$$

where n_{ph} and n_{el} are the number of photons and electrons injected, respectively. $\Phi_{optical}$ is the radiant flux of the OLED in [W], I is the current injected into the device (in amps [A]), and q is the elementary charge.

EQE can also be given as

$$\eta_{EQE} = \frac{2\pi}{hc} \frac{\iint E(\lambda,\theta)\,\lambda \sin\theta \, d\theta \, d\lambda}{I/q} \times 100\% \tag{3.19}$$

where $E(\lambda,\theta)$ is the angular spectral radiant intensity [W/sr] of the OLED, λ is the wavelength (in the visible range), θ is angle between the vector normal to the plane of the OLED and the vector normal to the plane of the detector and varies between 0 and 90 degrees.

As a performance parameter, EQE is related to IQE in that it considers how light is outcoupled from the internal organic layers of the device

$$\eta_{EQE} = \frac{\Phi_{optical}^{outcoupled}}{\Phi_{electrical}^{total}} = \eta_{int}\eta_{ph} \tag{3.20}$$

where η_{int} is the IQE, and η_{ph} is the light outcoupling efficiency. If there are significant loss mechanisms (see section 2.6), then the EQE can be much lower than the IQE.

There are some difficulties associated with measuring EQE. One is that EQE inherently

assumes a Lambertian source. The radiance of a radiating source is given by

$$L_e = \frac{d^2 \Phi_e}{dA \, d\Omega \cos \theta} \qquad (3.21)$$

In the approximation of small A and Ω (where $\cos \theta$ is approximately constant), L_e is given by

$$L_e = \frac{I_e}{A \cos \theta} \qquad (3.22)$$

A <u>Lambertian source</u> is one in which the observer radiant intensity is directly proportional to the

cosine of the angle, θ, between the observer's line of sight and the surface normal (see Fig. 3.13)

[20]. Mathematically, this is described as

$$I_e = I_{e0} \cos \theta \qquad (3.23)$$

where I_{e0} is the luminous intensity emitted perpendicular to the surface and therefore

$$L_{Lambertian} = \frac{I_{e0} \cos \theta}{A \cos \theta} = \text{constant} \qquad (3.24)$$
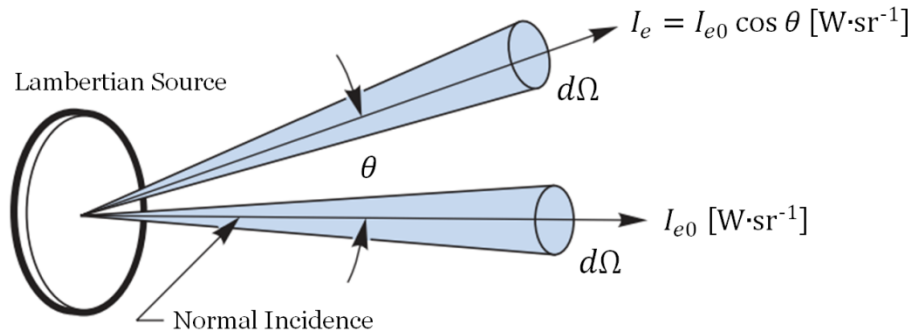
Fig. 3.13. Diagram to explain the angular emission characteristics of a Lambertian source. Adapted from [21].

Many common light sources such as incandescent lamps and LEDs cannot be considered

Lambertian emitters [22]. Bottom-emitting OLEDs based on a semi-transparent ITO anode are

generally considered Lambertian emitters. However, in OLEDs having microcavity structures,

the Lambertian assumption is false, and therefore EQE and other photometric quantities cannot be reported unless all of the light is collected from the OLED (with an integrating sphere for example).

Another potential source of error in reporting EQE is that the outcoupling efficiency might vary with driving voltage, viewing angle, and emission zone area and location. This can especially be an issue with stacked white OLEDs composed of stacking OLEDs with different colors, since each individual OLED unit will respond differently to the biasing, thus changing the spectrum of the white with driving current. Unless the different spectra are considered separately for the evaluation of the EQE, there will be an error in the calculated quantity.

For the derivation of the EQE formula used for our OLED measurement setup please refer to Appendix C3.

3.3.3 Current Efficacy

The <u>current efficacy</u> of an OLED is given in units of [cd/A], and is given by the formula

$$\eta_I = \frac{L_v}{J} \tag{3.25}$$

where L_v is the forward luminance [cd/m^2], and J is the current density in the device [A/m^2].

By definition, the current efficacy takes into account only the light that is emitted from the OLED in forward viewing direction (normal to the emitting surface). This means that the assumption that the OLED is a Lambertian source does not have to hold for this metric. Therefore, it will be used to describe the efficacy of inverted top-emitting OLEDs in this research.

High current efficacy is important because OLEDs are current-driven devices. Moreover, achieving a high luminance at low current densities is desirable because high currents lead to

degradation of the OLED. This is because organic semiconductors have resistance and therefore dissipate power through resistive (Joule) heating, which can change device performance.

3.3.4 Luminous Power Efficacy

Similar to the current efficacy, the luminous power efficacy also takes into account the applied voltage that is necessary to achieve a particular luminance level. The power efficacy describes the ratio of the luminous flux to the electrical input power. It is the photometric equivalent to the radiant efficiency or wall-plug efficiency. The luminous power efficacy, η_{lumEff}, is measured in units of [lm/W] and for a Lambertian emitter, it can be determined by

$$\eta_{\text{lumEff}} = \frac{\pi \times L_v}{J \times V} \tag{3.26}$$

where L_v is the luminance in units of $[\text{cd/m}^2]$, J is the current density in $[\text{A/m}^2]$, and V is the applied voltage in [V].

Although the applied voltage does not affect the EQE and current efficacy metrics, it does affect the luminous efficacy. Consequently, it is important to use design rules to minimize voltage losses arising from charge injection barriers and maintain good charge balance in order to produce an OLED with low power consumption. Once again, if the measurement and calculation of L_v assumes that the OLED is a Lambertian source, then one cannot report power efficacy for OLEDs that are non-Lambertian sources, such as the inverted top-emitting OLEDs in this research.

3.3.5 Maximum luminance

The maximum luminance $L_{v,max}$ $[\text{cd/m}^2]$ describes the highest intensity of light emitted from a surface per unit area in a given direction (typically the forward direction) over a range of operational voltage or current density. For an OLED device, this parameter is important to know for device applications since different device applications have different luminance

73

requirements. For solid-state lighting, one needs sufficient luminance values to illuminate a given environment. A T8 cool white fluorescent tube can achieve a luminance of 11,000 cd/m², whereas most computer screens do not get brighter than 1,000 cd/m^2.

3.3.6 Turn-On Voltage

The turn-on voltage in [V] is a parameter used to evaluate the performance of OLEDs. For OLEDs, turn-on voltage is typically defined as the voltage at which the luminescence of device reaches 10 cd/m^2. This is a luminance value which can easily be detected by the human eye, and is above the noise floor of the photodiode-amplifier setup used in the detection system (see section 3.2.1). The turn-on voltage can be obtained from the luminance-voltage characteristics of the device. A low turn-on voltage is desirable in order to obtain higher current density at a lower bias voltage. This is because higher voltages for a given current and luminance leads to a lower luminous power efficacy [lm/W] for the OLED device.

There are several factors believed to affect the turn-on voltages of OLEDs, such as the energy barrier height and dipoles at the electrodes-organic junctions and organic-organic heterojunctions (see section 2.2.1), differences of the work function between two electrodes, the thickness of organic transport and emissive layers, and the distribution of trap states in the organic layers and interfaces [23].

3.3.7 OLED Color Characterization

The color of light emitted by an OLED irrespective of its luminance can be characterized by its chromaticity value. Each color that can be seen by the human eye can be mapped onto a two-dimensional plot known as the Commission Internationale d'Eclairage (CIE)-diagram (see Fig. 3.14), where it is assigned a given CIE color coordinate. Additionally in Fig. 3.14, the emission colors of the temperature-dependant black body irradiation, known the Planckian locus,

is shown. For lighting applications, color temperatures below 5000 K are referred to as "warm" whites and temperatures above 5000 K are referred to as "cold" whites. For white light, another key parameter that is referenced is the <u>color rendering index</u> (CRI). The CRI is a measure for the ability of a light source to faithfully reproduce the colors of test objects in comparison to reference light source. For indoor-lighting applications a CRI greater than 80 is desired. For a full description of CIE coordinates and CRI, please refer to Appendix C, sections C1 and C4, respectively.
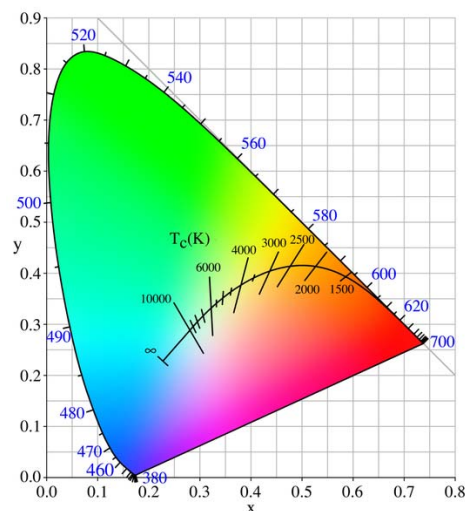
Fig. 3.14. The 1931 chromaticity diagram, showing the Planckian locus for ideal blackbody radiators.

3.4 References

[1] R. Steyrleuthner, S. Bange, D. Neher, Reliable electron-only devices and electron transport in n-type polymers, Journal of Applied Physics, 105 (2009) 064509-064509.
[2] C.C. Wu, C.I. Wu, J.C. Sturm, A. Kahn, Surface modification of indium tin oxide by plasma treatment: An effective method to improve the efficiency, brightness, and reliability of organic light emitting devices, Applied physics letters, 70 (1997) 1348-1350.
[3] C.S.R. Group, Plasma bonding of microfluidic devices, 2013.
[4] M.C. Petty, Molecular Electronics: From Principles to Practice, Wiley, 2008.
[5] M. Ohring, Materials Science of Thin Films, Elsevier Science, 2001.
[6] O. Vyavahare, Fabrication and Characterization of Organic Light Emitting Diodes for Display Applications. Thesis, (2009).
[7] T. Tsujimura, OLED Display Fundamentals and Applications, Wiley, 2012.
[8] P. Horowitz, W. Hill, The Art of Electronics, Cambridge University Press, 2006.

[9] B.E.A. Saleh, M.C. Teich, Fundamentals of Photonics, Wiley, 2013.

[10] H. Becker, S.E. Burns, R.H. Friend, Effect of metal films on the photoluminescence and electroluminescence of conjugated polymers, Physical Review B, 56 (1997) 1893.

[11] S. Nowy, B.C. Krummacher, J. Frischeisen, N.A. Reinke, W. Brutting, Light extraction and optical loss mechanisms in organic light-emitting diodes: Influence of the emitter quantum efficiency, Journal of Applied Physics, 104 (2008) 123109-123109.

[12] K.A. Neyts, Simulation of light emission from thin-film microcavities, JOSA A, 15 (1998) 962-971.

[13] X.-W. Chen, W.C.H. Choy, C.J. Liang, P.K.A. Wai, S. He, Modifications of the exciton lifetime and internal quantum efficiency for organic light-emitting devices with a weak/strong microcavity, Applied physics letters, 91 (2007) 221112-221112.

[14] K. Goushi, K. Yoshida, K. Sato, C. Adachi, Organic light-emitting diodes employing efficient reverse intersystem crossing for triplet-to-singlet state conversion, Nature Photonics, 6 (2012) 253-258.

[15] D.Y. Kondakov, T.D. Pawlik, T.K. Hatwar, J.P. Spindler, Triplet annihilation exceeding spin statistical limit in highly efficient fluorescent organic light-emitting diodes, Journal of Applied Physics, 106 (2009) 124510-124510.

[16] Y. Luo, H. Aziz, Correlation Between Triplet–Triplet Annihilation and Electroluminescence Efficiency in Doped Fluorescent Organic Light-Emitting Devices, Advanced Functional Materials, 20 (2010) 1285-1293.

[17] M. Wohlgenannt, K. Tandon, S. Mazumdar, S. Ramasesha, Z.V. Vardeny, Formation cross-sections of singlet and triplet excitons in π-conjugated polymers, Nature, 409 (2001) 494-497.

[18] Z. Shuai, D. Beljonne, R.J. Silbey, J.-L. Brédas, Singlet and triplet exciton formation rates in conjugated polymer light-emitting diodes, Physical review letters, 84 (2000) 131.

[19] M.A. Baldo, D.F. O'Brien, Y. You, A. Shoustikov, S. Sibley, M.E. Thompson, S.R. Forrest, Highly efficient phosphorescent emission from organic electroluminescent devices, Nature, 395 (1998) 151-154.

[20] E.F. Schubert, Light-Emitting Diodes, Cambridge University Press, 2006.

[21] Newport, Oriel Product Training, Spectral Irradiance, Stratford, CT, 2012.

[22] F. Grum, Radiometry, Elsevier Science, 2012.

[23] I.-W. Wu, Y.-H. Chen, P.-S. Wang, C.-G. Wang, S.-H. Hsu, C.-I. Wu, Correlation of energy band alignment and turn-on voltage in organic light emitting diodes, Applied physics letters, 96 (2010).

Chapter 4: Inverted Top-Emitting Single-Stack OLEDs

In this chapter, some of the key research results of the inverted top-emitting OLED devices are presented. A description of history and the state-of-the-art for electrophosphorescent inverted top-emitting OLEDs is first given. This is followed by a discussion of how higher efficiencies can be achieved in an OLED device structure where an Al/lithium fluoride cathode is employed at the bottom of the device. In addition, a novel anode consisting of 1,4,5,8,9,11-hexaazatriphenylene hexacarbonitrile (HAT-CN)-modified Ag is shown to act as an efficient hole-injecting electrode for application in inverted top-emitting OLEDs. Finally, these OLEDs are fabricated on recyclable crystalline nanocellulose (CNC) substrates, demonstrating the versatility of this inverted top-emitting architecture.

4.1 Historical Perspective

4.1.1 OLED in the Conventional Architecture

Electroluminescence phenomena was first mentioned by Henry Joseph Round in 1907. He discovered that current passed through silicon carbide (SiC) produced a yellowish light . Organic electroluminescence was not pursued until much later. Bernanose and co-workers discovered electroluminescence in organic materials in 1953 [2]. In the early 1960s, Williams and Schadt reported OLEDs based on anthracene thin films [3]; their work was expanded upon by Pope who focused on electrical contacts to organic materials [4]. These early devices made use of micrometer to millimeter organic crystals with applied voltages of a few hundred volts. With advances in semiconductor technology, new techniques such as vacuum thermal deposition led to the fabrication of much thinner and uniform small-molecule organic thin-films. Thus, the applied voltage for electroluminescence was reduced to below 100 V.

In 1987, Tang and VanSlyke at Kodak reported the first OLEDs with higher efficiencies (1.5 lm/W at 100 cd/m^2 at a voltage of 5.5 V) with OLEDs based on small molecules in a two-layer architecture. The device structure comprised a hole-transporting layer (HTL) and an

electron transporting layer (ETL) of N,N'-diphenyl-N,N'-bis (3-methylphenyl) 1,1'-biphenyl-4, 4' diamine (TPD) and (tris(8-hydroxyquinoline) aluminum (Alq_3), respectively. The two thin layers were deposited on an indium tin oxide (ITO) anode and featured a magnesium-silver (Mg/Ag) cathode. This OLED device had an maximum EQE of 1%, and a maximum luminance value of just over 1000 cd/m^2 at 7.5 V [5].

In the late 70s, Heeger, MacDiarmid, and Shirakawa demonstrated enhanced electrical conductivity of organic polymers through doping [6, 7], for which they were awarded the Nobel Prize in chemistry in 2000. This knowledge precipitated the development of the first polymer based OLED in 1990 by Burroughes et al. just after Tang and VanSklyke's seminal work [8].

With these advances by Tang and VanSklyke, organic semiconductors began their rise as a viable alternative to inorganic semiconductors. Traditionally, known organic semiconductors were wide bandgap insulators with low conductivity [6, 9-11]. After much research on both materials and interfaces, carrier mobility values in small molecule organic thin-film devices of 43 cm^2 /V-s were achieved [12] (for comparison, amorphous silicon can achieve a maximum mobility of 10 cm^2 /V-s [13]).

In the late 1990s and early 2000s, advances were made based on the work of S. R. Forrest, M. E. Thompson and their groups on phosphorescent organometallic emitters. They overcame material limitations on the internal quantum efficiency of OLEDs based on fluorescent materials, and allowed for OLEDs that achieve 100% internal quantum efficiencies by making use of both triplets and singlet states in specially designed phosphorescent emitters using heavy metals [14]. Most recently, M. G. Helander et al. demonstrated the highest OLED efficiencies to

date, achieving an EQE of over 50% and power efficiency of over 200 lm/W from through

10,000 cd/m^2 in devices with an Ir(ppy)$_2$(acac) emitter and optical outcoupling [15].

4.1.2 OLED in the Inverted Architecture

In the literature, attempts at using a bottom-cathode of aluminum with a lithium fluoride

(LiF) EIL yielded inferior performance compared to top-cathode devices [16, 17]. In top-cathode

OLEDs, the hot metal deposition reacts with an underlying layer of LiF and dopes the underlying

ETL [18, 19]. It was asserted that an Al/LiF cathode could not work in inverted architectures

because the metal is deposited first and the necessary chemical reaction could not take place

[16]. There were other reports that suggested, however, that the mechanism was not a chemical

reaction but rather an electron injection barrier reduction [20] or tunneling through the thin layer

of insulating LiF [21]. The conflicting reports from the literature led us to try the Al/LiF in the

inverted architecture with a range of different ETLs. These devices showed promising results.

Further optimization of these devices lead to improved performance as discussed in section 4.2.

Historically speaking, Bulović et al. reported the first inverted small molecule top-

emitting OLED with the Alq$_3$ based OLED contained a Mg:Al bottom cathode. These devices

yielded an external quantum efficiency (EQE) of 0.3% [22]. The first attempt at a pure Al

cathode with a separate doped EIL was made by Dobbertin et al., who used a lithium doped 4,7-

diphenyl-1,10-phenathroline (BPhen) EIL. These devices had a current efficacy of 4.2 cd/A and

a power efficacy of 1.0 lm/W at a luminance of 1,000 cd/m^2 [23].

Inverted top-emitting OLEDs have been investigated primarily with fluorescent emissive

compounds [16, 23-28]. For this type of OLED, the highest current efficacy reported was 33.8

cd/A at 6,670 cd/m^2 [29]. Scarce reports exist on inverted top-emitting OLEDs with emissive

layers containing phosphorescent dopants [25, 29]. For these OLEDs, the highest current efficacy reported was 55.4 cd/A at 140 cd/m^2. This device contained a lithium-doped electron transport layer (however, lithium is environmentally unstable), two emissive layers, and a radio-frequency magnetron sputtered ITO anode, which requires a separate deposition chamber [29].

4.2 Highly Efficient Green Inverted Top-Emitting OLEDs

The major challenge in fabricating efficient inverted OLEDs has been finding a highly reflective bottom cathode capable of effectively injecting electrons into the ETL [27]. Most organic semiconductors have a rather low electron affinity making it difficult to inject electrons efficiently from a metal electrode with good environmental stability such as aluminum [30]. Aluminum has a high reflectance and is less reactive than lower work function metals such as calcium and magnesium, however its work function is too high to be used as an efficient cathode in OLEDs. A strategy that is often employed in conventional top-cathode bottom-emitting OLEDs is to insert a thin layer of lithium fluoride (LiF) between the electron transport layer and the top aluminum cathode [21]. While this approach has been implemented in top-cathode OLEDs, attempts to fabricate bottom cathodes by depositing LiF on top of Al electrodes yielded modest performance with tris-(8-hydroxyquinoline)aluminum (Alq$_3$) [16],[28] ETLs.

Reports of inverted top-emitting OLEDs have mostly focused on devices with fluorescent emissive layers [23],[28]. The highest current efficacy reported for a fluorescent inverted top-emitting OLED was 33.8 cd/A at 6,670 cd/m^2, using an aluminum/lead monoxide cathode [29]. As mentioned in section 4.1.2, few attempts have been made to study inverted top-emitting OLEDs with emissive layers containing phosphorescent dopants that allow for both singlet and

triplet excited states to contribute to light emission [25],[29]. Again, the highest current efficacy reported for a phosphorescent inverted top-emitting OLED was 55.4 cd/A at 140 cd/m^2.

Some of the early attempts to fabricate inverted top-emitting OLEDs in our group involved the use of zinc oxide-modified ITO as an electron injection layer. This was following the precedent by Bolink et al., who used ITO/ZnO hybrid cathodes in many of their inverted fluorescent emitter-based device architectures [31]. His hybrid inorganic-organic OLEDs (referred to as HyLEDs in the literature) achieved higher efficiencies, as shown in Fig. 4.1, taken from [32].
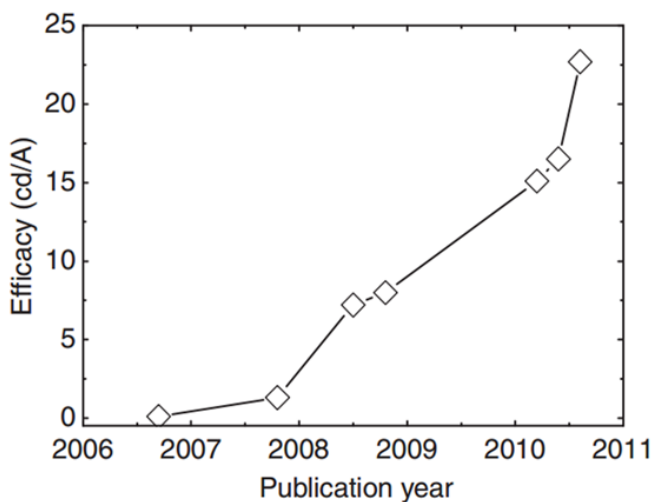
Fig. 4.1. Device efficacy for metal-oxide based Hy-LEDs using ZnO for example in both inverted and conventional architectures. The devices were all fluorescent OLEDs, and the current efficacy does not go beyond 25 cd/A. Taken from [32].

The ZnO was often modified by an additional surface modifier, such as calcium carbonate (Cs_2CO_3) or other compounds to further reduce the work-function of the electrode in order to match the electron affinity of the neighboring electron transport materials (3.0 eV in the case of BPhen, shown in Fig 4.3). An example device architecture that was pursued is given in

Fig. 4.3, with the resulting device performance given in Fig. 4.4. It can be seen that the device

performance is quite poor, with the devices hardly producing 1000 cd/m^2 at voltages of 10 V,

with external quantum efficiencies less than 0.5%. As mentioned in section 4.1.2, it was the

conventional belief that an Al/LiF cathode could not work in inverted architectures because the

metal is deposited first and the necessary chemical reaction between the LiF, the Al, and the ETL

could not take place (see Fig. 4.2) [16]:

$$3\,LiF + Al + 3\,Alq_3 \rightarrow AlF_3 + 3Li^+Alq_3^-$$
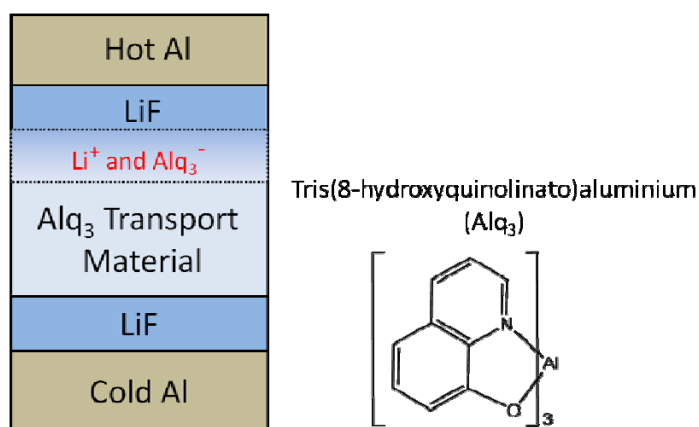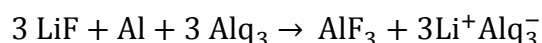
Fig. 4.2. Device reflecting conventional view that an Al/LiF cathode could not work in inverted architectures because the metal is deposited first and the necessary chemical reaction between the LiF, the Al, and the ETL could not take place. In the diagram it is shown that the deposition of the top hot Al electrode would initiate this reaction, while the cold bottom Al electrode would not.

However, as mentioned in section 4.1.2, there were other reports that suggested that the

mechanism was not a chemical reaction but rather an electron injection barrier reduction [20] or

tunneling through the thin layer of insulating LiF [21]. The conflicting reports from the literature

led us to try the Al/LiF in the inverted architecture. One such device architecture employing a

bilayer cathode comprising of 2.5 nm of Al and 2.5 nm of LiF is shown in Fig. 4.5. This device

remarkably showed external quantum efficiencies on the order of 5% as shown in Fig. 4.6, which

was an order of magnitude better than devices based on ZnO-modified ITO. One downside that

can be seen in the data in Fig. 4.6 is the lack of reproducibility, which was attributed to the

thinness of the layers. Through the course of some follow-up experiments we realized we could

completely eliminate the PEDOT:PSS-modified ITO, and thicken the Al layer and thin the top

Au contact to produce reproducible, efficient inverted and top-emitting devices. These devices

are described in detail in section 4.2.
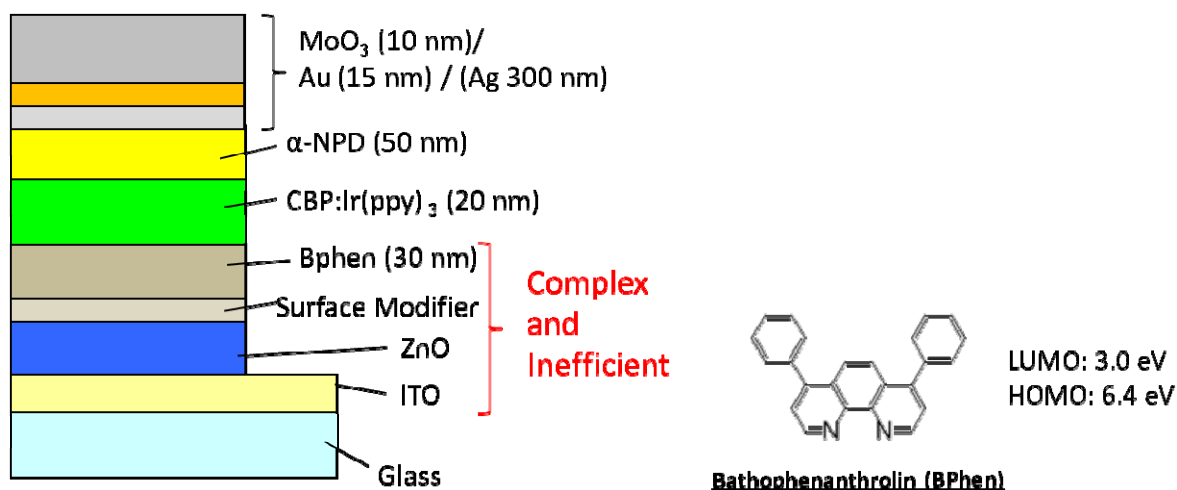
Fig. 4.3. Example of an early OLED device structure that was fabricated in the beginning, employing a ZnO-modified ITO electron injecting bottom cathode. The ITO/ZnO/Surface-modifier (i.e. Cs_2CO_3 or similar compound) was both complex and inefficient at electron injection, as evidenced by the device performances in Fig. 4.4.
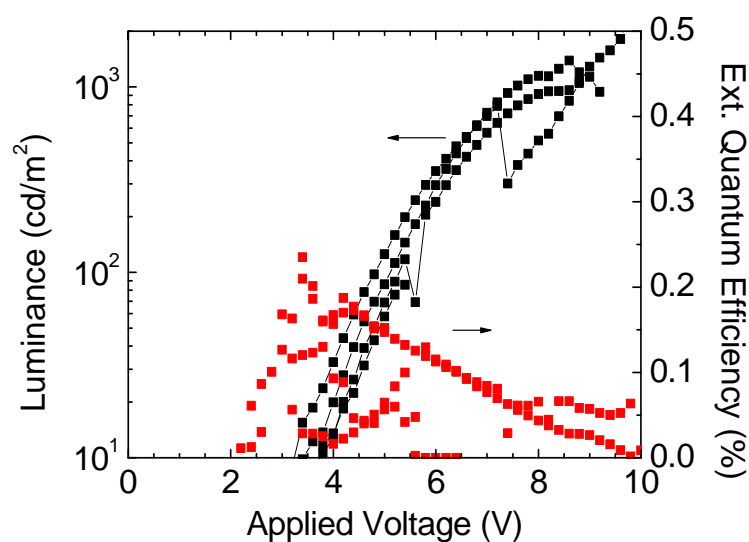
Fig. 4.4. Performance of the device depicted in Fig. 4.3. These OLEDs performed poorly, with low luminance values, high driving voltages, and low external quantum efficiencies. In addition, the device yield and reproducibility was poor.
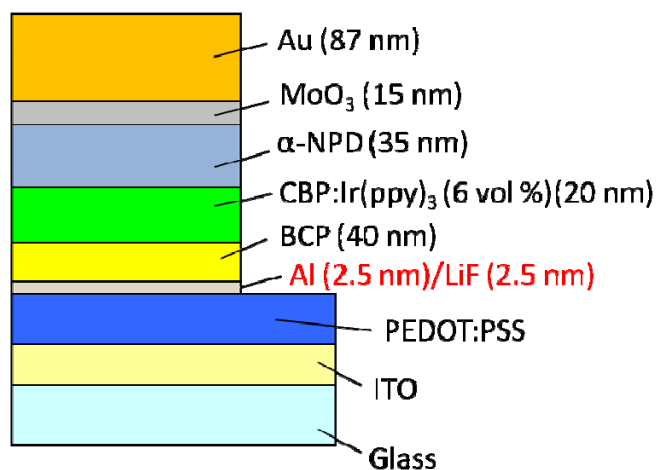
Fig. 4.5. Example of a device architecture using a bilayer bottom cathode of Al (2.5 nm)/LiF (2.5 nm) on top of PEDOT:SS-modified ITO. This device yielded more promising performance as evidenced by the plot in Fig. 4.6. The device architecture was improved upon during the course of the research, and the ITO, and PEDOT:PSS layer was eliminated entirely.
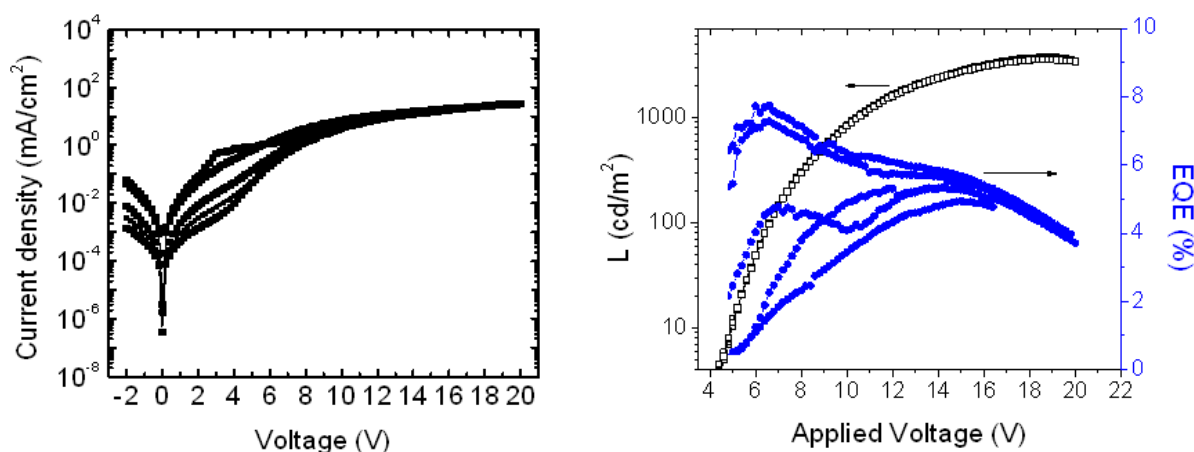
Fig. 4.6 Device performance characteristics of devices shown in Fig. 4.5. These devices have much higher EQE performance in comparison with devices employing ZnO-modified ITO.

One further modification that was made to the device architecture that led to the optimized OLEDs was the incorporation of a PEDOT:PSS buffering layer between the substrate and the Al cathode, as shown in Fig. 4.7. The resulting current-voltage characteristics and luminance-voltage and current efficacy-voltage characteristics are shown in Fig. 4.8. Here, it can be seen that devices with the PEDOT:PSS layer had considerably higher current efficacy (Fig. 4.8b). This is in addition to an improved yield in the devices with the PEDOT:PSS. The enhanced performance of these diodes is attributed to the fact that PEDOT:PSS planarizes the substrate and provides good wetting for the subsequent aluminum deposition. A previous report demonstrated that PEDOT:PSS on glass improves the reliability of electron-dominated organic diodes [33]. Including this layer also improves the yield and reliability of our inverted top-emitting OLEDs.

poly(3,4-ethylenedioxythiophene) poly(styrenesulfonate)
PEDOT:PSS
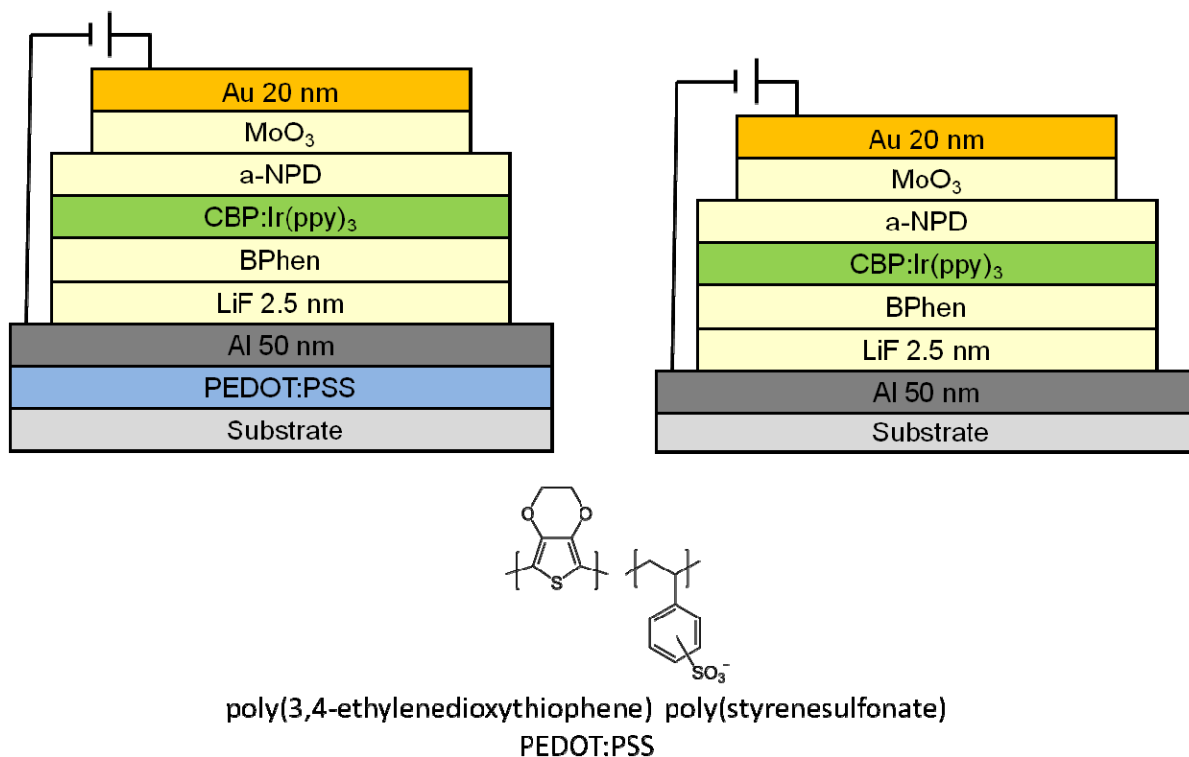
Fig. 4.7. Inverted top-emitting OLEDs with and without a PEDOT:PSS modified glass substrate. The PEDOT:PSS layer is dispensed from solution and requires a substrate annealing step. For details see experimental methods section 4.2.1.
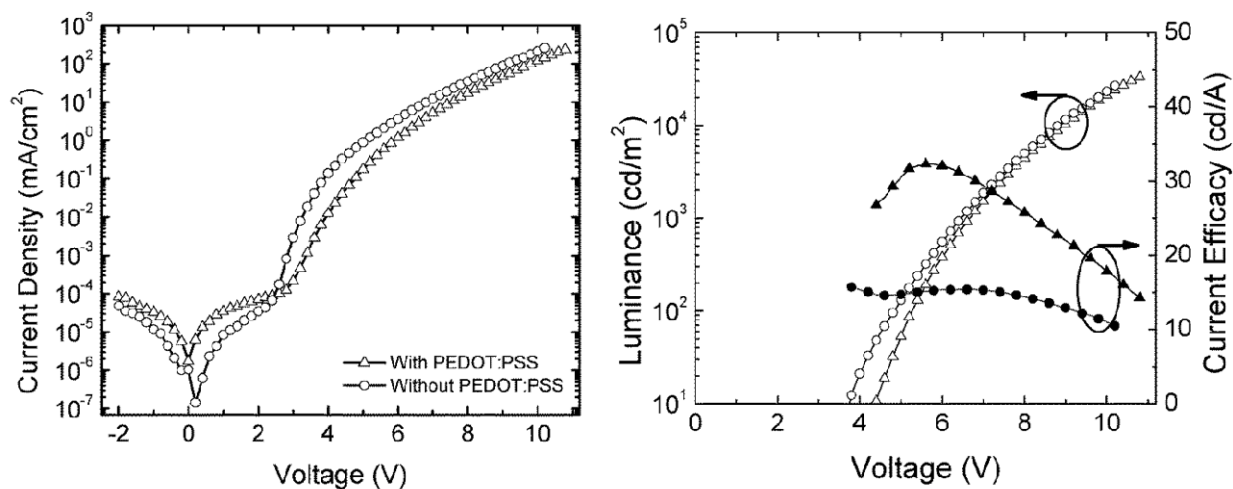
Fig. 4.8. The performance of the inverted top-emitting OLEDs with and without a PEDOT:PSS modified glass substrate. Devices with the PEDOT:PSS layer show considerably higher current efficacies for the same voltages as those without the PEDOT:PSS buffer layer.

Here, we report on highly-efficient green-emitting electrophosphorescent top-emitting OLEDs with Al/LiF bottom cathodes. Devices containing only two organic layers yield a current efficacy of 60.6 cd/A at a luminance of 1,073 cd/m^2 when fabricated on a glass substrate. It has been previously shown that an organic capping layer on the semitransparent electrode of a top-emitting OLED can improve the outcoupling efficiency of the device by modifying the device's optical structure [34].The current efficacy of our devices was increased to 92.5 cd/A at a luminance of 1,300 cd/m^2 with the addition of an N,N′-Di-[(1-naphthyl)-N,N′-diphenyl]-1,1′-biphenyl)-4,4′-diamine (α-NPD) optical outcoupling layer. Devices with such an outcoupling layer were also demonstrated on flexible polyethersulfone (PES) substrates and yielded a current efficacy of 96.3 cd/A at a luminance of 1,387 cd/m^2.

4.2.1 Experimental Methods

Glass micro-slides (VWR international) and PES sheets were cut into 1 × 1 inch squares and used as substrates for the inverted top-emitting OLEDs. The glass substrates were sequentially cleaned by ultrasonication in baths of detergent water, distilled water, acetone, and isopropanol for 20 min each and then blown dry with nitrogen. PES substrates were cleaned and dried by the same process excluding cleaning with acetone. The dry glass and PES substrates were treated by oxygen plasma for 2 min and 5 s, respectively. A layer of PEDOT:PSS Clevios P VP AI 4083 was dispensed through a 0.45 μm polyvinylidine fluoride filter and spin-coated at a speed of 5,000 rpm for 1 min. The substrates were then annealed at 140 °C for 10 min. The thickness of the PEDOT:PSS was 40 nm and measured by spectroscopic ellipsometry.

The samples were then transferred to a high-vacuum thermal evaporation system (EvoVac, Armstrong Engineering Inc.). The OLEDs on either glass or PES substrates were fabricated as separate batches. For all substrates, an aluminum layer of 50 nm was first deposited

at a rate of 2 Å/s followed by a LiF electron-injection layer of 2.5 nm at a rate of 0.2 Å/s. All subsequent organic layers were deposited at a rate of 1 Å/s. A 40 nm-thick layer of 1,3,5-tri(p-pyrid-3-yl-phenyl)benzene (TpPyPB) was used as an ETL. The emissive layer was comprised of a 6 vol. % tris(2-phenylpyridine)iridium(III) Ir(ppy)$_3$ dopant co-evaporated in a 20 nm layer of 4,4′-bis(N-carbazolyl)-1,1′-biphenyl (CBP). A 35 nm hole-transport layer of CBP was then deposited. This was followed by a 15 nm-thick layer of molybdenum trioxide (MoO$_3$) deposited at a rate of 0.2 Å/s as a hole-injection layer. Finally, a 20 nm-thick top Au anode was deposited at a rate of 2 Å/s. The typical OLED area was 4 × 5 mm. To improve the optical outcoupling, an additional 120 nm-thick layer of α-NPD was deposited on top of the anodes of some devices for comparison. All depositions were performed at pressures below 3×10^{-7} Torr. All materials were purchased from Sigma-Aldrich except for TpPyPB and Ir(ppy)$_3$, which were purchased from Luminescence Technology Corporation. The organic materials were purified by gradient-zone sublimation.

After fabrication, the devices were transferred in a sealed nitrogen-containing vessel to another glove box where current-voltage and luminance-voltage characteristics were measured with a Keithley 2400 Source Meter and a calibrated photodiode (FDS 100 from Thorlabs, Inc.). Electroluminescent spectra were measured with a radiometrically calibrated Ocean Optics USB4000 spectrometer.

4.2.2 Results and Discussion

Figure 4.9 shows a plot of the current density versus voltage of the OLEDs. Devices A and B are on glass substrates. Device A has no optical outcoupling layer and device B has an outcoupling layer of 120 nm of α-NPD. The current density versus voltage curves for both devices A and B are nearly identical, showing that the optical outcoupling layer had no effect on

the electrical properties of the devices. In a separate batch, OLEDs were made on PES substrates

also with an outcoupling layer of 120 nm of α-NPD (device C). As shown in Fig. 4.9, these

devices burned out at a lower driving voltage than devices A and B.
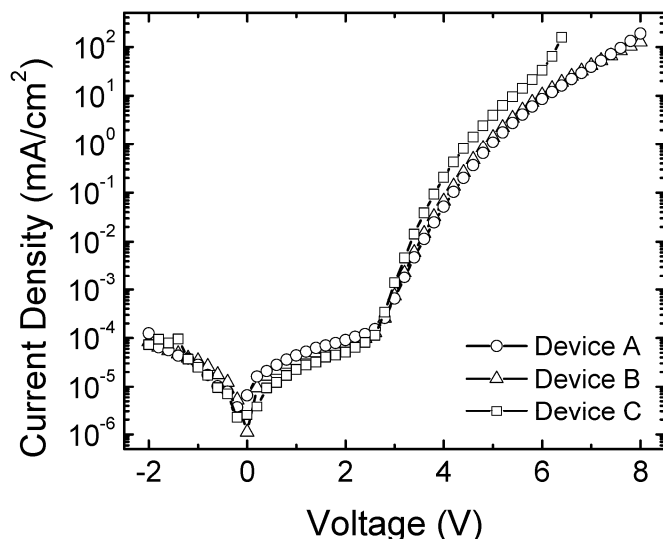
Fig 4.9. Current density versus voltage curves for OLEDs with device structure: Substrate/PEDOT:PSS/Al/LiF/TpPyPB/CBP:Ir(ppy)$_3$/CBP/MoO$_3$/Au. Glass substrates were used for devices A (circles) and B (triangles), with device B having a 120 nm α-NPD optical outcoupling layer. Device C was fabricated on PES and also had an outcoupling layer.

Figure 4.10 shows the luminance and current efficacy curves versus voltage. The turn-on

voltages, maximum current efficacy, and maximum luminance of devices A, B, and C are

summarized in Table 4.1. The device performance of OLEDs on glass substrates has been

verified in four separate batches with multiple OLEDs per batch. The average performance and

standard deviation of OLEDs from these separate batches are shown in Table 4.2.
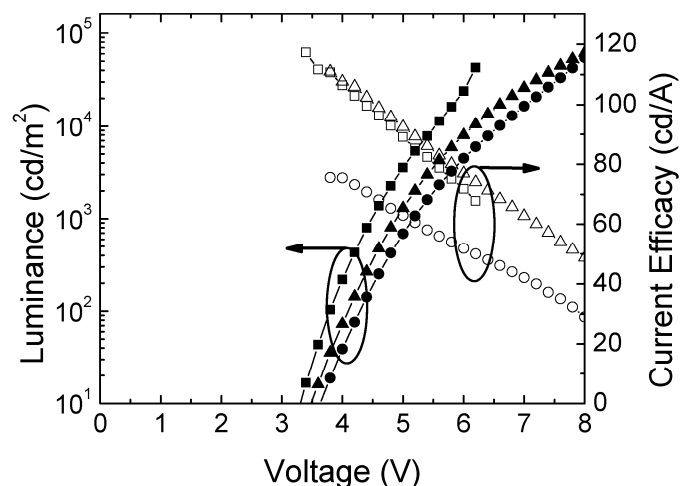
Fig. 4.10. Luminance and current efficacy versus voltage of device A (circles) and device B (triangles) on glass without and with an α-NPD optical outcoupling layer, respectively. Also shown is device C (squares) fabricated on a PES substrate and also having an outcoupling layer.

Table 4.1. Performance parameters of devices A (on glass with no optical outcoupling), B (on glass with outcoupling), and C (on PES with outcoupling). The turn-on voltage is defined as the voltage at a luminance of 10 cd/m^2. The numbers in parentheses reflect the values (luminance or current efficacy) at which the performance parameters being reported are determined.

	Turn-on Voltage [V]	Max Current Efficacy [cd/A]	Max Luminance [mA/cm^2]
Device A	3.6	75.6 (19.0 cd/m^2)	54,656 (29.0 cd/A)
Device B	3.5	111.0 (36.0 cd/m^2)	61,819 (48.8 cd/A)
Device C	3.3	117.0 (16.7 cd/m^2)	43,019 (67.9 cd/A)

Table 4.2. Average performance with standard deviation for OLEDs on glass substrates. The data is taken from four separate batches.

	Luminance [cd/m^2]	Voltage [V]	Current Density [mA/cm^2]	Current Efficacy [cd/A]
Device A (6 devices)	100	4.3 (± 0.1)	0.23 (± 0.04)	58 (± 7)
	1,000	5.2 (± 0.1)	2.4 (± 0.6)	53 (± 5)
	10,000	6.7 (± 0.2)	29 (± 6)	42 (± 8)
Device B (11 devices)	100	3.9 (± 0.2)	0.11 (± 0.02)	108 (± 2)
	1,000	4.7 (± 0.2)	1.5 (± 0.1)	94 (± 7)
	10,000	5.8 (± 0.3)	15 (± 2)	76 (± 2)

These results demonstrate that using a bottom Al/LiF cathode in conjunction with an ETL of TpPyPB and an anode of MoO_3/Au can lead to efficient inverted phosphorescent OLEDs, despite the cathode deposition order being the reverse of what is commonly used in conventional OLEDs. In addition, the MoO_3/Au semi-transparent anode can inject holes directly into the highest occupied molecular orbital (HOMO) of the CBP host (6.3 eV) [35] without necessitating a different hole transport material with a lower HOMO energy level with respect to vacuum. Using CBP as a hole-transport layer has the additional benefits of reducing the number of different materials needed, as well as eliminating an organic-organic heterojunction of dissimilar materials. Furthermore, it is likely that the high efficiency of the OLED is promoted by a combination of desirable properties of the electron transport material, TpPyPB: its lowest unoccupied molecular orbital (LUMO) energy (which corresponds to a measured electron affinity of 3.04 eV) for enhancing electron injection, a HOMO energy (which corresponds to a measured ionization energy of 6.66 eV) for confining holes to the emissive layer, and a high electron mobility (7.9×10^{-3} $cm^2V^{-1}s^{-1}$) as measured by time-of-flight experiments [36].

To compare the efficiency of injecting electrons from a bottom and top Al/LiF cathode, electron-dominated devices were fabricated. The device structure consisted of Glass/PEDOT:PSS (40 nm)/Al (50 nm)/LiF (2.5 nm)/TpPyPB (95 nm)/LiF (2.5 nm)/Al (50 nm). The HOMO level of TpPyPB ensures that hole injection from the Al/LiF electrodes is negligible. The device structure and current density versus voltage curves of these devices are shown in Fig. 4.11a and b, respectively. In Fig. 4.11b, negative voltages and positive voltages correspond to electron injection from the bottom and top electrodes, respectively. The curve shows a slightly higher current (by less than one order of magnitude) when electrons are injected from the top electrode. This asymmetry could be the result of aluminum diffusion into the organic when the

top electrode is deposited. Also shown is a comparison between identical electron-dominated devices where some have been subjected to a vacuum break and subsequently exposed to the glovebox N_2 atmosphere (O_2 <0.1 ppm, H_2O < 3.0 ppm) after the bottom Al/LiF cathode deposition. The current density of the exposed devices decreases by nearly four orders of magnitude when electrons are injected from the bottom. It is possible that the Al/LiF cathode oxidizes when exposed to the trace amounts of O_2 and H_2O in the glovebox atmosphere. If an oxide forms, the insulating property of the oxide may reduce the ability of the cathode to inject electrons. Moreover, an oxide may prevent a chemical reaction from occurring between the ternary system of Al/LiF/TpPyPB. Such a reaction has been shown to occur between Al/LiF/Alq3 resulting in enhanced injection due to the presence of Alq3- radical anions [18],[19]. The high sensitivity of the Al/LiF cathode to trace amounts of O_2 and H_2O may also explain why such cathodes have not been widely implemented in inverted OLED structures.
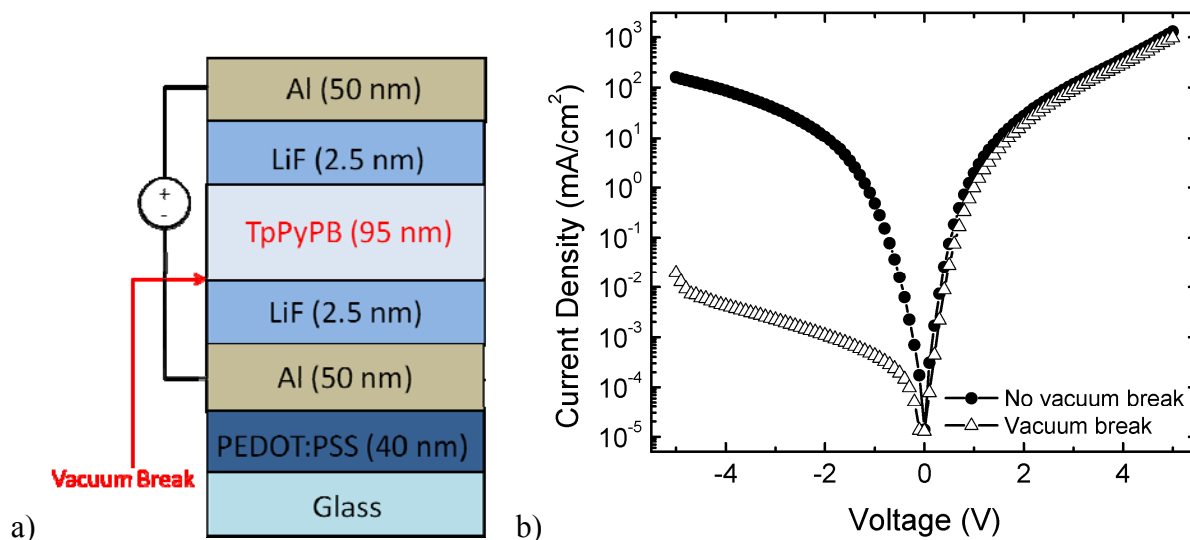
Fig. 4.11. a) Device structure of electron-dominated devices, showing point in device fabrication when vacuum break occurred, and b) Current density versus voltage characteristics of Al/LiF/TpPyPB/LiF/Al electron-dominated devices. Electrons are injected from the top electrode in forward bias and from the bottom in reverse bias.

Figure 4.12 shows the angular electroluminescent spectra of both devices A and B taken at 20° increments from the surface normal. The spectra are normalized to the peak of the spectrum taken normal to the surface. The microcavity formed by the Al and Au layers [37] causes the spectra to narrow and shift with increasing angle causing the color of the OLED to change with the angle-of-view. The CIE coordinates (*x*,*y*) of device A are (0.38, 0.58) at 0° and shift to (0.31, 0.64) at 60°. The addition of the optical outcoupling layer leads to stronger shifting and narrowing of the spectrum. For device B, the CIE coordinates at 0° are (0.33,0.62) and shift to (0.26,0.65) at 60°.
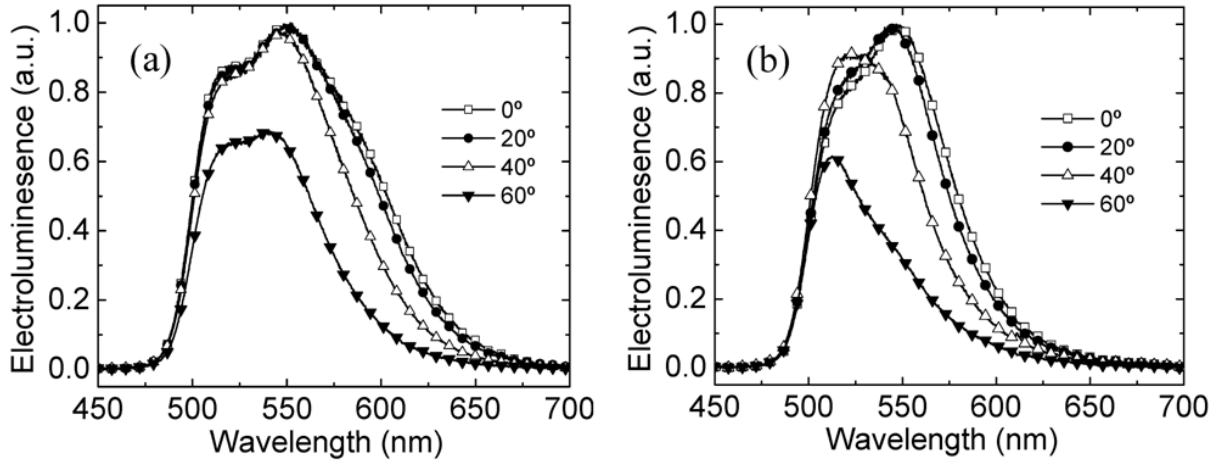
Fig. 4.12. (a) Electroluminescent intensity of device A and (b) device B measured at 20° increments from the surface normal. The measurements are normalized to the maximum intensity of the 0° spectrum.

OLEDs with microcavities cannot be assumed to be Lambertian emitters [38],[39]. Therefore, the external quantum efficiency and power efficacy of the devices cannot be calculated from a single measurement of the luminance in the direction normal to the surface. One way to measure accurate values for these parameters is to capture all of the light emitted

into the forward hemisphere using an integrating sphere. Accurately measuring these quantities could be the focus of future research.

4.2.3 Conclusion

In conclusion, highly efficient phosphorescent top-emitting inverted OLEDs have been demonstrated using a bottom Al/LiF cathode and an electron transport layer of TpPyPB. The OLEDs have a simplified structure containing only two organic layers. On glass, current efficacy of 60.6 cd/A at a luminance of 1,073 cd/m^2 was obtained. This current efficacy was shown to increase to 92.5 cd/A at a luminance of 1,300 cd/m^2 with the addition of an α-NPD optical outcoupling layer. Devices on PES substrates and also having an outcoupling layer show a current efficacy of 96.3 cd/A at a luminance of 1,387 cd/m^2. Future work will be focused on measuring the power efficacy of the devices using an integrating sphere.

4.3 Novel Ag/HATCN Anode for Green Inverted Top-Emitting OLEDs

4.3.1 Background

Reports on inverted top-emitting OLEDs are especially scarce. Not only do they require a highly reflective bottom-cathode capable of effective electron injection, but they also need a top-anode that is both semitransparent and capable of effective hole injection. Various approaches have been used including anodes consisting of sputtered ITO on PEDOT:PSS [23, 29] and pentacene [23] buffer/injection layers, Ag with doped hole-transport layers (HTLs) [24, 25], Au [16], and Ag/molybdenum trioxide (MoO$_3$) [17].

The highest current efficacy previously reported for inverted top-emitting OLEDs was 96.3 cd/A at a luminance of 1,387 cd/m^2 [40]. These OLEDs have a Au/MoO$_3$ anode which

injects holes into an HTL of 4,4′-bis(N-carbazolyl)-1,1′-biphenyl (CBP) [15]. The hole-injection process of transparent conducting oxides (TCO) such as MoO_3 proceeds by the transfer of electrons into the conduction band of the TCO from the highest occupied molecular orbital (HOMO) level of the neighboring HTL. This is the same model used to explain the operation of TCO-containing connecting-units in stacked OLEDs in that the charge-generation process takes place at the TCO/HTL interface [41]. It is for this reason that the material combinations that are used in the charge-generation units of stacked OLEDs can also be used as hole-injection/HTL combinations in single-unit OLEDs.

Like TCOs, 1,4,5,8,9,11-hexaazatriphenylene hexacarbonitrile (HAT-CN) has been used in the connecting-units of stacked OLEDs [42, 43] and a hole-generating organic interlayer in single-unit OLEDs [44] (see Fig. 4.13). HAT-CN is a electron acceptor that has also been used as an *n*-dopant [45] due to its large electron affinity (EA) that has value comparable to that of the ionization energy (IE) of common HTLs. Chiba et al. reported that a combination of a layer of HAT-CN and a layer of 1,1-bis-(4-bis(4-tolyl)-aminophenyl)cyclohexene (TAPC) could be used in highly efficient stacked electrophosphorescent OLEDs [42]. Under the application of an electric field, electrons are transferred from the highest occupied molecular orbital (HOMO) of TAPC (corresponding to an IE of 5.4 eV) [46] to the lowest unoccupied molecular orbital (LUMO) of HAT-CN (corresponding to an EA which has been reported to range from 4.4 eV [42] to 6.0 eV [47]), resulting in the simultaneous creation of holes. Very recently, a thick layer of HAT-CN has been used as a buffer layer for the sputter deposition of an indium zinc oxide anode on a transparent inverted OLED [48].

Here, we present high-performance inverted top-emitting electrophosphorescent OLEDs with a novel Ag/HAT-CN/TAPC anode structure. The use of Ag is more economical than Au

95

and HAT-CN offers the additional benefit of being deposited at a lower temperature (below 350°

C under high vacuum) compared to metal oxides such as MoO_3 [48]. Additionally Au has some

unfavorable optical characteristics for green (and blue) OLEDs. As can be seen in Fig. 4.13, 20

nm of Au reduces the transmittance of Glass/MoO_3 to 50% at the peak emission of Ir(ppy)$_3$.

When used in conjunction with a TAPC hole-transporting layer, devices with an outcoupling

layer of an N,N′-Di-[(1-naphthyl)-N,N′-diphenyl]-1,1′-biphenyl)-4,4′-diamine (α-NPD) achieve a

high current efficacy of 124.7 cd/A at 100 cd/m^2 in addition to exhibiting a low turn-on voltage

of 3.0 V and slight roll-off behavior in current efficacy, yielding an average value of 96.4 cd/A at

a luminance of 10,000 cd/m^2.
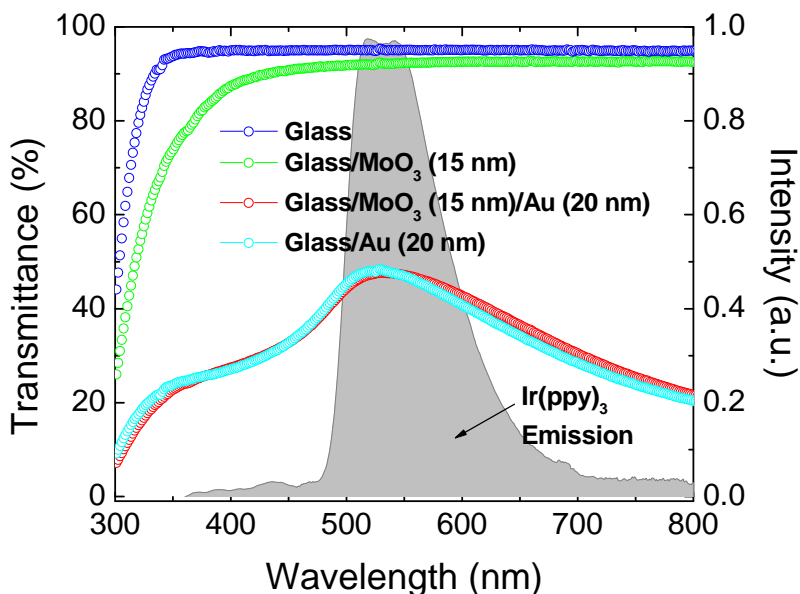
Fig.4.13. Optical Transmittance of MoO_3/Au on glass substrates overlayed with the spectral emission profile of the green phosphorescent emitter Ir(ppy)$_3$ used in the inverted top-emitting OLEDs. It can be seen that 20 nm of Au reduces the transmittance of Glass/MoO_3 to 50% at the peak emission of Ir(ppy)$_3$.

4.3.2 Experimental Methods

Substrates of glass micro-slides (VWR International) were cut into 1×1 inch squares and then cleaned by ultrasonication (5510, Branson Ultrasonics) in baths of detergent water, distilled water, acetone, and isopropanol. The substrates were treated for 20 min in each solvent and then blown dry with nitrogen gas. They were then exposed to oxygen plasma (Plasma-Preen II, Plasmatic Systems, Inc.) for 2 min. Next, PEDOT:PSS Clevios P VP AI 4083 was dispensed onto the substrates through a 0.45 μm polyvinylidene fluoride filter and spin-coated (WS-400B-6NPP/LITE, Laurell Technologies, Inc.) at a speed of 5,000 rpm for 1 min. The substrates were then annealed at 140 °C for 10 min in ambient atmosphere. The thickness of the PEDOT:PSS on glass was measured to be 40 nm-thick by spectroscopic ellipsometry (M-2000UI, J.A. Woollam Co., Inc.). A previous study showed that PEDOT:PSS on glass improves the reliability of electron-dominated organic diodes with bottom metal cathodes [33]. Including this layer also improves the yield and reliability of our inverted top-emitting OLEDs.

The samples were then transferred to a high-vacuum thermal evaporation system (EvoVac, Armstrong Engineering Inc.) and the chamber was pumped down to pressures below 3×10^{-7} Torr. An Al layer of 50 nm thickness was first deposited at a rate of 2 Å/s followed by a LiF electron-injection layer of 2.5 nm thickness at a rate of 0.2 Å/s. All following organic layers were then deposited at a rate of 1 Å/s. A 40 nm-thick electron-transport layer of 1,3,5-tri(p-pyrid-3-yl-phenyl)benzene (TpPyPB) was first deposited. The emissive layer consisting of 6 vol. % tris(2-phenylpyridine)iridium(III) Ir(ppy)$_3$ dopant co-evaporated in a 20 nm-thick layer of CBP was then evaporated, followed by a 35 nm-thick HTL of TAPC. A 5 nm-thick layer of HAT-CN was deposited at a rate of 0.1 Å/s as a hole-injection layer. Finally, a 20 nm-thick top Ag anode was deposited at a rate of 2 Å/s. All materials were evaporated through shadow masks. The

typical OLED area was 4×5 mm^2. To extract additional light from the devices, an 80 nm-thick layer of α-NPD was deposited on the Ag. All materials were purchased from Sigma-Aldrich with the exception of TpPyPB and Ir(ppy)$_3$, which were obtained from Luminescence Technology Corp. All organic materials were purified by gradient-zone sublimation prior to thermal evaporation.

After fabrication, current-voltage and luminance-voltage characteristics were measured using a digital source meter (2400, Keithley Instruments, Inc.) and a calibrated photodiode (FDS 100, Thorlabs, Inc.). The substrates were mounted on a computer-controlled rotating stage (Thorlabs, Inc.) and a radiometrically calibrated spectrometer (USB4000, Ocean Optics, Inc.) was used to measure the OLEDs' electroluminescent spectra.

4.3.3 Results and Discussion

The structure and biasing of these inverted top-emitting OLEDs along with a chemical diagram of HAT-CN are displayed in Fig. 4.14. A plot of the current density versus voltage of the OLEDs is shown in Fig. 4.15. The luminance versus voltage for the devices is displayed in Fig. 4.16 with an inset of the current efficacy versus luminance. These devices have a low turn-on voltage (defined here as the voltage required to achieve a luminance of 10 cd/m^2) of about 3.0 V. This low turn-on voltage is comparable to devices incorporating doped transport layers [25, 49]. The current efficacy is 124.7 cd/A at a practical luminance of 100 cd/m^2 and shows slight roll-off at luminance levels up to 10,000 cd/m^2. The average performance and standard deviation of multiple OLEDs with the same structure are shown in Table 4.3.
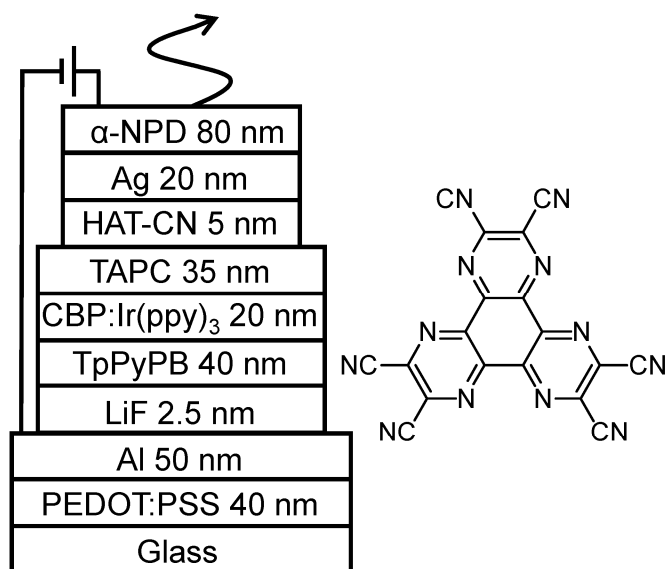
Fig. 4.14. (a) OLED device architecture and (b) HAT-CN chemical structure.
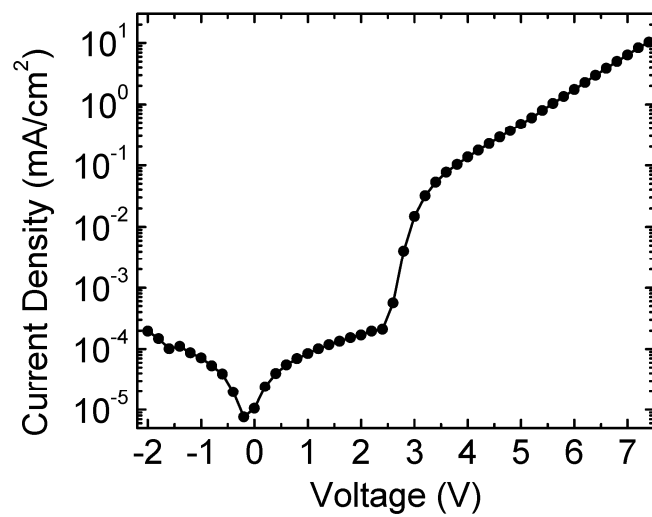
Fig. 4.15. Current density versus voltage characteristics of the top-emitting inverted OLED.
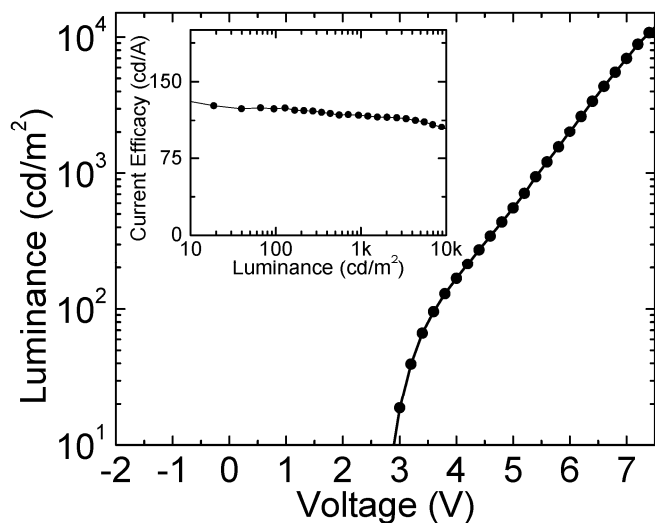
Fig. 4.16. Luminance versus voltage of the inverted top-emitting OLED with current efficacy versus luminance as an inset.

Table 4.3 Average performance and standard deviation of four inverted top-emitting OLEDs.

Luminance [cd/m^2]	Voltage [V]	Current Density [mA/cm^2]	Current Efficacy [cd/A]
100	3.8 ± 0.0	0.10 ± 0.01	119.0 ± 4.2
1,000	5.6 ± 0.0	1.01 ± 0.04	110.3 ± 8.2
10,000	7.4 ± 0.0	10.48 ± 0.92	96.4 ± 10.1

Hole-dominated devices were also fabricated to compare the effectiveness of injecting holes from a top Ag/HAT-CN/TAPC electrode structure versus an Ag electrode without HAT-CN. The device structure was Glass/ITO/PEDOT:PSS (40 nm)/TAPC (200 nm)/ HAT-CN (0 or 5 nm)/Ag (70 nm). The difference in the ITO/PEDOT:PSS work function (5.3 eV) [50] and the electron affinity of TAPC (1.84 ± 0.15 eV) [51] ensures that electron injection from the ITO electrode is negligible. The device architectures and current density versus voltage curves of these devices are shown in Fig. 4.17a, b, and c, respectively. In 4.17c positive voltages represent hole injection from the top electrode. Devices with HAT-CN show an increase in current density of up to three orders of magnitude over devices with only Ag. It has been previously reported in

[52] that HAT-CN can increase the work function of Ag(111) by up to 1.0 eV from a value of 4.4 eV to 5.4 eV. This modified work function value would match that of the ionization energy of TAPC (5.4 eV), leading to effective hole injection of Ag/HAT-CN into TAPC (see Fig. 4.17c). This effect can explain why the hole-injecting and transport combination of Ag/HAT-CN/TAPC, when used in conjunction with the effective electron-injecting and transport combination of Al/LiF/TpPyPB, results in good carrier balance and high current efficacy in the inverted top-emitting OLEDs.

(a)   (b)

(c)

Vacuum Level

Energy

Ag
4.4 eV
Work Function

Vacuum Level

1.8 eV   Electron Affinity

5.4 eV$^{(1)}$ 5.4 eV$^{(2)}$ Ionization Energy

TAPC

Ag/HAT-CN

[1]Appl. Phys. Lett.
97 (2010), p. 253308

[2]Appl. Phys. Lett.
72 (1998), pp. 864–866
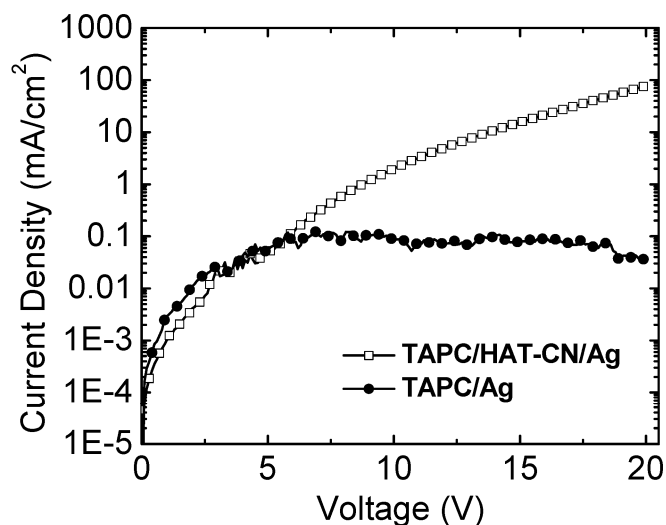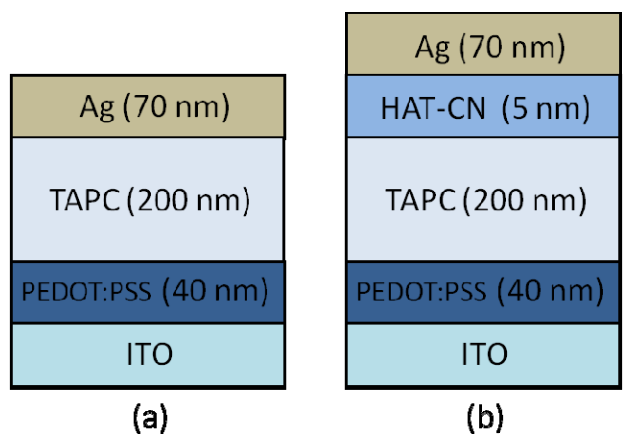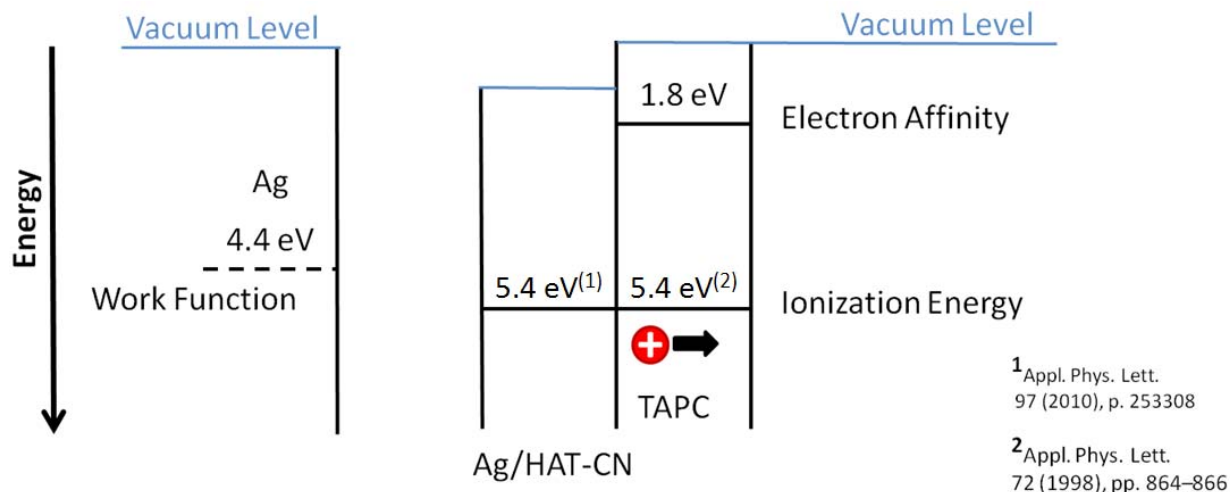
(d)

Fig. 4.17. a) Reference hole-dominated devices and b) hole-dominated devices with a 5 nm-thick layer of HAT-CN as a HIL. c) Current density versus voltage curves of hole-dominated devices. Holes are injected from the top contact in forward bias. The current density is increased by over three orders of magnitude when 5 nm of HAT-CN is used as a hole-injection layer. d) Potential mechanism for enhanced hole-injection current from the HAT-CN. HAT-CN has been shown to modify the work-function of the Ag and therefore, match the ionization energy of TAPC (5.4 eV), leading to effective hole injection of Ag/HAT-CN into TAPC.

Figure 4.18 shows the angular electroluminescent spectra of an inverted top-emitting OLED taken at 20° increments from the surface normal. The spectra are normalized to the maximum of the spectrum measured at normal incidence from the OLED surface. The microcavity [37] formed by the Al and Ag layers causes the spectrum to narrow and shift with increasing angle. This leads to changes in the color of the OLED with changes in the angle-of-view. The inset of Fig. 4.18 shows the change in the Commission Internationale de l'Eclairage (CIE) color coordinates with increasing angle-of-view. In these OLEDs, microcavity effects lead to a non-Lambertian emission pattern. This is clearly demonstrated in Fig. 4.19 where a plot of the electroluminescent intensity of the OLED (normalized to the maximum of 0° spectrum) at a fixed wavelength versus viewing angle shows a clear deviation from a Lambertian emission pattern. The observed color change with angle-of-view and the effects on the emission pattern

are characteristic of top-emitting OLEDs. However, these effects can be reduced through the use

of a light-scattering layer [53].
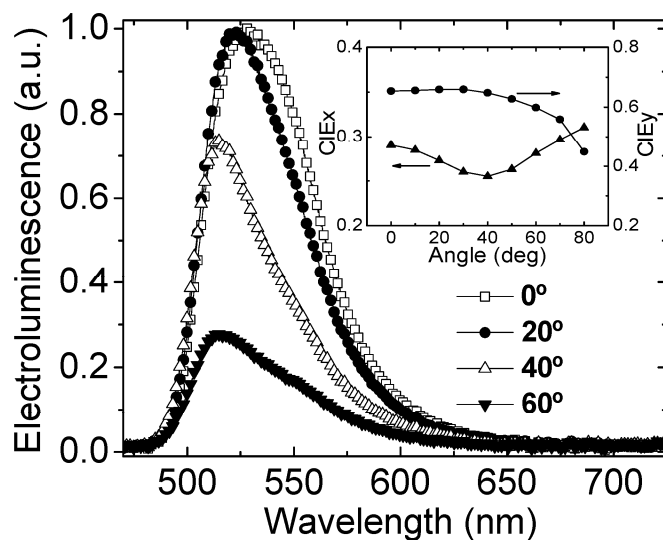
Fig. 4.18. Electroluminescent intensity of the inverted top-emitting OLED measured at 20° increments from the surface normal, normalized to the greatest intensity of the 0° spectrum. The inset shows the CIE coordinates versus angle.
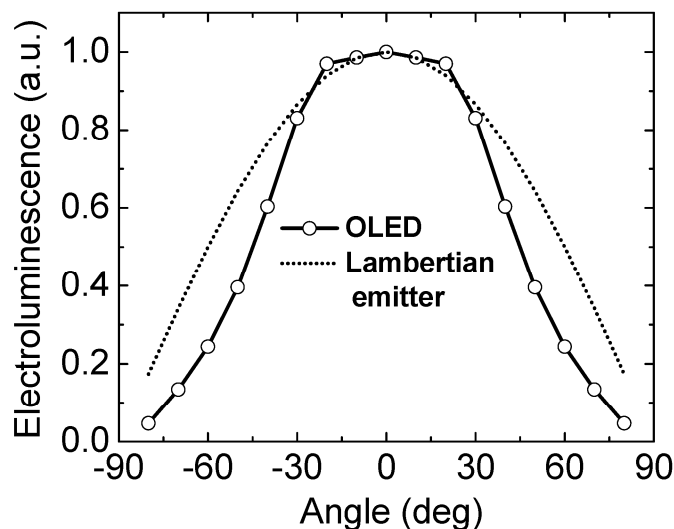
Fig. 4.19. Intensity of the OLED normalized to the maximum of 0° spectrum at fixed wavelength versus viewing angle. The OLED shows a clear deviation from a Lambertian emission pattern due to microcavity effects.

4.3.4 Conclusion

In summary, highly efficient inverted top-emitting electrophosphorescent OLEDs have been demonstrated using a novel top anode structure of Ag/HAT-CN/TAPC. The devices had a low turn on voltage of 3.0 V and a high current efficacy of 124.65 cd/A at a luminance of 100 cd/m^2. The current efficacy showed very little roll-off, yielding values of 96.4 cd/A at a luminance of 10,000 cd/m^2. In future work the power efficacy and external quantum efficiency of the devices will be measured using an integrating sphere.

4.4 Inverted Top-Emitting OLEDs on Nanocellulose Substrates

4.4.1 Background

Organic light-emitting diodes (OLEDs) are an attractive technology for future low-cost, flexible lighting and display applications. OLEDs have been traditionally fabricated on rigid glass substrates. Flexible OLEDs have also been fabricated on polyethylene terephthalate (PET) and polyethersulfone (PES) [54],[55]. However these plastic substrates are petroleum-based and expensive. Additionally, they are not as environmentally friendly as recyclable or biodegradable substrates, because plastic is not as susceptible to biodegradation as natural materials. For example, it takes over 30 years to decompose a plastic film container and 450 years to degrade a plastic bottle, while it takes only a few weeks to breakdown a paper towel [56]. Substrate materials that are derived from renewable feedstocks (such as wood) at a low cost could support OLED technology with a reduced environmental impact.

Cellulose nanomaterials (CNs) are cellulose-based nanomaterials with a host of useful properties. They have high aspect ratio, low density, low thermal expansion surfaces which can be readily chemically functionalized, low toxicity, renewability, and the potential to be scaled up to industrial quantities. CNs have been researched for potential applications outside organic electronics. This includes application in reinforcement phases in polymer composites, protective coatings, barrier and filter membrane systems, antimicrobial films, and network structures for tissue engineering [57-65].   Recently, we have successfully demonstrated organic solar cells on cellulose nanocrystal (CNC) substrates that achieve the same power conversion efficiency values (3.8 %) than solar cells fabricated on PES substrates. Furthermore, we have shown that organic solar cells on CNC substrates can be easily separated into their major components using low-energy processes at room temperature [66].

In Fig. 4.20, a hierarchical breakdown of wood from the tree level to the CNCs is shown. CNs can be extracted from plants in two different forms. One is cellulose nanocrystals (CNCs, which are 3–10 nm wide by 50–500 nm in length) and the other is cellulose nanofibers (CNFs, which are 4–20 nm wide by > 1 μm in length). Neat and polymer composite films produced from CNCs and CNFs can be made into substrates for organic electronic devices. They have favorable properties such as low density (1–1.5 g/cm^3) with high tensile strength (30–240 MPa), high elastic modulus (6–30 GPa) and low coefficient of thermal expansion (CTE, 2–25 ppm/K) [61],[67],[64],[68]. CNCs are also found to be readily thermally stable up to 210°C, and after processing optimization, up to 350°C. This yields good compatibility with organic semiconductor processing [65].
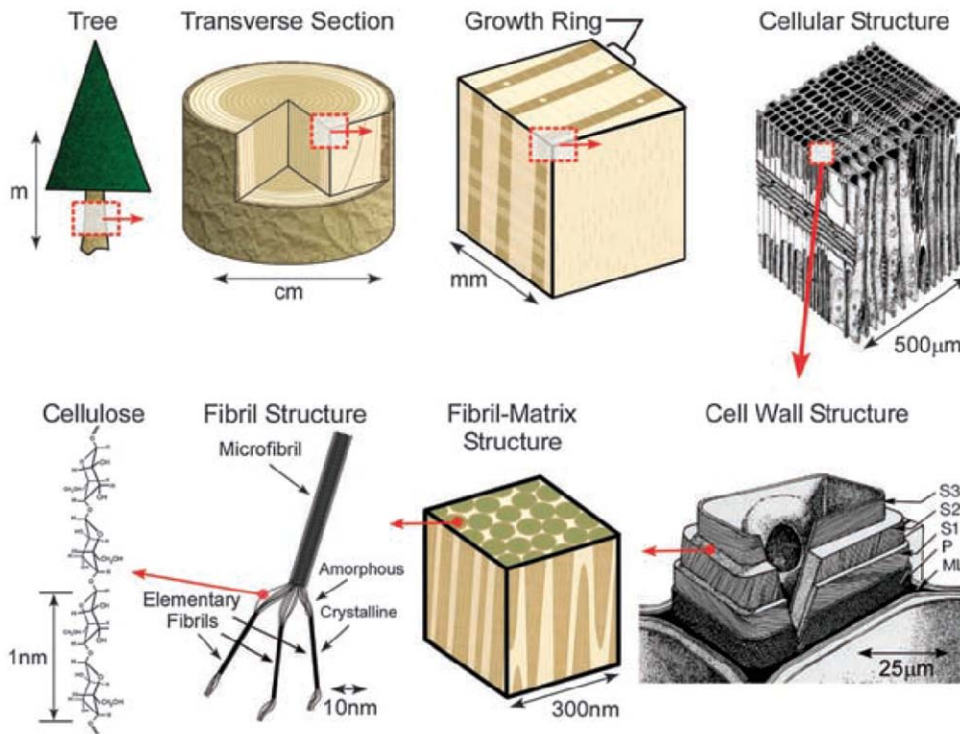
Fig. 4.20. Hierarchical breakdown of wood from the tree level to the CNCs. Here ML stands for middle lamellae between tracheids, P stands for primary cell wall, and S(1-3) represents the cell wall layers. Taken from [69].

To date, few reports exist on OLEDs fabricated upon cellulose substrates such as paper. Legnani et al. first prepared substrates from bacterial cellulose sheet deposited with SiO_2 for fluorescent OLEDs. The OLEDs used radio frequency magnetron sputtered indium tin oxide (ITO) on the SiO_2 to protect the underlying cellulose from damage. They achieved a maximum luminance of 1200 cd/m^2 [70]. Okahisa et al. fabricated substrates from matrix acrylic resin reinforced acetylated wood–cellulose nanocomposites and showed a photograph of a working OLED with no performance data [71]. S. Ummartyotin et al. [72] developed a nanocomposite film composed of bacterial cellulose and a polyurethane based resin as a substrate for flexible OLED displays. Unfortunately polyurethane is derived from petroleum. They reported a maximum current efficacy of 0.09 cd/A at a maximum luminance of 200 cd/m^2.

OLED research in general has mostly investigated structures in which the organic layers are sandwiched between a bottom hole-injecting anode and a top electron-injecting cathode [5],[15]. Conventional OLEDs are often bottom-emitting meaning that the generated light exits the OLED through a semi-transparent anode and transparent substrate, such as an ITO-coated glass. Emitting light through these layers leads to undesirable waveguide losses from both ITO and substrate modes [16]. In top-emitting OLEDs, the cathode is usually a reflective metal and the anode consists of either a transparent conductive oxide [23]. or a semitransparent thin metal layer [24],[25]. Top-emitting devices avoid the light-trapping and waveguiding losses of devices that emit through ITO-coated glass substrates [73]. Moreover, the top-emitting architecture can be easily fabricated on a variety of substrates, including opaque substrates such as those based on cellulose nanocrystals. The use of an Al/lithium fluoride (LiF) bottom-cathode has already been

demonstrated in high-performance green [40] and blue inverted (bottom-cathode, top-anode) top-emitting OLEDs [74].

Here efficient inverted top-emitting green electrophosphorescent OLEDs on free-standing transparent CNC substrates are demostated. The OLEDs are fabricated with Al/LiF bottom electrode on top of a 400 nm-thick N,N'-Di-[(1-naphthyl)-N,N'-diphenyl]-(1,1'-biphenyl)-4,4'-diamine (α-NPD) buffered CNC substrates, with MoO_3/Au as the top electrode. The OLEDs on CNCs show a maximum luminance of 74,591 cd/m^2 and maximum current efficacy 53.7 cd/A at a luminance of 100 cd/m^2 and 41.7 cd/A at 1000 cd/m^2. The average current efficacy of OLEDs on CNCs was 32.5 ± 14.1 cd/A at 10 cd/m^2 and 42.7 ± 9.8 cd/A at 100 cd/m^2. This was similar to the average performance achieved on glass substrates, which was 38.0 ± 19.3 cd/A at a luminance of 10 cd/m^2 and 45.5 ± 10.0 at 100 cd/m^2, for 8 devices made in the same batch as the OLEDs on CNC substrates.

A key advantage of the OLEDs on the CNC substrates is that they can be easily dissolved at room temperature by simple immersion in water. The dissolution of the CNC substrate in distilled water leads to a separation of the OLED into constituent organic semiconducting materials and metal layers which can be filtered out and recycled.

4.4.2 Experimental Methods

The CNCs were produced at USDA Forest Service-Forest Products Laboratory (Madison, WI) using procedures described by Beck-Candanedo et al. [75]. CNC suspensions were produced by sulfuric acid hydrolysis of softwood pulp (64% sulfuric acid, 8:1 acid to pulp weight ratio, 45°C, 60 minutes) followed by quenching with deionized water, centrifuge rinsing, washing, and then dialysis for a week to remove any remaining acid. The suspension was then ultrasonicated

to disperse the CNCs with mechanical agitation and centrifuged a final time for macroparticle removal. CNC films for substrates were prepared by mixing 1.65 wt. % CNC suspension (30 g) with 1 wt. % glycerol solution (4.95 g) for 24 hours. Glycerol (Sigma Aldrich) was added to make the films more flexible for handling. The homogeneous glycerol/CNC water suspension was then poured into 80 mm diameter plastic Petri dishes and allowed to dry at 23°C and 30%–40% relative humidity.

The dried films were detached from Petri dishes and cut into 1 x 1 in. substrates. These films were placed on polydimethylsiloxane-coated glass substrates for mechanical support during OLED fabrication and testing. Glass micro-slides (VWR international) were also cut into 1×1 in. squares and used as reference substrates for the inverted top-emitting OLEDs. The glass substrates were sequentially cleaned by ultrasonication (5510, Branson Ultrasonics) in baths of detergent water, distilled water, acetone, and isopropanol for 20 min each and then blown dry with nitrogen.

The glass and CNC samples were transferred to a high-vacuum thermal evaporation system (EvoVac, Armstrong Engineering Inc.) and evacuated to pressure below 3×10^{-7} Torr. The OLEDs on glass and CNC substrates were fabricated in the same batch. For all substrates, a 400 nm thick layer of α-NPD was first deposited at a rate of 1 Å/s. This is thought to provide a smooth surface for the subsequent cathode layer. Next, an aluminum layer of 50 nm was deposited at a rate of 2 Å/s followed by a LiF electron-injection layer of 2.5 nm at a rate of 0.2 Å/s. All subsequent organic layers were deposited at a rate of 1 Å/s. A 40 nm-thick layer of 1,3,5-tri(*p*-pyrid-3-yl-phenyl)benzene (TpPyPB) was used as an electron transport material. The emissive layer was composed of a 6 vol. % tris(2-phenylpyridine)iridium(III) Ir(ppy)₃ dopant co-

evaporated in a 20 nm layer of 4,4′-bis(N-carbazolyl)-1,1′-biphenyl (CBP). A 35 nm hole-transport layer of CBP was then deposited. This was followed by a 15 nm-thick layer of molybdenum trioxide (MoO_3) deposited at a rate of 0.2 Å/s as a hole-injection layer. Finally, a 20 nm-thick semitransparent top Au anode was deposited at a rate of 2 Å/s. The typical OLED area was 4×5 mm. All depositions were performed at pressures below 3×10^{-7} Torr. All materials were purchased from Sigma-Aldrich except for TpPyPB and Ir(ppy)$_3$, which were purchased from Luminescence Technology Corporation. The organic materials were purified by gradient-zone sublimation prior to thermal evaporation.

Current-voltage and luminance-voltage characteristics were measured with a source meter (Keithley 2400) and a calibrated photodiode (FDS 100 Thorlabs, Inc.). Electroluminescent spectra were measured with a radiometrically calibrated spectrometer (Ocean Optics USB4000).

4.4.3 Results and Discussion

Figure 4.21 depicts the device structure and a plot of the current density versus voltage of the OLEDs built on CNC substrates with a 400 nm-thick α-NPD buffer layer and reference devices without this layer. It can be observed that the current level of the substrate without the buffer layer is much higher than those with the buffer layer. Figure 4.22 shows the luminance and current efficacy curves versus voltage. The data in Figs. 1 and 2 show that the OLED on α-NPD offers much higher current efficacy, lower turn-on voltage, and higher luminance than the OLED built directly on CNC. The average device performance with standard deviations of 15 OLEDs on α-NPD buffered CNC substrates are shown in Table 1.
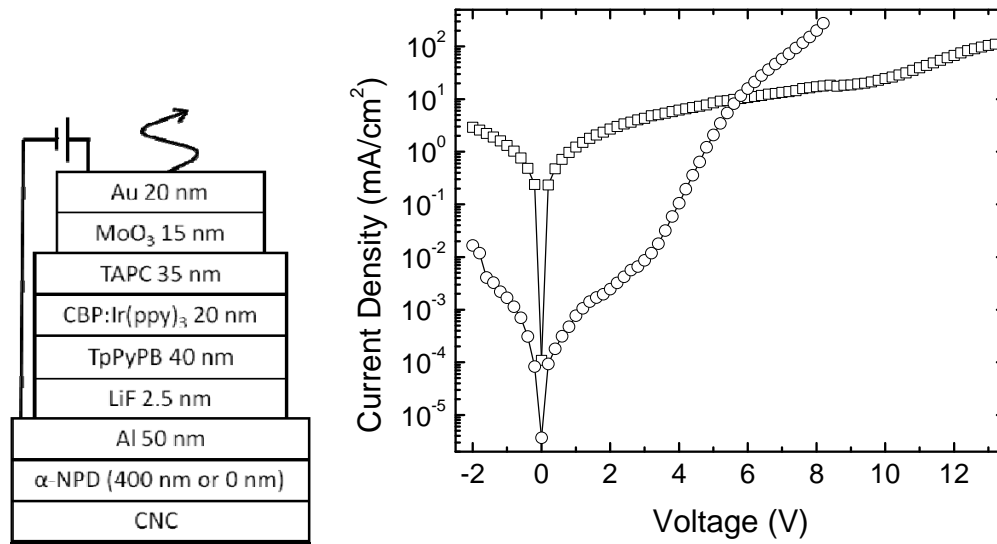
Fig 4.21. Device structure (a) and (b) current density versus voltage curves for OLEDs with device structure: CNC/α-NPD/Al/LiF/TpPyB/CBP:Ir(ppy)$_3$/CBP/MoO$_3$/Au. Open squares refer to devices with the α-NPD and open circles refer to devices without the α-NPD layer.
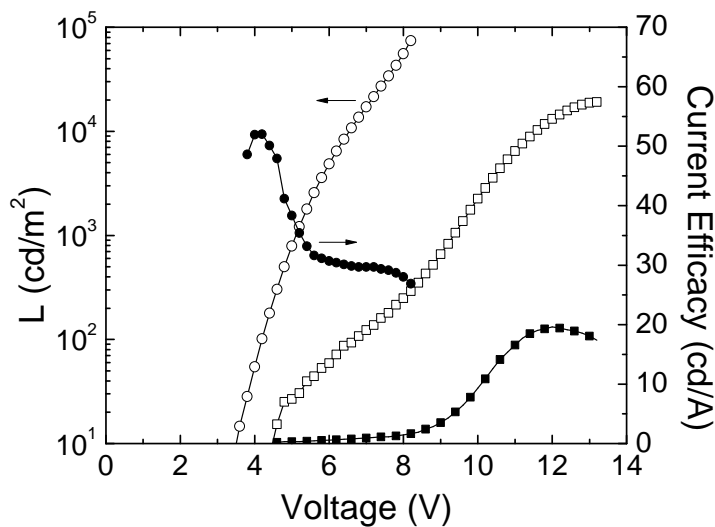
Fig. 4.22. Luminance and current efficacy versus voltage of OLEDs on CNC substrates with α-NPD (circles) and without α-NPD (squares).

Table 4.4. Average performance and standard deviation of 15 inverted top-emitting OLEDs on CNC substrates.

Luminance [cd/m^2]	Voltage [V]	Current Density [mA/cm^2]	Current Efficacy [cd/A]
10	3.5 ± 0.1	0.06 ± 0.05	33 ± 14
100	4.3 ± 0.1	0.27 ± 0.08	43 ± 10
1000	5.1 ± 0.1	4 ± 1	32 ± 6

111

Figure 4.23 shows the angular electroluminescent spectra of the OLEDs on CNC

substrates buffered with a 400 nm-thick α-NPD. These measurements are taken at 20°

increments from the surface normal. All spectra are normalized to the peak value of the normal

spectrum. There is a microcavity that is formed by the Al and Au layers [37], which leads to

spectral narrowing. Furthermore, the spectra shift with increasing angle causing the color of the

OLED to change with the angle-of-view. Hence the CIE coordinates (x, y) of device A are (0.41,

0.55) at 0° and shift to (0.36, 0.60) at 60°. These microcavity effects can be mitigated to a degree

by employing a light scattering layer [53].
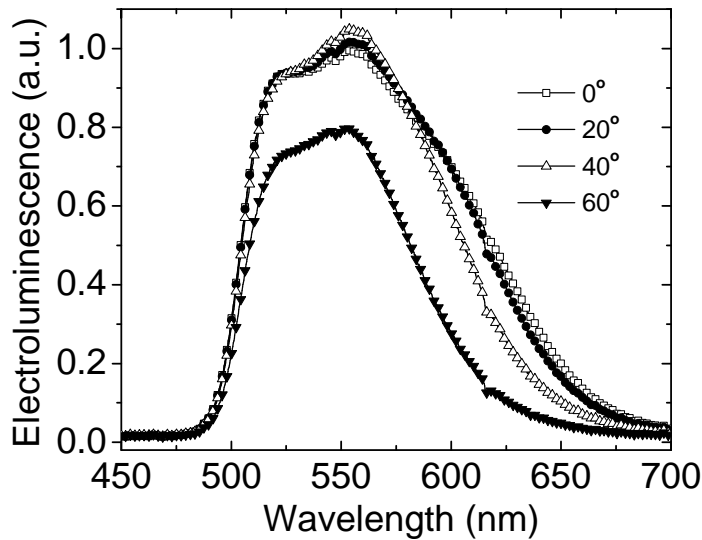
Fig. 4.23. Electroluminescent intensity of an OLED device on a CNC substrate with α-NPD.
Spectra are measured at 20° increments from the surface normal. The measurements are
normalized to the maximum intensity of the 0° spectrum.

A photograph of five inverted top-emitting OLEDs on a CNC substrate mounted on glass,

and an illuminated OLED on CNC can be seen in Fig. 4.24. See figures 4.25 and 4.26 for

photographs of filtered flakes of the constituent OLED on filter paper and the solution after

filtering, respectively.
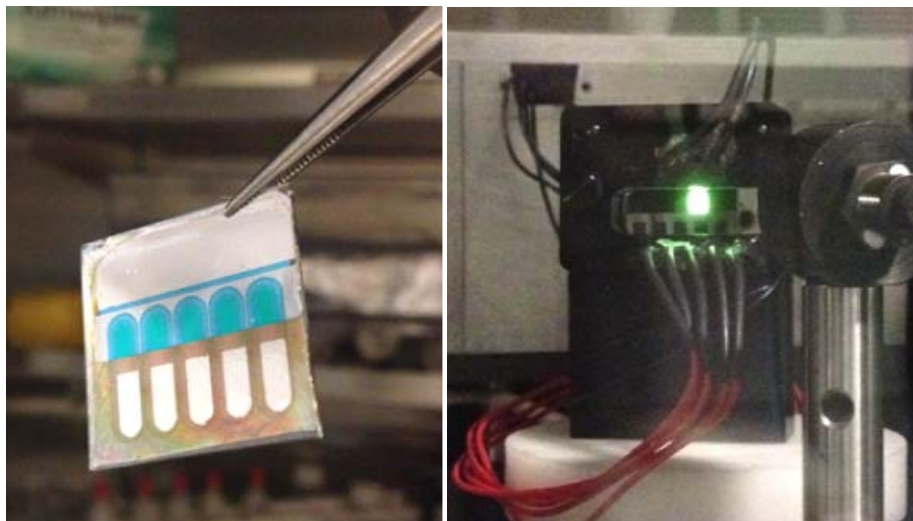
Fig. 4.24. Photograph of five inverted top-emitting OLED devices on a CNC substrate mounted on glass (left), and a working OLED device on CNC substrate (right).

Fig. 4.25. Dried filter paper showing flakes of OLED constituents.

Fig. 4.26. The remaining solution after filtering. All macroscopic flakes of OLED constituents have been removed through the filtering process.

4.4.4 Conclusion

In conclusion, efficient phosphorescent top-emitting inverted OLEDs on CNC substrates have been demonstrated using a bottom Al/LiF cathode on top of a 400 nm α-NPD organic buffer layer. On CNC, a maximum current efficacy of 53.7 cd/A at a luminance of 100 cd/m^2, and 41.7 cd/A at 1,000 cd/m^2 were obtained. The average current efficacy of devices on CNCs was 32.5 ± 14.1 cd/A at 10 cd/m^2 and 42.7 ± 9.8 cd/A at 100 cd/m^2, similar that achieved on glass substrates, 38.0 ± 19.3 cd/A at a luminance of 10 cd/m^2 and 45.5 ± 10.0 at 100 cd/m^2, for 8 devices made in the same batch as the OLEDs on α-NPD buffered CNC substrates. This research is a step towards future low-cost, low-weight, flexible, and recyclable electronics based on cellulose nanomaterial substrates.

4.5 References

[1] H. J. Round, "A note on carborundum", Electrical World, vol. 19, pp. 309, 1907. .

[2] A. Bernanose, Electroluminescence of organic compounds, British Journal of Applied Physics, 6 (1955) S54.

[3] M. Schadt, D.F. Williams, Low-Temperature Hole Injection and Hole Trap Distribution in Anthracene, The Journal of Chemical Physics, 50 (1969) 4364-4368.

[4] H.P. Kallmann, M. Pope, Theory of Hole Injection and Conductivity in Organic Materials, The Journal of Chemical Physics, 36 (1962) 2482-2485.

[5] C.W. Tang, S.A. VanSlyke, Organic electroluminescent diodes, Applied Physics Letters, 51 (1987) 913-915.

[6] H. Shirakawa, E.J. Louis, A.G. MacDiarmid, C.K. Chiang, A.J. Heeger, Synthesis of electrically conducting organic polymers: halogen derivatives of polyacetylene,(CH) x, Journal of the Chemical Society, Chemical Communications, (1977) 578-580.

[7] C.K. Chiang, C.R. Fincher, Jr., Y.W. Park, A.J. Heeger, H. Shirakawa, E.J. Louis, S.C. Gau, A.G. MacDiarmid, Electrical Conductivity in Doped Polyacetylene, Physical Review Letters, 39 (1977) 1098-1101.

[8] J.H. Burroughes, D.D.C. Bradley, A.R. Brown, R.N. Marks, K. Mackay, R.H. Friend, P.L. Burns, A.B. Holmes, Light-emitting diodes based on conjugated polymers, Nature, 347 (1990) 539-541.

[9] M. Abkowitz, I. Chen, J.H. Sharp, Electron Spin Resonance of the Organic Semiconductor, alpha -Copper Phthalocyanine, The Journal of Chemical Physics, 48 (1968) 4561-4567.

[10] N. Almeleh, S.E. Harrison, Trapping effects in the organic semiconductor triphenylene, Journal of Physics and Chemistry of Solids, 27 (1966) 893-901.

[11] J. McGinness, P. Corry, P. Proctor, Amorphous semiconductor switching in melanins, Science, 183 (1974) 853-855.

[12] Y. Yuan, G. Giri, A.L. Ayzner, A.P. Zoombelt, S.C.B. Mannsfeld, J. Chen, D. Nordlund, M.F. Toney, J. Huang, Z. Bao, Ultra-high mobility transparent organic thin film transistors grown by an off-centre spin-coating method, Nature communications, 5 (2014).

[13] P.G. Le Comber, W.E. Spear, Electronic transport in amorphous silicon films, Physical Review Letters, 25 (1970) 509-511.

[14] C. Adachi, M.A. Baldo, M.E. Thompson, S.R. Forrest, Nearly 100% internal phosphorescence efficiency in an organic light-emitting device, J. Appl. Phys., 90 (2001) 5048-5051.

[15] M.G. Helander, Z.B. Wang, J. Qiu, M.T. Greiner, D.P. Puzzo, Z.W. Liu, Z.H. Lu, Chlorinated Indium Tin Oxide Electrodes with High Work Function for Organic Device Compatibility, Science, 332 (2011) 944-947.

[16] K.H. Kim, S.Y. Huh, S.M. Seo, H.H. Lee, Inverted top-emitting organic light-emitting diodes by whole device transfer, Org. Electron., 9 (2008) 1118-1121.

[17] Q. Wang, Z.Q. Deng, D.G. Ma, Highly efficient inverted top-emitting organic light-emitting diodes using a lead monoxide electron injection layer, Opt. Express, 17 (2009) 17269-17278.

[18] M. Mason, Interfacial chemistry of Alq3 and LiF with reactive metals, J. Appl. Phys., 89 (2001) 2756.

[19] K.R. Choudhury, J.H. Yoon, F. So, LiF as an n-dopant in tris(8-hydroxyquinoline) aluminum thin films, Adv. Mater., 20 (2008) 1456.

[20] T. Mori, H. Fujikawa, S. Tokito, Y. Taga, Electronic structure of 8-hydroxyquinoline aluminum/LiF/Al interface for organic electroluminescent device studied by ultraviolet photoelectron spectroscopy, Appl. Phys. Lett., 73 (1998) 2763-2765.

[21] L.S. Hung, C.W. Tang, M.G. Mason, Enhanced electron injection in organic electroluminescence devices using an Al/LiF electrode, Appl. Phys. Lett., 70 (1997) 152-154.

[22] V. Bulovic, P. Tian, P.E. Burrows, M.R. Gokhale, S.R. Forrest, M.E. Thompson, A surface-emitting vacuum-deposited organic light emitting device, Applied Physics Letters, 70 (1997) 2954-2956.

[23] T. Dobbertin, O. Werner, J. Meyer, A. Kammoun, D. Schneider, T. Riedl, E. Becker, H.H. Johannes, W. Kowalsky, Inverted hybrid organic light-emitting device with polyethylene dioxythiophene-polystyrene sulfonate as an anode buffer layer, Appl. Phys. Lett., 83 (2003) 5071-5073.

[24] C.W. Chen, C.L. Lin, C.C. Wu, An effective cathode structure for inverted top-emitting organic light-emitting devices, Appl. Phys. Lett., 85 (2004) 2469-2471.

[25] M. Thomschke, S. Hofmann, S. Olthof, M. Anderson, H. Kleemann, M. Schober, B. Lussem, K. Leo, Improvement of voltage and charge balance in inverted top-emitting organic electroluminescent diodes comprising doped transport layers by thermal annealing, Appl. Phys. Lett., 98 (2011) 083304.

[26] S.F. Chen, L.L. Deng, J. Xie, L. Peng, L.H. Xie, Q.L. Fan, W. Huang, Recent Developments in Top-Emitting Organic Light-Emitting Diodes, Adv. Mater., 22 (2010) 5227-5239.

[27] C.C. Wu, C.W. Chen, C.L. Lin, C.J. Yang, Advanced Organic Light-Emitting Devices for Enhancing Display Performances, J. Disp. Technol., 1 (2005) 248-266.

[28] Q. Wang, F.X. Wang, X.F. Qiao, D.G. Ma, Lead(IV) dioxide: an effective electron injection material to realize high-efficiency inverted top-emitting organic light-emitting diodes, Semicond. Sci. Technol., 24 (2009) 105027.

[29] M. Kroger, T. Dobbertin, D. Schneider, T. Rabe, E. Becker, H.H. Johannes, W. Kowalsky, Highly efficient guest-host-systems for hybrid inverted organic light-emitting diodes with sputtered indium-tin-oxide anodes, Org. Light-Emit. Mater. and Devices Viii 2004, pp. 143-152.

[30] T. Matsushima, K. Goushi, C. Adachi, Charge-carrier injection characteristics at organic/organic heterojunction interfaces in organic light-emitting diodes, Chem. Phys. Lett., 435 (2007) 327-330.

[31] H.J. Bolink, H. Brine, E. Coronado, M. Sessolo, Phosphorescent Hybrid Organic–Inorganic Light-Emitting Diodes, Adv. Mater., 22 (2010) 2198-2201.

[32] M. Sessolo, H.J. Bolink, Hybrid Organic–Inorganic Light-Emitting Diodes, Adv. Mater., 23 (2011) 1829-1845.

[33] R. Steyrleuthner, S. Bange, D. Neher, Reliable electron-only devices and electron transport in n-type polymers, J. Appl. Phys., 105 (2009) 064509.

[34] Q. Huang, K. Walzer, M. Pfeiffer, K. Leo, M. Hofmann, T. Stubinger, Performance improvement of top-emitting organic light-emitting diodes by an organic capping layer: An experimental study, J. Appl. Phys., 100 (2006) 064507.

[35] A. Kahn, N. Koch, W.Y. Gao, Electronic structure and electrical properties of interfaces between metals and pi-conjugated molecular films, J. Polym. Sci. B-Polym. Phys., 41 (2003) 2529-2548.

[36] S.J. Su, T. Chiba, T. Takeda, J. Kido, Pyridine-containing triphenylbenzene derivatives with high electron mobility for highly efficient phosphorescent OLEDs, Adv. Mater., 20 (2008) 2125-+.

[37] S. Hofmann, M. Thomschke, P. Freitag, M. Furno, B. Lussem, K. Leo, Top-emitting organic light-emitting diodes: Influence of cavity design, Appl. Phys. Lett., 97 (2010) 253308.
[38] J. Lee, S. Hofmann, M. Furno, M. Thomschke, Y.H. Kim, B. Lussem, K. Leo, Systematic investigation of transparent organic light-emitting diodes depending on top metal electrode thickness, Org. Electron., 12 (2011) 1383-1388.
[39] S. Hofmann, M. Thomschke, B. Lussem, K. Leo, Top-emitting organic light-emitting diodes, Opt. Express, 19 (2011) A1250-A1264.
[40] E. Najafabadi, K.A. Knauer, W. Haske, C. Fuentes-Hernandez, B. Kippelen, Highly efficient inverted top-emitting green phosphorescent organic light-emitting diodes on glass and flexible substrates, Appl. Phys. Lett., 101 (2012) 023304-023304.
[41] J. Meyer, A. Kahn, Electronic structure of molybdenum-oxide films and associated charge injection mechanisms in organic devices, J. Photon. Energy, 1 (2011) 011109.
[42] T. Chiba, Y.J. Pu, R. Miyazaki, K. Nakayama, H. Sasabe, J. Kido, Ultra-high efficiency by multiple emission from stacked organic light-emitting devices, Org. Electron., 12 (2011) 710-715.
[43] L.S. Liao, K.P. Klubek, Power efficiency improvement in a tandem organic light-emitting diode, Appl. Phys. Lett., 92 (2008) 223311.
[44] S.E. Jang, J.Y. Lee, Organic interlayer for high power efficiency in organic light-emitting diodes, Synthetic Met., 161 (2011) 40-43.
[45] S.H. Cho, S.W. Pyo, M.C. Suh, Low voltage top-emitting organic light emitting devices by using 1,4,5,8,9,11-hexaazatriphenylene-hexacarbonitrile, Synthetic Met., 162 (2012) 402-405.
[46] L.-B. Lin, R.H. Young, M.G. Mason, S.A. Jenekhe, P.M. Borsenberger, Transient photocurrents across organic--organic interfaces, Appl. Phys. Lett., 72 (1998) 864-866.
[47] Y.-K. Kim, J.W. Kim, Y. Park, Energy level alignment at a charge generation interface between 4,4(')-bis(N-phenyl-1-naphthylamino)biphenyl and 1,4,5,8,9,11-hexaazatriphenylene-hexacarbonitrile, Appl. Phys. Lett., 94 (2009) 063305.
[48] S. Lee, J.-H. Lee, J.-H. Lee, J.-J. Kim, The Mechanism of Charge Generation in Charge-Generation Units Composed of p-Doped Hole-Transporting Layer/HATCN/n-Doped Electron-Transporting Layers, Adv. Funct. Mater., 22 (2012) 855-860.
[49] M. Thomschke, M. Furno, B. Lussem, K. Leo, Highly efficient inverted top-emitting organic electroluminescent devices with doped charge transport layers, Org. Photon. IV2010, pp. 77220R.
[50] T.M. Brown, J.S. Kim, R.H. Friend, F. Cacialli, R. Daik, W.J. Feast, Built-in field electroabsorption spectroscopy of polymer light-emitting diodes incorporating a doped poly(3,4-ethylene dioxythiophene) hole injection layer, Appl. Phys. Lett., 75 (1999) 1679-1681.
[51] A. Schmidt, M.L. Anderson, N.R. Armstrong, Electronic States of Vapor-Deposited Electron and Hole Transport Agents and Luminescent Materials for Light-Emitting-Diodes, J. Appl. Phys., 78 (1995) 5619-5625.
[52] B. Broker, O.T. Hofmann, G.M. Rangger, P. Frank, R.P. Blum, R. Rieger, L. Venema, A. Vollmer, K. Mullen, J.P. Rabe, A. Winkler, P. Rudolf, E. Zojer, N. Koch, Density-Dependent Reorientation and Rehybridization of Chemisorbed Conjugated Molecules for Controlling Interface Electronic Structure, Phys. Rev. Lett., 104 (2010) 246805.
[53] C.C. Liu, S.H. Liu, K.C. Tien, M.H. Hsu, H.W. Chang, C.K. Chang, C.J. Yang, C.C. Wu, Microcavity top-emitting organic light-emitting devices integrated with diffusers for simultaneous enhancement of efficiencies and viewing characteristics, Appl. Phys. Lett., 94 (2009) 103302.

[54] Y. Li, L.-W. Tan, X.-T. Hao, K.S. Ong, F. Zhu, L.-S. Hung, Flexible top-emitting electroluminescent devices on polyethylene terephthalate substrates, Applied Physics Letters, 86 (2005) 153508-153508-153503.

[55] K.H. Kim, N.M. Park, T.Y. Kim, K.S. Cho, J.I. Lee, H.Y. Chu, G.Y. Sung, Fabrication of organic light-emitting diodes using ITO anodes grown on polyethersulfone (PES) substrates by pulse-laser deposition, 2005, pp. 145-148.

[56] H. Zhu, Z. Xiao, D. Liu, Y. Li, N.J. Weadock, Z. Fang, J. Huang, L. Hu, Biodegradable transparent substrates for flexible organic-light-emitting diodes, Energy & Environmental Science, 6 (2013) 2105-2111.

[57] N. Lin, J. Huang, A. Dufresne, Preparation, properties and applications of polysaccharide nanocrystals in advanced functional nanomaterials: a review, Nanoscale, 4 (2012) 3274-3294.

[58] J. Vartiainen, T. Pöhler, K. Sirola, L. Pylkkänen, H. Alenius, J. Hokkinen, U. Tapper, P. Lahtinen, A. Kapanen, K. Putkisto, P. Hiekkataipale, P. Eronen, J. Ruokolainen, A. Laukkanen, Health and environmental safety aspects of friction grinding and spray drying of microfibrillated cellulose, Cellulose, 18 (2011) 775-786.

[59] N. Lavoine, I. Desloges, A. Dufresne, J. Bras, Microfibrillated cellulose – Its barrier properties and applications in cellulosic materials: A review, Carbohydrate Polymers, 90 (2012) 735-764.

[60] Y. Habibi, L.A. Lucia, O.J. Rojas, Cellulose nanocrystals: chemistry, self-assembly, and applications, Chemical reviews, 110 (2010) 3479-3500.

[61] R.J. Moon, A. Martini, J. Nairn, J. Simonsen, J. Youngblood, Cellulose nanomaterials review: structure, properties and nanocomposites, Chemical Society Reviews, 40 (2011) 3941-3994.

[62] L. Hu, G. Zheng, J. Yao, N. Liu, B. Weil, M. Eskilsson, E. Karabulut, Z. Ruan, S. Fan, J.T. Bloking, M.D. McGehee, L. Wagberg, Y. Cui, Transparent and conductive paper from nanocellulose fibers, Energy & Environmental Science, 6 (2013) 513-518.

[63] I. Siró, D. Plackett, Microfibrillated cellulose and new nanocomposite materials: a review, Cellulose, 17 (2010) 459-494.

[64] H. Fukuzumi, T. Saito, T. Iwata, Y. Kumamoto, A. Isogai, Transparent and High Gas Barrier Films of Cellulose Nanofibers Prepared by TEMPO-Mediated Oxidation, Biomacromolecules, 10 (2008) 162-165.

[65] H. Yu, Z. Qin, B. Liang, N. Liu, Z. Zhou, L. Chen, Facile extraction of thermally stable cellulose nanocrystals with a high yield of 93% through hydrochloric acid hydrolysis under hydrothermal conditions, Journal of Materials Chemistry A, 1 (2013) 3938-3944.

[66] Y. Zhou, C. Fuentes-Hernandez, T.M. Khan, J.-C. Liu, J. Hsu, J.W. Shim, A. Dindar, J.P. Youngblood, R.J. Moon, B. Kippelen, Recyclable organic solar cells on cellulose nanocrystal substrates, Scientific reports, 3 (2013).

[67] M. Nogi, S. Iwamoto, A.N. Nakagaito, H. Yano, Optically Transparent Nanofiber Paper, Adv. Mater., 21 (2009) 1595-1598.

[68] J. Kim, S. Yun, Z. Ounaies, Discovery of Cellulose as a Smart Material, Macromolecules, 39 (2006) 4202-4206.

[69] M.T. Postek, A. Vladár, J. Dagata, N. Farkas, B. Ming, R. Wagner, A. Raman, R.J. Moon, R. Sabo, T.H. Wegner, Development of the metrology and imaging of cellulose nanocrystals, Measurement Science and Technology, 22 (2011) 024005.

[70] C. Legnani, C. Vilani, V.L. Calil, H.S. Barud, W.G. Quirino, C.A. Achete, S.J.L. Ribeiro, M. Cremona, Bacterial cellulose membrane as flexible substrate for organic light emitting devices, Thin Solid Films, 517 (2008) 1016-1020.

[71] Y. Okahisa, A. Yoshida, S. Miyaguchi, H. Yano, Optically transparent wood–cellulose nanocomposite as a base substrate for flexible organic light-emitting diode displays, Composites Science and Technology, 69 (2009) 1958-1961.

[72] S. Ummartyotin, J. Juntaro, M. Sain, H. Manuspiya, Development of transparent bacterial cellulose nanocomposite film as substrate for flexible organic light emitting diode (OLED) display, Industrial Crops and Products, 35 (2012) 92-97.

[73] J.S. Kim, P.K.H. Ho, N.C. Greenham, R.H. Friend, Electroluminescence emission pattern of organic light-emitting diodes: Implications for device efficiency calculations, J. Appl. Phys., 88 (2000) 1073-1081.

[74] K.A. Knauer, E. Najafabadi, W. Haske, B. Kippelen, Inverted top-emitting blue electrophosphorescent organic light-emitting diodes with high current efficacy, Applied Physics Letters, 101 (2012) 103304-103304.

[75] S. Beck-Candanedo, M. Roman, D.G. Gray, Effect of Reaction Conditions on the Properties and Behavior of Wood Cellulose Nanocrystal Suspensions, Biomacromolecules, 6 (2005) 1048-1054.

Chapter 5: White Stacked Inverted Top-Emitting OLEDs

In this chapter, the advantages of stacked inverted top-emitting white OLEDs are discussed and a brief historical overview of white OLEDs is given. Next, a stacked inverted top-emitting white OLED device comprising of individual orange and blue subunits is demonstrated for the first time. A discussion for further optimization and characterization of such a white OLED is given, along with some outstanding issues such as lifetime and reproducibility.

5.1 Motivation

White OLEDs are the most sought after OLED type for lighting applications, and also the most difficult to achieve. This is mainly due to the lack of broad spectrum emitters, necessitating systems that use multiple emitters to achieve a broad spectral coverage. Many device architectures can be used for making white OLEDs, the simplest being single stacked bottom emitting white conventional OLEDs. The major advantage of white stacked inverted top-emitting OLEDs is their ease of color mixing and their integrability with flexible substrates.

In terms of color mixing, separate blue and orange OLEDs of appropriate spectral characteristics can be optimized and well matched in terms of their current efficacy, and then combined. White OLEDs that have a single emissive layer with multiple dopants are more difficult to optimize. Controlling the charge balance in one organic host material such that all dopants receive the requisite amount of charge simultaneously is difficult, since the dopants all have different IE/EA values. Isolating each emitter in a unique host and then stacking them with connecting units (CUs) composed of thin organic semiconductors, metals, and/or oxides is a preferred architecture.

In terms of substrates, white inverted top-emitting OLEDs can be fabricated on large-area metal foils such as aluminum, which are more industrially favorable from a manufacturing and

implementation perspective. Additionally, TCOs non-uniformity and defects that hinder large-area white OLED applications are avoided.

5.2 Historical Perspective

5.2.1 Overview

Organic light-emitting diodes (OLEDs) hold the exciting prospect of replacing today's bulkier and less efficient displays and luminaries with efficient, lightweight, and flexible panels that are more environmentally friendly [1]. White OLEDs can be used in conjunction with patterned color filters to produce active-matrix full-color displays [2] as well as for general lighting [3]. In both applications, it is highly desirable that the OLEDs be efficient and have long operational lifetimes. For displays, it is advantageous for the OLEDs to have an architecture convenient for integration with the preferred *n*-type pixel driving electronics used in active-matrix displays [4]. For general lighting, it is especially important that the white OLEDs are suitable for use in large-area applications [5]. As a device architecture, stacked inverted top-emitting white OLEDs with thin metal electrodes are appealing for both of these major application areas.

5.2.2 Stacked OLEDs

The first demonstration of a stacked OLED was in 1997 by Forrest et al. [6]. This device consisted of distinct red, green, and blue light emitting units connected in series through the use of connecting units. However, the units were each independently addressed and biased. This then allowed the display resolution to increase by having all three colors being present in the area of one pixel. They achieved an external quantum efficiency of less than 1% for each of the colors.

121

They additionally noted that microcavity effects distorted the spectra of the individual OLEDs, something which is undesirable from the point of view of display applications. The highest reported current efficacy was by Cho et al. reporting a value of 200 cd/A from a conventional, top-emitting two-unit green electrophosphorescent stacked microcavity OLED. This OLED was optimized for cavity length and made use of an anode of Ag (100 nm) and an optically outcoupled, semitransparent cathode consisting of Al (1 nm)/Ag (20 nm)/4, 4', 4"-tris(N-carbazolyl)-triphenylamine (TCTA) (60 nm) [7].

At the time of writing of this thesis, to the best of our knowledge, no reports for inverted stacked OLEDs have appeared in the literature.

5.2.3 White OLEDs

Kido et al. developed the first white OLED from vacuum thermal evaporated materials. In terms of performance, the devices had a turn on voltage of 10 V and a maximum luminance of 2,000 cd/m^2, with a maximum power efficacy of 1 lm/W with an EQE of 1% and a short lifetime of less than one day [8].

In terms of the highest performance in the literature for phosphorescent OLEDs comprising of different layers, there is a report by Reineke et al. that show white OLEDs with 81 lm/W at 1,000 cd/m^2 by employing a complex three-layer RGB EMLs based on phosphorescent emitters and optical outcoupling with lenses (a 2.7 fold enhancement). Without the optical outcoupling, the devices had a power efficacy of 33 lm/W [9].

Currently white OLEDs for lighting applications are significantly behind their main solid-state LED lighting competition in terms of cost competitiveness, lifetime, and efficiency (see Fig. 5.1). As shown in Fig. 5.2, the luminous efficacy (lm/W) of commercially available

OLEDs is behind LEDs by almost an order of magnitude. However, laboratory-produced OLEDs show significant promise. The target for OLED efficacy by 2020 is nearly 200 lm/W, significantly higher than current fluorescent tube and bulb technology.
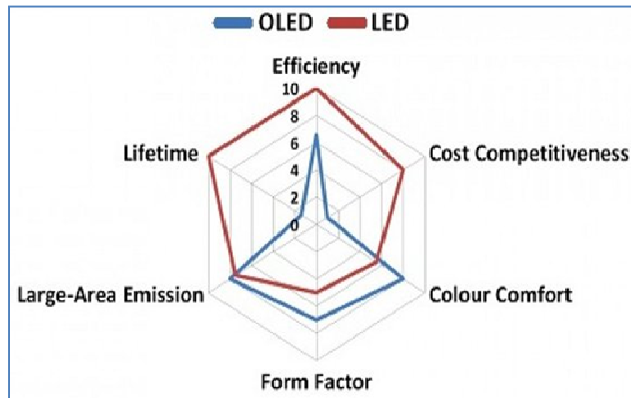
Fig. 5.1. Comparison of OLED and LED technologies for lighting in the year 2013. Taken from [10].
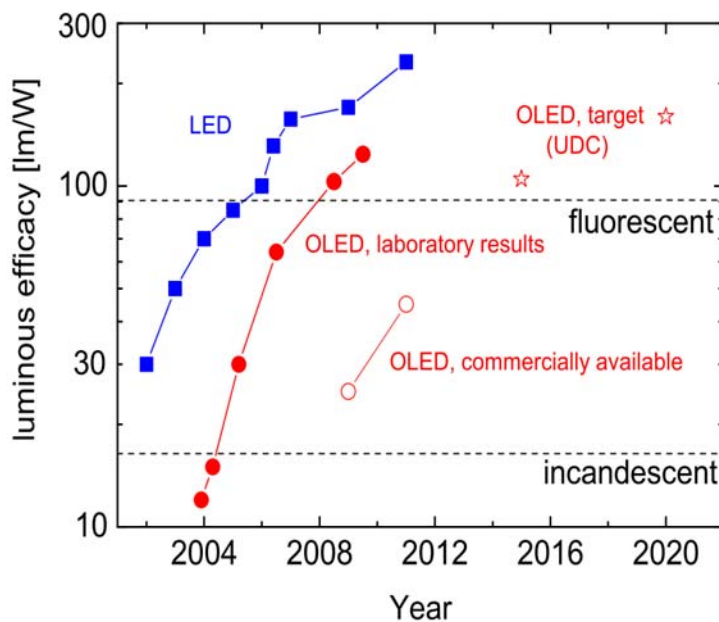
Fig. 5.2. The maximum reported luminous efficacy (lm/W) of LED and OLED technologies by year. Taken from [11].

5.2.4 Inverted White Single-unit OLEDs

In terms of white OLEDs, there are only two reports that attempt to build inverted white OLEDs. The first, from D. Ma's group, is a inverted top-emitting OLED based on a blue emitter p-bis(p-N,N-diphenyl-amino-styryl) (DSA-ph) doped into a 2-methyl-9,10-di(2-naphthyl) anthracene (MADN) host. They achieved efficient blue, green, and white OLEDs by changing the thickness of the HTL, thus modifying the optical properties of the microcavity created by the metal electrodes. The white OLEDs reached a maximum of 5.6 cd/A efficacy [11]. The only other report was from Tomschke et al, where they optimized white OLEDs achieving a power efficacy of 13.3 lm/W, an EQE of 7.8%, and a current efficacy of 26.7 cd/A. They employed an additional optical outcoupling layer with N,N,N',N'tetrakis(4-methoxyphenyl)-benzidine (Me-OTPD) deposited on a Ag top-cathode, and found that the performance values are comparable with corresponding non-inverted bottom emitting OLEDs [12].

In terms of a stacked inverted white OLED, no reports exist in the literature.

5.3 Design Considerations of Stacked OLEDs

5.3.1 General Considerations

From a design standpoint, the stacked white OLED can be broken down to its constituent OLEDs and optimize those components individually. First we elect to develop and optimize blue and orange inverted top-emitting OLEDs with high current efficacy. These two OLEDs are then matched in their current-luminance and current-voltage characteristics. This is so one OLED

does not dominate in the stack, and a more pure white can be produced. Again, in the stacked OLED, the devices will be put under a large voltage that will cause current flow in the subunit OLEDs. Each OLED should have essentially comparable current levels for each applied voltage and produce roughly the same order of magnitude luminance. An easy way to gauge this device compatibility is through current efficacy measurements. OLEDs that have roughly the same current efficacy at the same voltage ranges should be suitable for stacking.

5.3.2 Connecting Unit Considerations

In terms of the critical Connecting Units (CUs), it is still unclear in the literature the mechanism through which CUs operate. Therefore, a lot of trial and error experimentation is required to find the appropriate material combinations and thicknesses. Ideally, it is desirable to have a *p*-type/doped *n* -type organic hetero-junction with thickness values that are significantly smaller than that of neighboring hole and electron-transport layers (which on the order of 30-40 nm). Additionally, if the *n*-type material is doped with metals and inorganic materials such as Al/LiF, then the interlayer should be as transparent as possible. Otherwise light from the bottom unit will be blocked from exiting the top semi-transparent anode.

In terms of previous research, the CUs that have been investigated in the literature can be modified for use in this research. For instance, Chiba et al. previously used a connecting unit of LiF/Al/HAT-CN/TAPC in stacked electrophosphorescent OLEDs [13], where they advocate charge generation at the HAT-CN/TAPC interface. Reported values for the electron affinity of HAT-CN (4.4 eV [13] to 6.0 eV [14]) and the ionization potential of TAPC (5.4 eV [15]) support this claim by leading to efficient electron transfer between the HOMO level of TAPC to the LUMO level of HAT-CN. Others have shown that thin interlayers of Al/LiF are used to

promote electron injection into the top LEU by decreasing the energy barrier between the LUMO

level of TpPyPB (3.04 eV [16]) and the LUMO level of HAT-CN [13, 17]. Once a CU is

identified, a stacked white OLEDs with the device structure: Opaque metal

cathode/EIL/ETL/orange EML/HTL/CU/ETL/blue EML/HTL/HIL/semi-transparent metal anode

can be designed.

5.3.3 Top-Anode Considerations

For a top-emitting OLED, the electrical and optical properties of the anode are critical to

device performance. A semi-transparent Au/MoO$_3$ anode that has been shown to lead to very

efficient OLEDs when used with an HTL of CBP; this high efficiency is believed to partly result

from the Au/MoO$_3$ anode injecting holes directly into the HOMO of the CBP [18]. Further

optical fine-tuning must be considered however, since the emission spectrum is affected by a

microcavity formed between the Al cathode and Au anode, as well as the transmittance of the

anode. The transmittance of MoO$_3$ and Au on glass is shown in Fig. 5.3.
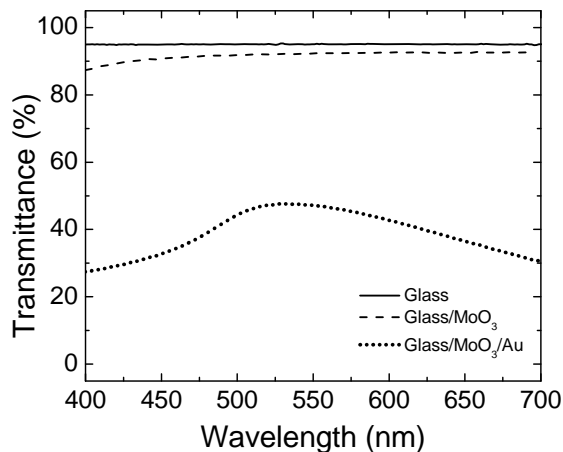
Fig. 5.3. The transmittance of MoO$_3$ (15 nm) and Au (20 nm) on glass.

Across the visible wavelengths the glass substrate has a high transmittance of 95% and a 15 nm MoO$_3$ layer on glass maintains a transmittance of about 90%. When 20 nm of Au is deposited on the MoO$_3$, the transmittance drops below 50% in the blue wavelengths. This data illustrates the fact that higher efficiencies can be expected from OLEDs that optically optimize the anode for blue transmission. To optimize the white inverted-top emitting OLEDs, an organic material of appropriate refractive index and thickness such as α-NPD to extract some of the light from the devices is used.

5.4 Results from Efficient Blue Inverted Top-Emitting OLEDs

Blue inverted top-emitting OLEDs with the device structure Glass/PEDOT:PSS (40 nm)/Al (50 nm)/LiF (2.5 nm)/1,3,5-tri(m-pyrid-3-yl-phenyl)benzene) (TmPyPB) (40 nm)/ N,N'-dicarbazolyl-3,5-benzene (mCP): iridium(III)bi[(4,6-di-fluorophenyl)-pyridinato-N,C2']picolinate (FIrpic) (20 nm)/CBP (35 nm)/MoO$_3$ (15 nm)/Au (20 nm) were demonstrated in Knauer et al [19]. This work is particularly notable since it is difficult to get high efficiency blue emission in OLEDs. It was shown that TpPyPB performed poorly with a blue FIrpic emitter doped in a mCP host. Instead, using a similar compound, TmPyPB [16] as the ETL, a high current efficacy of 33.6 cd/A at 1126 cd/m^2 could be achieved. This OLED can be used in the stacked white OLED with the appropriate engineering of the connecting unit to integrate with the blue ETL and finding an appropriate HTL for charge balance and outcoupling material and thickness for white emission.

5.5 Fabrication of Efficient Orange Inverted Top-Emitting OLEDs

Stacked OLEDs from Chiba et al. [13] showed OLEDs with connecting layers having HAT-CN/TAPC. We therefore investigated OLEDs with a tris[2-phenyl-4-methylquinoline]iridium(III) Ir(Mpqh)$_3$ orange emitter, and we first tried having both a TAPC host and a HTL of TAPC. This would lead us to easily stack the OLED with the appropriate CU. We therefore fabricated red inverted top-emitting OLED having the device structure: Al (50 nm)/LiF (2.5 nm)/TpPyPB (40 nm)/ TAPC:Ir(Mpqh)$_3$ (6% by volume) (20 nm)/ TAPC (35 nm)/MoO$_3$ (15 nm)/Au (20 nm). From a process flow standpoint, an identical recipe was followed as in the case of the blue OLEDs, but with the different material choice for the ETL, EML host, dopant and HTL.

Figure 5.4 shows the device structure along with a plot of the current density versus voltage of the OLEDs. Figure 5.5 shows the luminance versus voltage and current efficacy versus luminance. These red devices have a turn-on voltage of 3.6 V and current efficacies of 12 cd/A at 149 cd/m^2 and 8.9 cd/A at 1,100 cd/m^2.
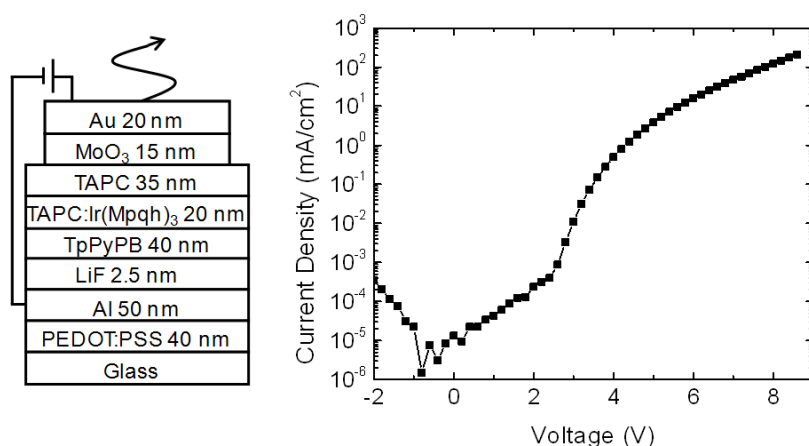
Fig. 5.4. OLED device structure and (b) current density versus voltage curves for red OLEDs with a TAPC host.
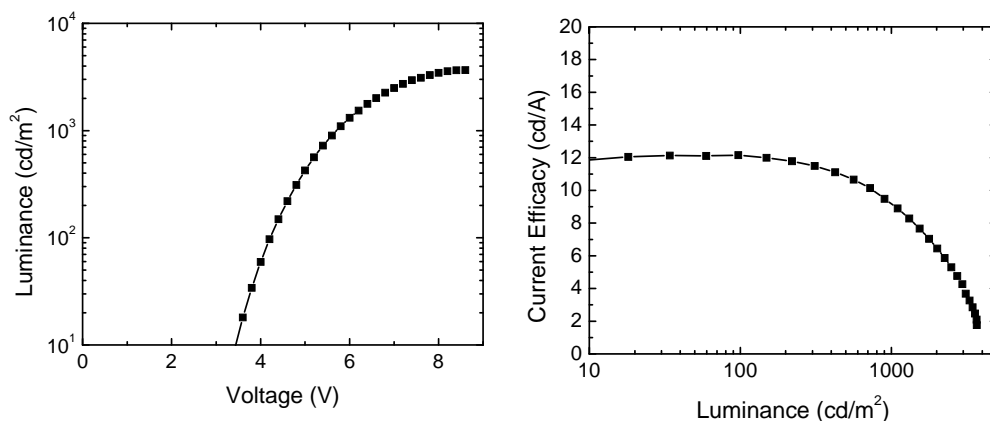
Fig. 5.5. Luminance versus voltage and current efficacy versus luminance of red OLEDs with a TAPC host.

We further optimized this work by reverting to the superior CBP host while maintaining the TAPC as an HTL to more readily integrate with the CUs of a stacked OLED. Devices with the structure Al (50 nm)/LiF (2.5 nm)/TpPyPB (40 nm)/ CBP:Ir(Mpqh)$_3$ (6% by volume) (20 nm)/ TAPC (35 nm)/MoO$_3$ (15 nm)/Au (20 nm) were therefore made.

Figure 5.6 shows the device structure along with a plot of the current density versus voltage of these superior red OLEDs. Figure 5.7 shows the luminance versus voltage and current efficacy versus luminance. These red devices have a turn-on voltage of 3.6 V and current efficacies of 13.7 cd/A at 100 cd/m^2 and 10.6 cd/A at 1,000 cd/m^2.

Au 20 nm
MoO₃ 15 nm
TAPC 35 nm
CBP:Ir(Mpqh)₃ 20 nm
TpPyPB 40 nm
LiF 2.5 nm
Al 50 nm
PEDOT:PSS 40 nm
Glass

10^3
10^2
10^1
10^0
10^{-1}
10^{-2}
10^{-3}
10^{-4}
10^{-5}

Current Density (mA/cm^2)
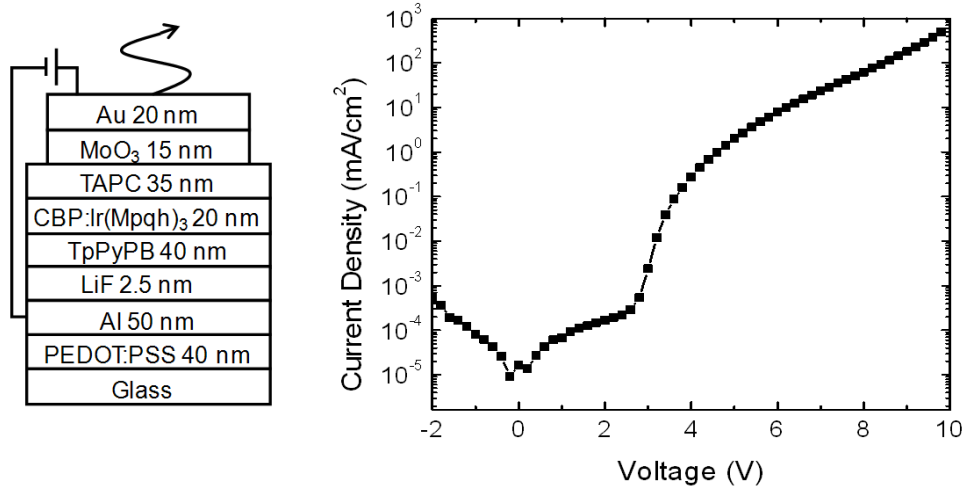
Voltage (V)

Fig. 5.6. OLED device structure and (b) current density versus voltage curves for red OLEDs with a CBP host.

10^4
10^3
10^2
10^1

Luminance (cd/m^2)

Voltage (V)

25
20
15
10
5
0

Current Efficacy (cd/A)
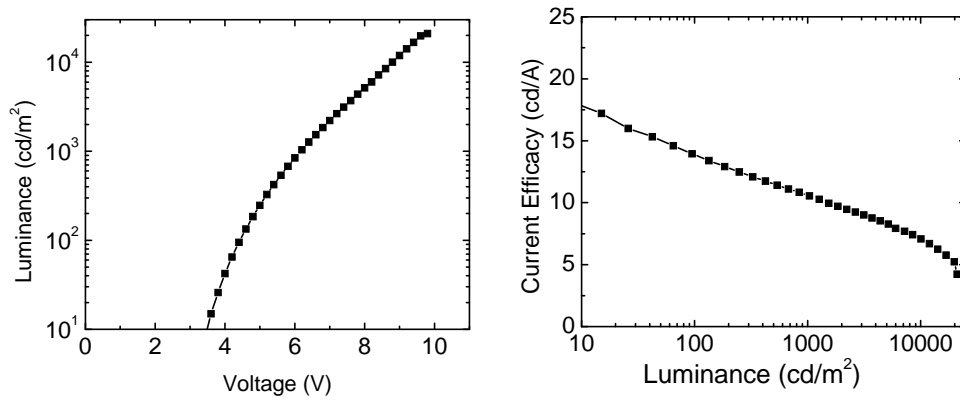
Luminance (cd/m^2)

Fig. 5.7. Luminance versus voltage and current efficacy versus luminance of red OLEDs with a CBP host.

5.6 Stacked Inverted Top-Emitting White OLEDs

As mentioned is section 5.2.4, few reports exist on inverted top-emitting white OLEDs, none of which have a stacked architecture. Wang et *al.* [11] used OLEDs containing a blue emitter p-bis(p-N,N-diphenyl-amino-styryl) (DSA-ph) to produce blue, green, and white OLEDs by changing the thickness of the microcavity formed by the device's metal electrodes. These white OLEDs reached a maximum of 5.6 cd/A efficacy [11]. Tomschke *et al.* also reported on inverted top-emitting white OLEDs that achieved a power efficacy of 13.3 lm/W, an EQE of

7.8%, and a current efficacy of 26.7 cd/A [12]. Neither report mentions the luminance level at which these metrics were determined.

Here, we report on stacked inverted top-emitting white OLEDs that combine the advantages of inverted top-emitting OLEDs and stacked OLEDs. The white OLED has a double-unit stack consisting of an orange and a blue LEU. These devices attain a current efficacy of 26.5 cd/A at a luminance of 100 cd/m^2. For purposes of comparison, single-unit inverted top-emitting OLEDs based on the orange and blue LEUs are also fabricated and characterized. The current efficacy values of the orange and blue OLEDs are 21.2 cd/A and 32.6 cd/A, respectively, at a luminance of 100 cd/m^2.

5.6.1 Experimental Methods

OLED substrates were cut into 1 × 1 inch squares from 1.0 mm-thick glass micro-slides (VWR International) and cleaned by ultrasonication (5510, Branson Ultrasonics) for 20 min in baths of water with detergent, distilled water, acetone, and isopropanol. The substrates were then blown dry with nitrogen gas and treated by oxygen plasma for 2 min (Plasma-Preen II, Plasmatic Systems, Inc.). To improve the wettability of the bottom aluminum cathode, poly(3,4-ethylenedioxythiophene) poly(styrenesulfonate) (PEDOT:PSS, Clevios P VP AI 4083) was dispensed onto the substrates through a 0.45 μm polyvinylidene fluoride filter and spin coated (WS-400B-6NPP/LITE, Laurell Technologies, Inc.) at a speed of 5,000 rpm for 1 min [20]. They were then placed on a hot plate for 10 min at 140 °C. The PEDOT:PSS layer was 40 nm-thick and characterized by spectroscopic ellipsometry (M-2000UI, J.A. Woollam Co., Inc.).

The samples were then loaded into a thermal vacuum evaporation system (EvoVac, Angstrom Engineering Inc.) evacuated to a pressure below 3×10^{-7} Torr. First, the bottom Al cathode was deposited to a thickness of 50 nm at a rate of 2 Å/s. A 2.5 nm-thick lithium fluoride

(LiF) layer was then deposited at a rate of 0.2 Å/s as an electron injection layer (EIL). The bottom orange LEU was made of an ETL of 1,3,5-tri(p-pyrid-3-yl-phenyl)benzene (TpPyPB) with a thickness of 40 nm, a 20 nm-thick emissive layer of 4,4′-bis(N-carbazolyl)-1,1′-biphenyl (CBP) coevaporated with 6% by volume of tris[2-phenyl-4-methylquinoline)]iridium(III)(Ir(Mphq)$_3$) and a 35 nm-thick hole-transport layer of 1,1-bis-(4-bis(4-tolyl)-aminophenyl)cyclohexene (TAPC). For the stacked white OLEDs, the bottom orange LEU was connected to a blue top LEU by a CU consisting of 10 nm of 1,4,5,8,9,11-hexaazatriphenylene hexacarbonitrile (HAT-CN), a 2.5 nm-thick Al layer, and a 1.0 nm-thick LiF layer. For these interlayers, the HAT-CN was deposited at a rate of 0.2 Å/s, the Al at 1 Å/s, and the LiF at a rate of 0.1 Å/s. The top blue LEU consisted of a 40 nm-thick electron-transport layer of 1,3,5-tri(p-pyrid-3-yl-phenyl)benzene (TmPyPB), an emissive layer with a total thickness of 20 nm consisting of 4,4′-bis(N-carbazolyl)-1,1′-biphenyl (mCP) coevaporated with 12% by volume of tris[2-phenyl-4-methylquinoline)]iridium(III) (FIrpic), and a 35 nm-thick hole-transport layer of CBP. All organic compounds besides HAT-CN were deposited at a rate of 1.0 Å/s. The top anode consists of a 15 nm-thick hole-injection layer of molybdenum trioxide (MoO$_3$) that was deposited at a rate of 0.2 Å/s and a semitransparent 20 nm-thick top Au anode that was deposited at a rate of 2 Å/s. Tooling factors were calibrated using spectroscopic ellipsometry and the thicknesses of all layers were estimated by the quartz crystal monitors in the deposition chamber. In the same batch as the stacked white OLEDs, single-unit orange and blue OLEDs based on the white OLED's LEUs were also made for comparison. The typical OLED active area was 4.2×3.6 mm^2. TpPyPB, TmPyPB, TAPC, mCP, Ir(ppy)$_3$, FIrpic, and HAT-CN were purchased from Luminescence Technology Corporation and all other materials were

purchased from Sigma-Aldrich. All organic materials were purified by gradient-zone sublimation.

The devices (8 blue, 13 orange, and 7 white OLEDs) were then characterized with a source meter (Keithley 2400) and a calibrated photodiode (FDS 100 from Thorlabs, Inc.) in order to take current versus voltage and luminance versus voltage measurements. For angular-dependent electroluminescent spectra, the substrates were first mounted on a rotating stage and then measured with a radiometrically calibrated spectrometer (Ocean Optics USB4000).

5.6.2 Results and Discussion
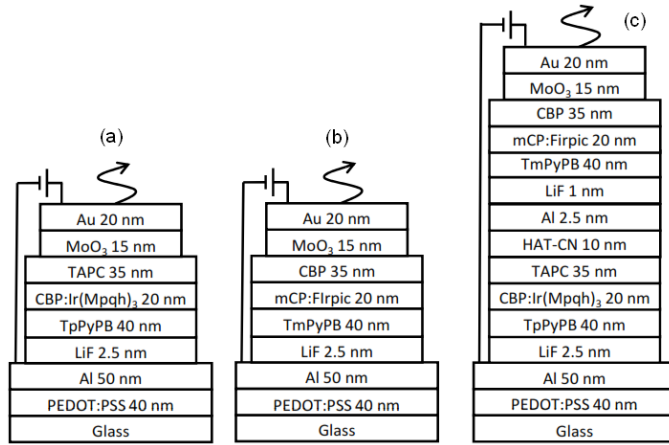
Fig. 5.8. Device structures of the (a) orange, (b) blue, and (c) white OLEDs.

The device structure of the orange, blue, white OLEDs are shown in Fig. 5.8(a), 5.8(b), and 5.8(c), respectively. Plots of the current density versus voltage and luminance versus voltage of the OLEDs are shown in Fig. 5.9 and Fig. 5.10, respectively. The turn-on voltages (defined here as the voltage at which a luminance of 10 cd/m^2 is achieved) for the orange and blue OLEDs are 3.5 and 3.4 V, respectively. The turn-on voltage for the white OLED is 7.1 V. Note that the white OLED's turn-on voltage is close to the sum of the turn-on voltages of the single-unit OLEDs. This data indicates that the white OLED, consisting of a bottom orange LEU, a CU, and a top blue LEU, is operating similarly to an orange OLED and blue OLED electrically connected in series. Thus, the CU of HAT-CN/Al/LiF allows for a very effective interconnection between the LEUs of the stacked OLED. The CU's effectiveness depends on the choice of the materials neighboring it, namely the heterojunction of TAPC/HAT-CN with the bottom LEU and the material combination of Al/LiF/TmPyPB with the top LEU. Chiba et al. have previously shown the effectiveness of using a CU of LiF/Al/HAT-CN in highly efficient stacked green OLEDs in the conventional geometry [13]. There the authors claim that the HAT-

CN/TAPC heterojunction is the interface responsible for charge generation in which electrons transfer between the highest occupied molecular orbital (HOMO) level of TAPC to the lowest unoccupied molecular orbital (LUMO) level of HAT-CN. Reported values for the electron affinity (EA) of HAT-CN range from 4.4 eV [13] to 6.0 eV [14] and the reported value of the ionization potential of TAPC is 5.4 eV [15]. Recently, we have shown that an inverted deposition sequence of Al followed by LiF can result in efficient electron injection into both TpPyPB (EA = 3.04 eV [16]) and TmPyPb (EA = 2.73 eV [16]), which here have been used in conjunction with Al/LiF in the bottom and top LEUs, respectively [19].
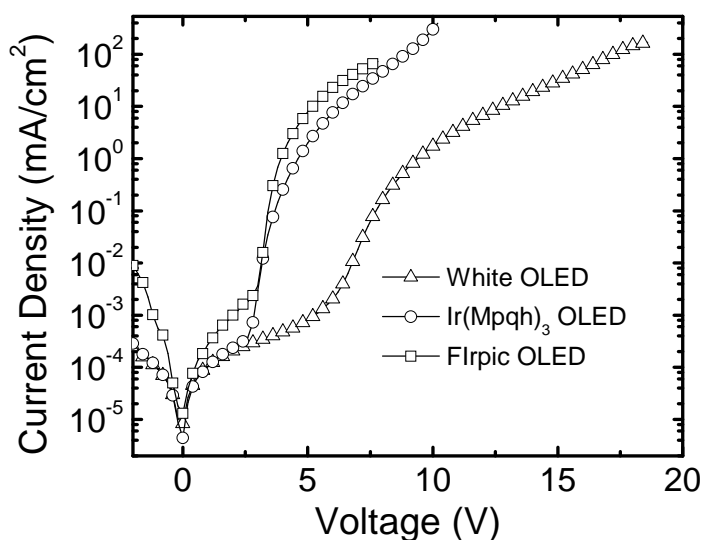
Fig. 5.9. Current-density versus voltage of orange, blue, and white OLED.
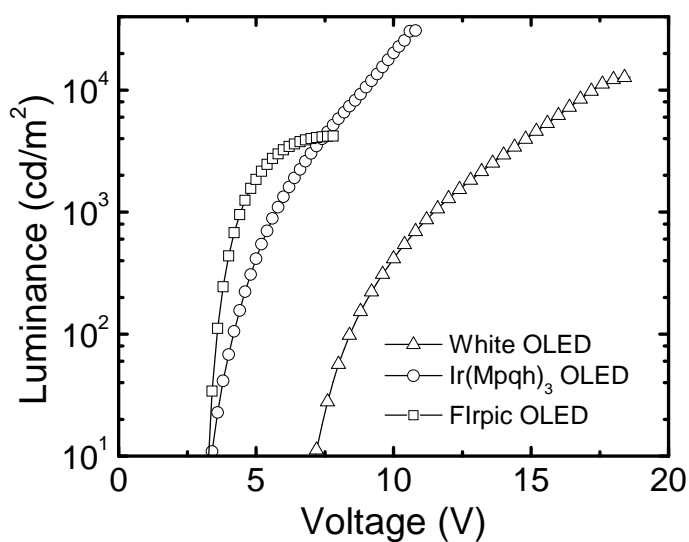
Fig. 5.10. Luminance versus voltage of orange, blue, and white OLEDs.

The current efficacy versus voltage of the OLEDs is shown in Fig. 5.11. The device performance is summarized in Table 5.1. Across most luminance values, the white OLED has a current efficacy intermediate to that of the blue and red OLEDs, attaining a maximum (non-averaged) current efficacy of 36.4 cd/A at a luminance of 11.2 cd/m^2. It reached a maximum luminance (non-averaged) of about 12,756 cd/m^2 with a current efficacy of 7.6 cd/A.
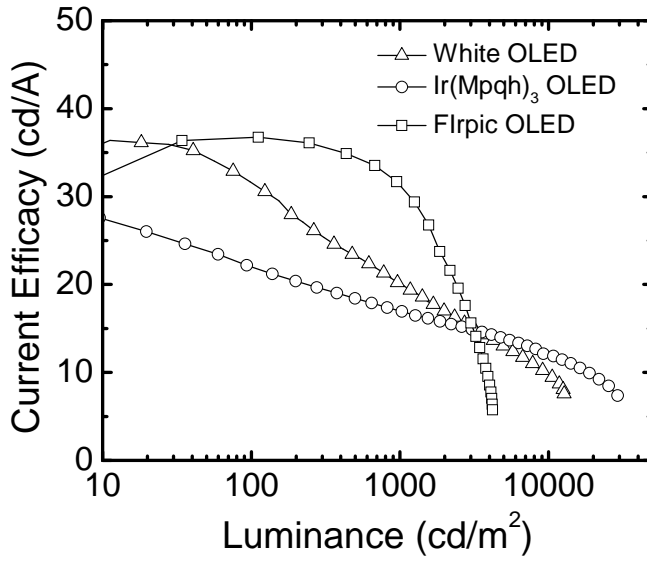
Fig. 5.11. Current efficacy versus luminance of orange, blue and white OLEDs.

Table 5.1. Average performance and standard deviation for all OLEDs, characterizing 13 orange, 8 blue, and 7 white OLEDs.

	Luminance [cd/m^2]	Voltage [V]	Current Density [mA/cm^2]	Current Efficacy [cd/A]
Orange	10	3.5 (±0.1)	0.06 (±0.02)	26.0 (±2.9)
	100	4.3 (±0.1)	0.56 (±0.09)	21.2 (±0.8)
	1000	5.9 (±0.1)	6.73 (±0.47)	16.3 (±0.7)
	10000	8.9 (±0.2)	88.1 (±5.0)	11.8 (±0.4)
Blue	10	3.4 (± 0)	0.11 (±0.01)	34.4 (±3.2)
	100	3.6 (± 0.0)	0.46 (±0.36)	32.6 (±9.4)
	1000	4.5 (±0.1)	4.61 (±1.12)	28.4 (±4.2)
	5000	5.6 (±0.0)	32.4 (±4.60)	16.5 (±2.5)
White	10	7.1 (±0.1)	0.04 (±0.01)	29.5 (±6.0)
	100	8.4 (±0.1)	0.43 (±0.10)	26.5 (±4.3)
	1000	11.5 (±0.2)	5.70 (±0.44)	18.5 (±1.3)
	10000	17.0 (±0.3)	112.0 (±7.7)	9.3 (±0.7)

The spectra of the orange, blue, and white OLEDs are displayed in Fig. 5.12(a). The measurements are normalized to the maximum intensity of each OLED's individual spectrum collected at normal incidence. The white OLED spectrum is clearly composed of emission due to

both FIrpic and Ir(Mpqh)$_3$. By comparing the blue portion of the white OLED's spectrum with the blue OLED, it is apparent that the relative intensities of the FIrpic peaks have changed. Also in the white OLED spectrum, the peak due to Ir(Mpqh)$_3$ emission has shifted from 631.6 nm to 577.3 nm and significant spectral narrowing has occurred when compared to the spectrum of the orange OLED. To explain these effects, it is important to realize that in these top-emitting OLEDs the cathode and semitransparent anode act as parallel mirrors and form a microcavity. It is well known that microcavity OLEDs act as Fabry-Pérot resonators giving rise to various microcavity effects such as spectral narrowing, angular-dependent spectra, and forward-angle emission enhancement [21]. In comparing the microcavity of the white OLED with that of the single-unit OLEDs, changes have been made to both the cavity thickness and the location of the emissive regions within the device relative to the device's electrodes. Changing either of these parameters will lead to alterations of the complex interference effects taking place within the microcavity, likely leading to the observed deviation from the white OLED spectrum being a simple combination of the spectra of orange and blue single-unit OLEDs [21].

The change in the Commission Internationale de l'Eclairage (CIE) coordinates (x,y) of the white OLED as a function of operating voltage and viewing-angle at 10 degree increments is shown in Fig. 5.12(b). The color change as a function of voltage is likely due to the different luminance versus current-density characteristics of the two constituent LEUs as is expected from the single-unit OLED data (see supplementary material at [URL] for luminance versus current-density graph in Fig. 5.13). This unwanted effect might be reduced by using LEUs that are more closely matched in their luminance vs. current-density characteristics. The color change versus angle-of-view is an effect of the microcavity. The CIE coordinates (x, y) of the white OLEDs are (0.33,0.47) at 0 degrees and shift to (0.35,0.31) at 80 degrees. Such changes in color upon angle-

of-view are obviously undesirable; however, light-scattering layers can be used on top-emitting OLEDs to reduce the color change with changing angle-of-view while retaining efficiency [21, 22]. See supplementary material at [URL] for photographs of a representative orange, blue, and white OLED on glass substrates in Fig. 5.14.

(a)   (b)
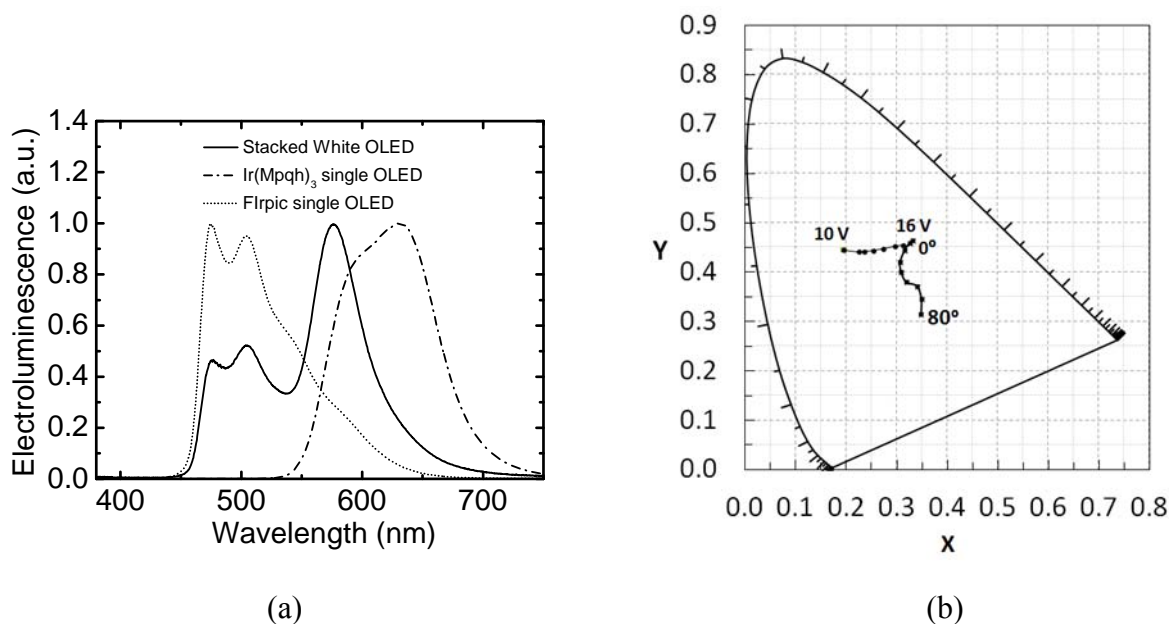
Fig. 5.12. (a) Electroluminescent spectra of orange, blue, and white OLEDs normalized to the maximum intensity of each spectrum. (b) CIE coordinates (x,y) as a function of viewing angle and operating voltage.
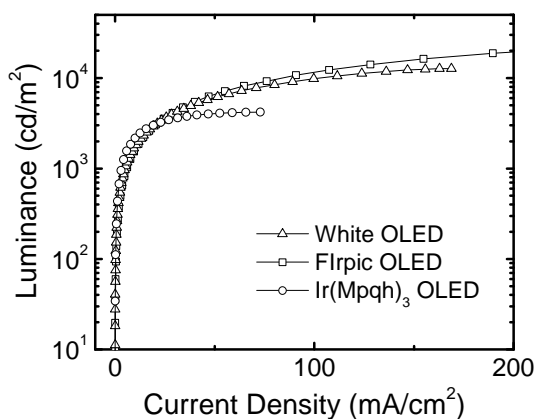
Fig. 5.13. Luminance versus current density of the orange, blue and white OLEDs.
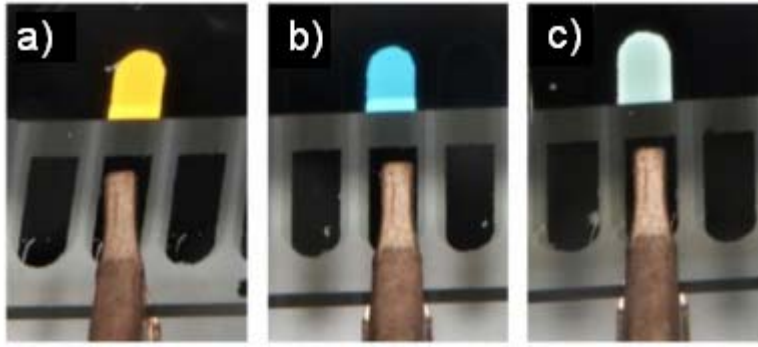
Fig. 5.14. Pictures of (a) orange, (b) blue, and (c) white OLED on glass substrates.

The color-rendering index (CRI) of the white OLEDs at 16 V and normal incidence is 52.9, which is less than the minimum CRI value of 75 that is required for lighting applications [21]. This is not surprising, as the CRI values of top-emitting OLEDs are typically quite low due to spectral narrowing effects [21]. It is important to note, that a CRI value of 62 has been previously reported for a bottom-emitting two-color mixed white OLED using a similar emitter combination [23]. The CRI value of the stacked white OLED can be increased either by further optimization of the microcavity or by implementing a three-layer stack containing red, green, and blue LEUs to broaden the spectrum [3]. Such a stack could be fabricated in a straight-forward manner using the same stacking methodology described here.

Lastly, we must mention that in conventional bottom-emitting OLEDs, EQE and power efficacy (in lm/W) values are typically calculated from a single measurement of the luminance at the surface normal with the assumption that the device is a Lambertian emitter. However, microcavity devices such as those here are not Lambertian emitters [21, 24]. For more detailed characterization, measurements of EQE and power efficacy must be taken with an integrating sphere which captures all of the OLED's emitted light.

5.6.3 Conclusion

In summary, stacked white inverted top-emitting OLEDs consisting of orange and blue LEUs have been demonstrated on glass substrates. This is the first demonstration of white OLEDs with this architecture, combining the respective advantages of having inverted electrode positions, top-emission, and OLED stacking. Also, having thin metal layers as electrodes rather than a brittle TCO electrode allows this device to be fabricated on flexible substrates [25] to take advantage of roll-to-roll manufacturing techniques. A maximum current efficacy of 26.5 cd/A is attained at a luminance of 100 cd/m^2. For comparison, single-unit blue and orange OLEDs were also fabricated that were based on the LEUs contained in the stacked white OLED. The current efficacies of the orange and blue OLEDs are 21.2 cd/A and 32.6 cd/A, respectively, at a luminance of 100 cd/m^2. For practical applications, further optimization to this white OLED is still required both to increase the CRI value and reduce undesired changes in spectrum versus angle-of-view. Two recommended methods include forming a stack with three units in an RGB configuration and adding a diffuser layer upon the semitransparent anode.

5.7 References

[1] R. Coehoorn, V. Elsbergen, C. Verschuren, High Efficiency OLEDs for Lighting Applications, in: E. Cantatore (Ed.) Applications of Organic and Printed Electronics, Springer US 2013, pp. 83-100.
[2] A.D. Arnold, P.E. Castro, T.K. Hatwar, M.V. Hettel, P.J. Kane, J.E. Ludwicki, M.E. Miller, M.J. Murdoch, J.P. Spindler, S.A. Van Slyke, K. Mameno, R. Nishikawa, T. Omura, S. Matsumoto, Full-color AMOLED with RGBW pixel pattern, Journal of the Society for Information Display, 13 (2005) 525-535.
[3] H. Sasabe, J. Kido, Development of high performance OLEDs for general lighting, Journal of Materials Chemistry C, 1 (2013) 1699-1707.
[4] W. Chung-Chih, C.-W. Chen, C.-L. Lin, Y. Chih-Jen, Advanced organic light-emitting devices for enhancing display performances, Display Technology, Journal of, 1 (2005) 248-266.
[5] J.W. Park, D.C. Shin, S.H. Park, Large-area OLED lightings and their applications, Semiconductor Science and Technology, 26 (2011) 034002.

[6] S.R. Forrest, P.E. Burrows, Z. Shen, G. Gu, V. Bulovic, M.E. Thompson, The stacked OLED (SOLED): a new type of organic device for achieving high-resolution full-color displays, Synthetic Metals, 91 (1997) 9-13.

[7] T.-Y. Cho, C.-L. Lin, C.-C. Wu, Microcavity two-unit tandem organic light-emitting devices having a high efficiency, Applied Physics Letters, 88 (2006) 111106-111103.

[8] J. Kido, M. Kimura, K. Nagai, Multilayer White Light-Emitting Organic Electroluminescent Device, Science, 267 (1995) 1332-1334.

[9] S. Reineke, F. Lindner, G. Schwartz, N. Seidler, K. Walzer, B. Lüssem, K. Leo, White organic light-emitting diodes with fluorescent tube efficiency, Nature, 459 (2009) 234-238.

[10] DisplaySearch: small/medium OLED penetration to more than double by 2015. OLED News and Information, Website, http://www.oled-info.com/displaysearch-smallmedium-oled-penetration-more-double-2015.

[11] Q. Wang, Z.Q. Deng, J.S. Chen, D.G. Ma, Realization of blue, green, and white inverted microcavity top-emitting organic light-emitting devices based on the same emitting layer, Optics Letters, 35 (2010) 462-464.

[12] M. Thomschke, R. Nitsche, M. Furno, K. Leo, Optimized efficiency and angular emission characteristics of white top-emitting organic electroluminescent diodes, Applied Physics Letters, 94 (2009) 083303.

[13] T. Chiba, Y.J. Pu, R. Miyazaki, K. Nakayama, H. Sasabe, J. Kido, Ultra-high efficiency by multiple emission from stacked organic light-emitting devices, Org. Electron., 12 (2011) 710-715.

[14] Y.-K. Kim, J.W. Kim, Y. Park, Energy level alignment at a charge generation interface between 4,4'-bis(N-phenyl-1-naphthylamino)biphenyl and 1,4,5,8,9,11-hexaazatriphenylene-hexacarbonitrile, Appl. Phys. Lett., 94 (2009) 063305.

[15] L.B. Lin, R.H. Young, M.G. Mason, S.A. Jenekhe, P.M. Borsenberger, Transient photocurrents across organic-organic interfaces, Appl. Phys. Lett., 72 (1998) 864-866.

[16] S.J. Su, T. Chiba, T. Takeda, J. Kido, Pyridine-containing triphenylbenzene derivatives with high electron mobility for highly efficient phosphorescent OLEDs, Adv. Mater., 20 (2008) 2125-2130.

[17] C.C. Chang, S.W. Hwang, C.H. Chen, J.F. Chen, High-efficiency organic electroluminescent device with multiple emitting units, Jpn. J. Appl. Phys. 1, 43 (2004) 6418-6422.

[18] M.G. Helander, Z.B. Wang, J. Qiu, M.T. Greiner, D.P. Puzzo, Z.W. Liu, Z.H. Lu, Chlorinated Indium Tin Oxide Electrodes with High Work Function for Organic Device Compatibility, Sci., 332 (2011) 944-947.

[19] K.A. Knauer, E. Najafabadi, W. Haske, B. Kippelen, Inverted top-emitting blue electrophosphorescent organic light-emitting diodes with high current efficacy, Appl. Phys. Lett., 101 (2012) 103304.

[20] R. Steyrleuthner, S. Bange, D. Neher, Reliable electron-only devices and electron transport in n-type polymers, J. Appl. Phys., 105 (2009) 064509.

[21] S. Hofmann, M. Thomschke, B. Lussem, K. Leo, Top-emitting organic light-emitting diodes, Opt. Express, 19 (2011) A1250-A1264.

[22] C.-C. Liu, S.-H. Liu, K.-C. Tien, M.-H. Hsu, H.-W. Chang, C.-K. Chang, C.-J. Yang, C.-C. Wu, Microcavity top-emitting organic light-emitting devices integrated with diffusers for simultaneous enhancement of efficiencies and viewing characteristics, Applied Physics Letters, 94 (2009) 103302-103303.

[23] J.S. Park, J.H. Yu, W.S. Jeon, Y.H. Son, C. Kulshreshtha, J.H. Kwon, Two-color-mixed white organic light-emitting diodes with a high color temperature, Journal of Information Display, 12 (2011) 51-55.

[24] J. Lee, S. Hofmann, M. Furno, M. Thomschke, Y.H. Kim, B. Lussem, K. Leo, Systematic investigation of transparent organic light-emitting diodes depending on top metal electrode thickness, Org. Electron., 12 (2011) 1383-1388.

[25] E. Najafabadi, K.A. Knauer, W. Haske, C. Fuentes-Hernandez, B. Kippelen, Highly efficient inverted top-emitting green phosphorescent organic light-emitting diodes on glass and flexible substrates, Appl. Phys. Lett., 101 (2012) 023304.

Chapter 6: Conclusions

In this section, a summary of the research results is presented and a review of the significance of the research is presented. Finally some directions for future research is given along with some preliminary results of experiments conducted in this regard.

6.1 Summary of Research Findings

In summary, the research presented in this thesis has focused on inverted top-emitting electrophosphorescent OLEDs and particularly white OLEDs with this architecture for lighting applications. Whereas chapter 4 chapter was concerned with the fabrication of efficient single unit inverted top-emitting OLEDs with a novel bottom cathode for use with green emitters on a variety of substrates, chapter 5 was concerned with stacking OLEDs in the inverted top-emitting architecture for the fabrication of white OLEDs.

In chapter 4, it was shown that green phosphorescent inverted top-emitting organic light-emitting diodes with high current efficacy and luminance can be made on glass and polyethersulfone (PES) substrates coated with polyethylene dioxythiophene-polystyrene sulfonate (PEDOT:PSS). The bottom cathode consisted of an aluminum/lithium fluoride (Al/LiF) bilayer that injects electrons efficiently into an electron transport layer of 1,3,5-tri(m-pyrid-3-yl-phenyl)benzene (TpPyPB). A high current efficacy of 96.3 cd/A was achieved at a luminance of 1387 cd/m^2 when an optical outcoupling layer of N,N'-Di-[(1-naphthyl)-N,N'-diphenyl]-(1,10-biphenyl)-4,4'-diamine (α-NPD) was deposited on the anode.

In addition, it was shown that the cathode was highly sensitive to the exposure of the trace amounts of O$_2$ and H$_2$O native to the glovebox environment. This was done by comparing the effectiveness of injecting electrons from bottom and top Al/LiF cathode in symmetric electron-dominated devices. The device structure consisted of Glass/PEDOT:PSS (40 nm)/Al (50

nm)/LiF (2.5 nm)/TpPyPB (95 nm)/LiF (2.5 nm)/Al (50 nm). The results showed a comparable current density when electrons are injected from the top electrode as the current density when electrons were injected from the bottom cathode. However identical electron-dominated devices where some have been subjected to a vacuum break and subsequently exposed to the glovebox N_2 atmosphere (O_2 <0.1 ppm, H_2O < 3.0 ppm) after the bottom Al/LiF cathode deposition showed asymmetric current density versus voltage characteristics. The current density of the exposed devices decreased by nearly four orders of magnitude when electrons were injected from the bottom. It is speculated that the high sensitivity of the Al/LiF cathode to trace amounts of O_2 and H_2O may also explain why such cathodes have not been widely implemented in inverted OLED structures until our work.

In chapter 4 section 4.3, a green electrophosphorescent inverted top-emitting organic light-emitting diodes with a Ag/1,4,5,8,9,11-hexaazatriphenylene hexacarbonitrile (HAT-CN) anode has been shown. The use of Ag is more economical than Au and HAT-CN offers the additional benefit of being deposited at a lower temperature (below 350 °C under high vacuum) compared to metal oxides such as MoO_3. A high current efficacy of 124.7 cd/A was achieved at a luminance of 100 cd/m^2 when an optical outcoupling layer of α-NPD was deposited on the anode. The devices had a low turn-on voltage of 3.0 V and exhibited low current efficacy roll-off through luminance values up to 10,000 cd/m^2. Hole-dominated devices with Ag/HAT-CN electrodes showed current densities up to three orders of magnitude higher than devices without HAT-CN.

Also in chapter 4, organic light-emitting diodes (OLEDs) fabricated on recyclable and biodegradable substrates were fabricated, representing a step towards the realization of a sustainable OLED technology. OLEDs have been traditionally made on rigid glass substrates.

145

Flexible OLEDs have also been fabricated on polyethylene terephthalate (PET) and polyethersulfone (PES). However these plastic substrates are petroleum-based and expensive. Additionally, they are not as environmentally friendly as recyclable or biodegradable substrates, because plastic is not as susceptible to biodegradation as natural materials. We demonstrated efficient OLEDs with the inverted top-emitting architecture on recyclable cellulose nanocrystal (CNC) substrates. The OLEDs again had a bottom cathode of Al/LiF, but this electrode was deposited on a 400 nm thick α-NPD layer and a top anode of Au/MoO$_3$. They achieved a maximum luminance of 74,591 cd/m^2 with a current efficacy of 53.7 cd/A at a luminance of 100 cd/m^2 and 41.7 cd/A at 1000 cd/m^2. The average current efficacy of OLEDs on CNCs was 32.5 ± 14.1 cd/A at 10 cd/m^2 and 42.7 ± 9.8 cd/A at 100 cd/m^2. This was similar to the average performance achieved on glass substrates, which was 38.0 ± 19.3 cd/A at a luminance of 10 cd/m2 and 45.5 ± 10.0 at 100 cd/m^2, for 8 devices made in the same batch as the OLEDs on CNC substrates. It was shown that the 400 nm-thick α-NPD layer on the CNC substrate is necessary for achieving high performance OLEDs.

In chapter 5, stacked inverted top-emitting white electrophosphorescent organic light-emitting diodes (OLEDs) were demonstrated. For general lighting, it is especially important that the white OLEDs are suitable for use in large-area applications. As a device architecture, stacked inverted top-emitting white OLEDs with thin metal electrodes are appealing for both display and lighting applications. The OLEDs consisted of orange and blue light-emitting units interconnected with a connecting unit of HAT-CN/Al/LiF. These OLEDs combined the features of having inverted electrode positions, top-emission, and a stacked architecture. They exhibited an average current efficacy of 26.5 cd/A at a luminance of 100 cd/m^2. Single-unit inverted top-emitting OLEDs based on the constituent orange and blue light-emitting units were also

characterized for comparison. The current efficacies of the orange and blue OLEDs were

21.2 cd/A and 32.6 cd/A, respectively, at a luminance of 100 cd/m^2. The color-rendering index

(CRI) of the white OLEDs at 16 V and normal incidence was 52.9, which is less than the

minimum CRI value of 75 that is required for lighting applications. This is not surprising, as the

CRI values of top-emitting OLEDs are typically quite low due to spectral narrowing effects. The

CRI value of the stacked white OLED can be increased either by further optimization of the

microcavity or by implementing a three-layer stack containing red, green, and blue LEUs to

broaden the spectrum.

6.2 Outlook for Future Research

There are several natural extensions to the research shown in this thesis. For instance, the

stacked inverted top-emitting OLEDs demonstrated in chapter 5 are far from optimized. Further

research should be aimed at improving the charge balance in these devices so more of the light

from the constituent orange light-emitting unit can be extracted from the device. This may

involve a better use of transport materials or better design of the intervening connecting unit

layers. For instance, perhaps the thicknesses of these connecting unit layers have to be changed.

An additional optical outcoupling layer with optimized thickness could further extract light from

the stacked OLEDs, yielding higher current efficacies. For practical applications, further research

on these white OLEDs should also seek to improve the CRI value and reduce undesired changes

in spectrum versus angle-of-view by using light-scattering layers.

Another mechanism for improving the current efficacy and lifetimes of the OLEDs

shown in this research is to further stack them with more devices. A preliminary attempt at a

triple stacked OLED with the device structure shown in Fig. 6.1 was undertaken. The resulting

current density vs. voltage and luminance-voltage-current efficacy characteristics are shown in Fig. 6.2.

Au 20 nm
MoO₃ 15 nm

TAPC 35 nm
CBP:Ir(ppy)₃ 20 nm
TpPyPB 40 nm
LiF 1 nm
Al 2.5 nm
HAT-CN 10 nm
TAPC 35 nm
CBP:Ir(ppy)₃ 20 nm
TpPyPB 40 nm
LiF 1 nm
Al 2.5 nm
HAT-CN 10 nm
TAPC 35 nm
CBP:Ir(ppy)₃ 20 nm
TpPyPB 40 nm
LiF 2.5 nm

Al 50 nm
PEDOT:PSS 40 nm
Glass
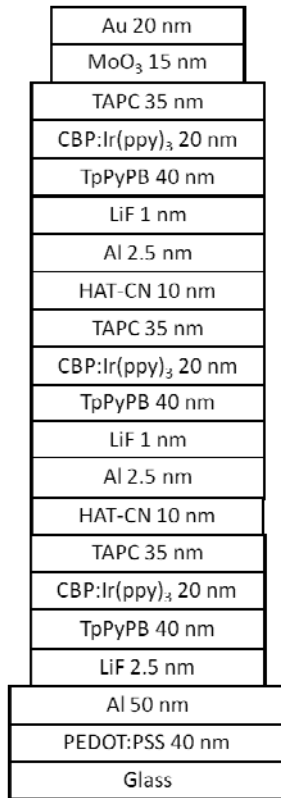
Fig. 6.1. Device architecture for triple stacked inverted top-emitting green OLEDs using Al/LiF cathode.

There it is readily seen that these devices did not perform as expected, perhaps due to imperfect fabrication methods or a deeper underlying physical reason. Certainly these devices are challenging to fabricate, and a better understanding of the issues in triple stacking inverted top-emitting OLEDs would be in of itself an interesting research topic. If this triple stacked device is then optimized and working properly, one could more to a device architecture with separate red, green, and blue light emitting units to create a white OLED with enhanced CRI and current efficacy, which would be of great practical significance for all the reasons discussed in chapter 5.

a)

b)
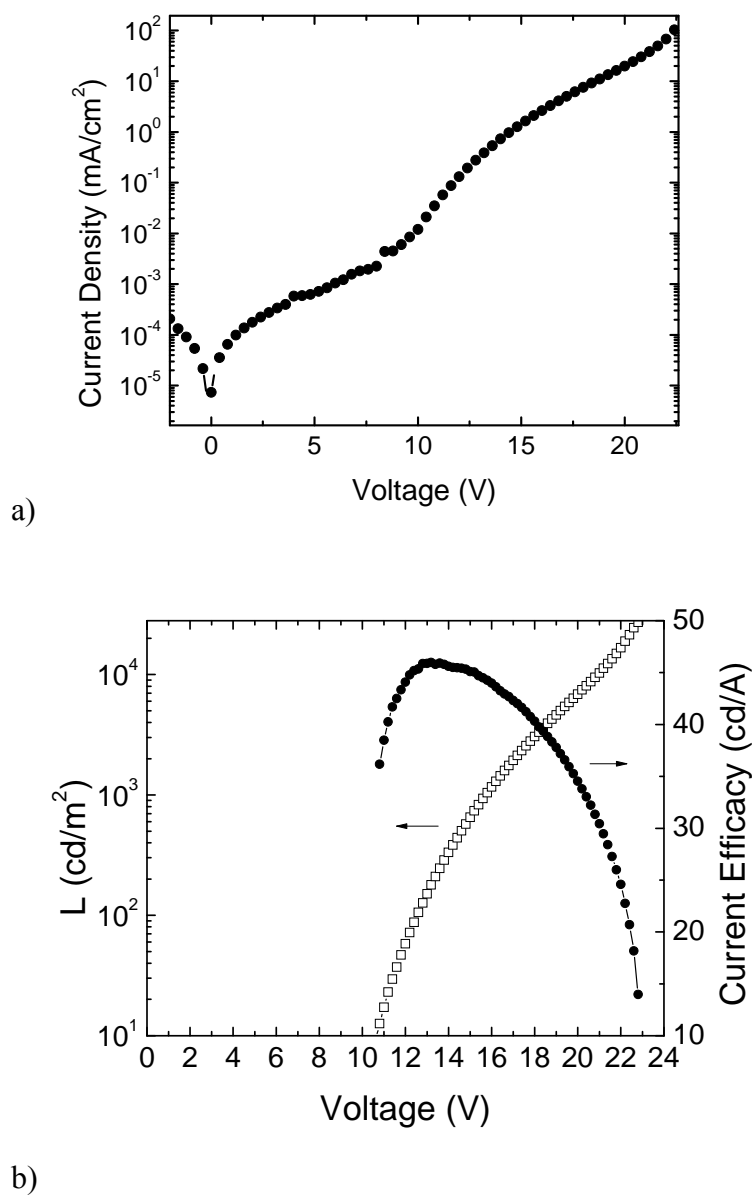
Fig. 6.2. a) Current density vs. voltage and b) luminance-voltage-current efficacy characteristics for un-optimized triple stacked OLEDs.

Recently there has been a great deal of research interest in a new class of emitter molecules known as thermally activated delayed fluorescence (TADF) emitters. These molecules are fluorescent emitters that are not based on heavy metals, and have been shown to be as efficient as their phosphorescent counterparts in the context of conventional bottom-emitting

OLEDs (cite literature). A preliminary experiment employing one of these emitters in our inverted top-emitting OLEDs was undertaken by simply substituting a phthalonitrile derivative (4s,6s)-2,4,5,6-tetra(9H-carbazol-9-yl)isophthalonitrile (4CzIPN) TADF emitter in the device architecture shown in Fig. 6.3. The device performances of these devices are shown in Fig. 6.4 and the spectral characteristics are shown in Fig. 6.5.
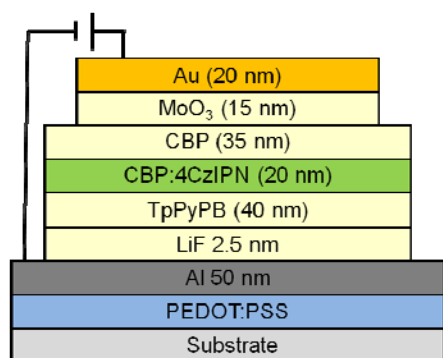
Fig. 6.3. Device architecture for devices employing TADF emitter 4CzIPN in the inverted top-emitting architecture.
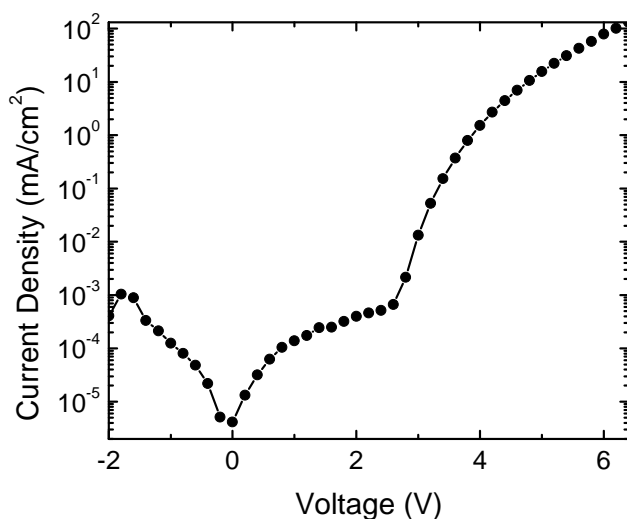
a)
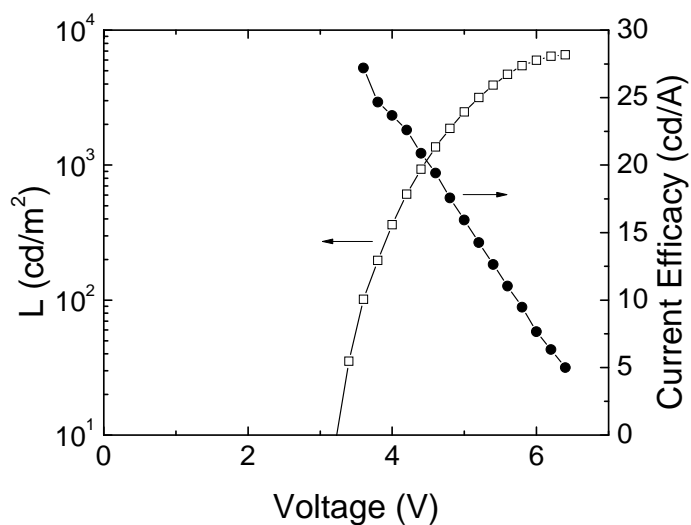
b)

Fig. 6.4. a) Current density vs. voltage and b) luminance-voltage-current efficacy characteristics for un-optimized inverted top-emitting OLEDs employing TADF emitter.
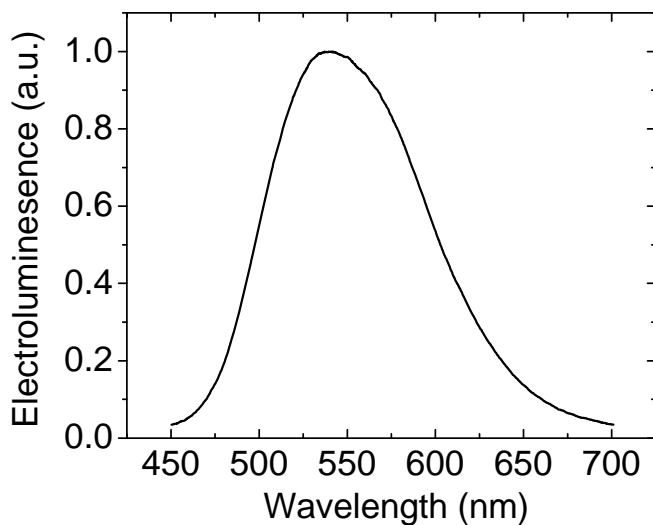
Fig. 6.5. Spectral characteristic for un-optimized inverted top-emitting OLEDs employing TADF emitter.

It can be observed that while these devices work, they are far from optimized. They achieve far lower current efficacies (a maximum of 27 cd/A at 10 cd/m^2) than devices with the same architecture which employ Ir(ppy)$_3$ phosphorescent emitters. It is foreseeable that with

research, improvement of these OLEDs different transporting layers to achieve charge balance could lead to fluorescent inverted top-emitting OLEDs with similar current efficacies as phosphorescent OLEDs having this novel architecture.

Appendix A: OLED Materials

OLEDs are multilayer devices that are comprised of different categories of materials, such as metal electrodes, inorganic metal-oxides, and organic transport materials. Some of the materials that comprise OLEDs and specifically those that pertain to the inverted top-emitting OLEDs in this thesis are discussed in this appendix.

A.1 Anode

As mentioned in section 1.4, the function of the anode in an OLED is to efficiently inject holes. In order to function as an effect electrode, the anode materials have a high electrical conductivity (greater than 1×10^6 Ω^{-1} m^{-1} [1]) so as to reduce contact resistance to electrical leads, have a low sheet resistance (10-15 Ω/sq.) so that the OLED device can be uniformly illuminated (especially in large-area applications, as discussed in reference [2]), have a high work function (greater than 4.1 eV) to promote efficient hole injection to known hole-transporting materials, have good film-forming and wetting properties with applied organic materials, and either be transparent for bottom-emitting OLEDs, or highly reflective if used in top-emitting OLEDs.

For bottom-emitting OLEDs, one common anode choice is indium tin oxide (ITO). ITO is transparent in the visible range (greater than 85% in the 400-700 nm part of the spectrum [3]), due to its large band gap of over 4.0 eV. It has a high conductivity, which for a 300 nm thick films grown at room temperature in oxygen pressure of 10 mTorr, is 2.6×10^{-3} $\Omega^{-1}cm^{-1}$ [4]. Additionally ITO has a work function between 4.5 to 5 eV, depending on preparation conditions [5]. Oxygen plasma treatment (see section 3.1.3) can increase the work function by as much as 0.5 eV. Other transparent, conductive electrodes exist, such as fluorine doped tin oxide (FTO) [6], and aluminum-doped zinc oxide (AZO) [7]. However since ITO is used frequently in the more established liquid crystal display (LCD) technology, it is the most readily available.

ITO, however, has many several key disadvantages as relates to organic electronics. It is brittle, has high resistivity (~2 $x10^4$ Ω-cm), moderate surface roughness (typically ~5 nm), a

chemically reactive surface, and a low and variable WF (4.5–4.8 eV), leading to hole injection difficulties with some materials. In many instances, deposition of ITO must be followed by annealing of the film at quite high temperature (greater than 200 °C) to reduce the resistivity to acceptable levels [8]. Such high-temperature annealing processes are precluded for plastic substrates which cannot withstand that level of heat.

In the inverted top-emitting OLEDs in this thesis, thin films of metals such as Au and Ag are used to inject holes and are the top semi-transparent anode. When used in combination with effective hole injection materials, they inject holes efficiently into hole transporting materials. In addition they do not have the disadvantages of ITO that are mentioned above. In particular they are flexible, easy to thermally evaporate, have high conductivity, and are not chemically reactive. However, they absorb more light that ITO and therefore reduce the amount of generated light that can exit the device.

A.2 Cathode

In an OLED the function of the cathode is to efficiently inject electrons. Therefore it often consists of a low work function metals such as Mg, Ca, and Ba to promote electron injection into known electron transporting materials. However, low work function metals are also highly chemical reactive. Direct chemical reduction of organic materials in contact with such low work function metals can lead to device degradation. In OLEDs, a combination of less reactive, higher work function metals such as Al and Ag are preferred. A thin layer of lithium fluoride (LiF) is often used in conjunction with Al ($\phi_f = 4.2$ eV), to form an effective LiF/Al top cathode LiF/Al ($\phi_f = 3.6$–3.8 eV) [9].

Al/LiF is the bottom cathode that is used in the inverted top-emitting OLEDs in this thesis. In non-inverted OLEDs where the deposition sequence is LiF followed by Al, there have been a number of mechanisms have proposed to explain the better charge injection of Al/LiF compared with bare Al. These include electron tunneling through a thin insulator layer [10],band bending at the metal/organic interface [10], lowering of the work function of Al [11], the presence of interfacial dipoles [12] and LiF dissociation that lead to a release of Li atoms and Alq_2^+ anions [9] (see section 4.2 for more details).

Some other typical cathode structures are Ca/Al, Mg/Ag (ϕ_f = 2.9 eV), and Ba/Al (ϕ_f = 2.6 eV). The work function of these cathode combinations is not fixed at these values, but rather is affected by material purity, deposition method (thermal evaporation, sputtering, electron beam deposition, etc.), morphology and roughness, and the crystal orientation.

In addition other electron injection materials besides LiF have been used such as CsF [13], lithium [14] or cesium doped thin electron transport layers [15], and organic polymers. The optimized thickness such electron injection layers is usually about 0.3–3.0 nm.

A.3 Electron Transport Material

The function of the electron transport materials is to aid in the transport of electrons from the cathode of the OLED to the emissive layer. Effective electron transport materials have a low electron affinity (generally less than 3.2 eV) to facilitate charge injection from the cathode by matching the work-function of known non-reactive cathode/electron-injection layer materials. They typically have high electron mobility values to facilitate the transport of electrons after injection, and high triplet energy to prevent the diffusion of triplet excitons from the neighboring

emissive layer of phosphorescent OLED devices. In addition, they have high thermal stability to withstand resistive Joule heating during device operation and to resist crystallization.

The metal chelate tris(8-hydroxyquinolinato)aluminium, Alq_3 (see Fig. A1), was the first emission and electron transport material explored by the Kodak group at the inception of the OLED field [16]. Interestingly, it is still a prevalently used as an electron transport, emissive layer, and host material in OLEDs. This is due to its high thermal stability (Alq_3 has a glass transition temperature, T_g, of 172 °C [17]). Almost all long-lived OLED devices include Alq_3 as the ETL. It has an electron affinity of 3.0 eV [18], an electron mobility of 1.4 x 10^{-6} (V/cm^2 s), and a hole mobility of 2.0 x 10^{-8} (V/cm^2 s) as estimated by time-of-flight (TOF) measurements (for description of this technique, refer to section 2.2.4) [19].
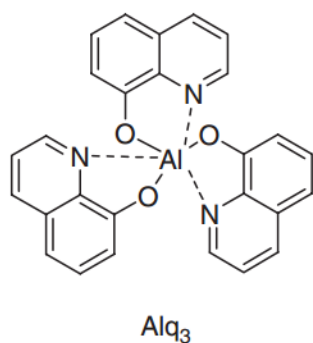
Alq_3

Fig. A1. Chemical structure for electron transporting, emissive host, and fluorescent emitter material tris(8-hydroxyquinolinato)aluminium (Alq_3).

(a)   (b)
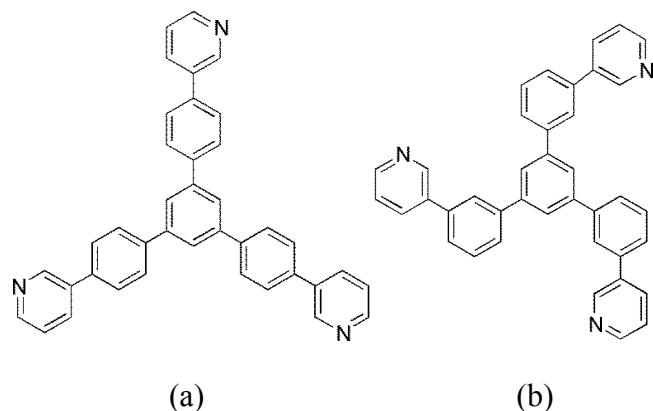
Fig. A2. Chemical structures for electron transporting materials a) 1,3,5-tri(p-pyrid-3-yl-phenyl)benzene (TpPyPB), and b) (TmPyPB).

In this research two pyridine-containing triphenylbenzene derivatives, TpPyPB and

TmPyPB (see Fig. A2) are used in the inverted top-emitting OLEDs. These compounds were

synthesized first by the group of Kido in reference [20]. These compounds showed exceptionally

high electron mobility (as measured by TOF), almost three orders of magnitude higher than Alq_3.

The electron mobility of TpPyPB (3.4-7.9 cm^2/V-s at electric field values between 2.7-6.1 $\times 10^5$

V/cm) is among the highest for known electron transporting materials. TpPyPB's mobility is

several times higher than that of TmPyPB (7.0 to 1.0 cm^2/V-s at electric fields between 2.5 and

6.4 $\times 10^5$ V/cm) due to the former's planer molecular structure and more delocalized π-

conjugation, which more readily facilitates electron hopping between molecules in an amorphous

thin film. The HOMO levels of TmPyPB and TpPyPB are 6.68 and 6.66 eV, respectively, which

are much larger than those of present used triplet emitters and hosts. Additionally their triplet

energy levels are 2.78 and 2.57 eV, For TmPyPB and TpPyPB respectively, compared with 2.65

eV and 2.55 eV for the phosphorescent blue and green emitters FIrpic [21] and Ir(ppy)₃ [22],

respectively. Together, these factors allow for good confinement of holes within the emissive

layer in an OLED device, leading to well charge-balanced, highly efficient devices.

157

A.4 Emissive Layer

The emissive layer of the OLED is where excitons form and radiatively decay to produce light. As discussed in section 2.5, the host material harvests singlet transfers singlet and triplet excitons to the guest material where they are transferred to the lowest triplet level of the phosphorescent host by both Förster and Dexter transfer mechanisms, allowing for emission from both triplet and singlet states for high internal quantum efficiency.

Among the many criteria for a host:guest emissive layer material is that the host is that it have matching ionization energy/HOMO and electron affinity/LUMO energy levels with the guest materials. For efficient energy transfer, the LUMO energy level of the host normally is typically shallower than the corresponding LUMO energy level of the guest, with respect to the vacuum level. Likewise, the HOMO energy level of the host is typically deeper than that of the guest. For emissive layers containing phosphorescent guest dopants, the triplet energy level of the host normally is usually higher than that of the guest. In addition, the host:guest system has good ambipolar charge transport for exciton formation, and has good thermal, chemical, and electrical stability.

(a)   (b)
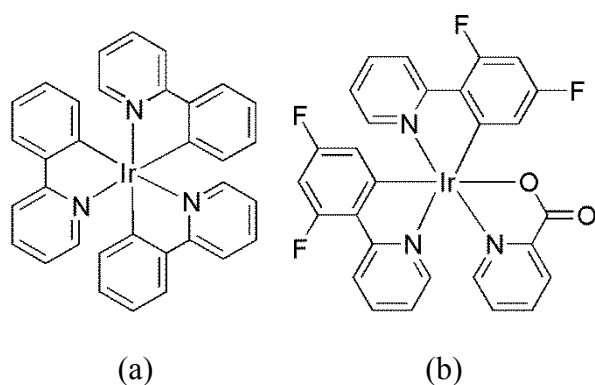
Fig. A3. Chemical structure for a) green phosphorescent dopant Tris[2-phenylpyridinato-C2,N]iridium(III) (Ir(ppy)$_3$) and b) blue phosphorescent dopant Bis[2-(4,6-difluorophenyl)pyridinato-C^2,N](picolinato)iridium(III) (FIrpic).
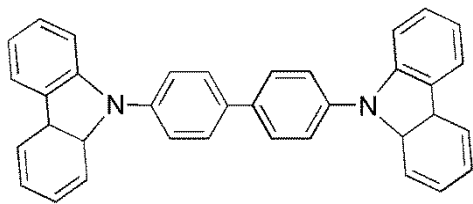
Fig. A4. Chemical structure for host emissive layer material 4,4′-Bis(9-carbazolyl)-1,1′-biphenyl (CBP).

The emissive layer is typically composed of the material system 4′-Bis(9-carbazolyl)-1,1′-biphenyl (CBP) doped with tris[2-phenylpyridinato-C2,N]iridium(III) (Ir(ppy)$_3$) for green phosphorescent OLEDs and the inverted top-emitting OLEDs in this research (see Fig A3a and Fig. A4). The HOMO and LUMO energy levels of CBP are 6.30 and 3.0 eV, respectively. The triplet energy level of CBP is 2.67 eV. CBP has an ambipolar charge transport quality [23]. For these reasons, CBP is considered a good host material for green, yellow, and red triplet phosphorescent emitters. However, the triplet energy level of CBP is too low to yield efficient devices with blue emitters. For instance, the blue emitter FIrpic (see Fig. A3b) has a higher triplet energy level (2.75 eV) compared with CBP. The energy transfer process of a CBP:FIrpic system is best characterized as endothermic and produces a low-efficiency device [24]. However, a related compound to CBP has a large band-gap host material is N,N'-dicarbazolyl-3,5-benzene (mCP) [25]. Notably, mCP and CBP have similar charge injection and transport properties, but mCP has a triplet energy of 3.0 eV, allowing for efficient energy transfer to the triplet emitter guest. In fact, using mCP as a host and FIrpic as the blue phosphorescent dopant in the blue unit for our stacked white inverted top-emitting OLEDs.

A.5 Hole Injection Material

Hole injection materials are used to improve the injection of holes into the hole transporting materials used in the OLED device leading to lower turn-on voltages. A wide variety of hole injection materials exists, many of which are designed for to increase the work function of ITO and thereby reduce the barrier to hole injection. Conducting polymers such as poly(3,4-ethylenedioxythiophene) poly(styrenesulfonate) (PEDOT:PSS) are often used with ITO for this purpose. A spin-coated PEDOT:PSS layer can improve surface smoothness, and increase the work function of ITO [26]. However one downside to using PEDOT:PSS is that it is strongly acidic due to the doping necessary to induce conductivity. The acidity can, in many instances, lead to ITO corrosion over time. Another commonly used hole injection material is the porphyrinic metal complex pigment copper phthalocyanine (CuPC), which was first implemented in an OLED by the Kodak group [27]. CuPC is a readily available semiconducting material that has high thermal stability. It is also often thermally evaporated onto ITO, where it is thought to increase the ITO work function to approximately 5.1 eV [28].

Another class of materials that has had widespread use in OLEDs are the metal oxides such as SiO_2, Si_3N_4, WO_3, MoO_3, and related compounds [29-31]. One commonly used metal oxides in organic electronics applications is MoO_3, because it is evaporated at relatively low temperature ($\sim 400°C$) and can be deposited in vacuum from a crucible. It is used in our inverted top-emitting OLEDs with a hole-transporting material of CBP.

160
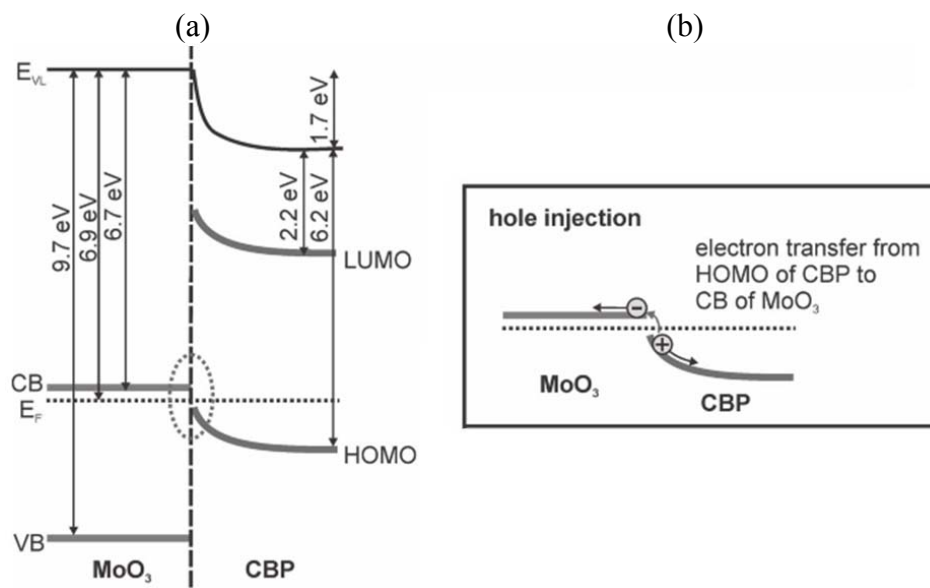
Fig. A5. Proposed mechanism for the effective use of MoO$_3$/CBP for hole injection. In (a) the IE (9.7 eV), EA (6.7 eV), and the energy difference between the Fermi level (E_F) and the vacuum level (E_{VL}) (6.9 eV) is shown for MoO$_3$. Also the EA (2.2 eV), the IE (6.2 eV) is shown for CBP as well as the vacuum level shift upon contact with MoO$_3$. The energy level alignment between the conduction band (CB) of MoO$_3$ and the HOMO level of CBP is shown in (a); the hole injection mechanism via electron transfer from the HOMO of CBP to the CB of MoO$_3$ is shown in (b). Taken from [32].

MoO$_3$ and other similar metal oxides are n-type materials exhibiting very deep lying electron affinity/LUMO levels. One proposed mechanism for the effective use of MoO$_3$/CBP for hole injection is shown in **Fig. A5**. The energy alignment between the conduction band of MoO$_3$ and the ionization energy of CBP leads to efficient electron transfer between the two materials. Hole-injection into CBP occurs by an electron transfer from the HOMO level of CBP to the conduction band of MoO$_3$ upon the application of positive bias to the anode. The left over hole is then collected by the anode. Thus the metal oxide/organic interface converts a hole current into an electron current and is sometimes referred to as a "charge generation" layer in the literature.
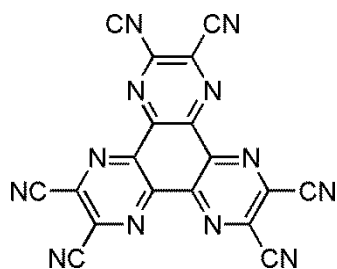
Fig. A6. Chemical structure for hole injection material 1,4,5,8,9,11-hexaazatriphenylene hexacarbonitrile (HAT-CN).

Like TCOs, 1,4,5,8,9,11-hexaazatriphenylene hexacarbonitrile (HAT-CN) (see Fig. A6) has been used in the connecting-units of stacked OLEDs [18],[19] and a hole-generating organic interlayer in single-unit OLEDs [20]. In terms of energy levels and charge injection mechanism HAT-CN acts similarly to metal oxides such as MoO_3. It is an electron acceptor that has also been used as an p-dopant [21] due to its large electron affinity that has a value comparable to that of the ionization energy (IE) of common HTLs. A thick layer of HAT-CN has been used as a buffer layer for the sputter deposition of an indium zinc oxide anode on a transparent inverted OLED [24]. HAT-CN has a HOMO level of 4.4-6.0 eV ([33],[34]) and it has been shown to increase the work function of Ag by 1 eV [35]. It is used in conjunction with Ag as a novel top-anode in some the green inverted top-emitting phosphorescent OLEDs described in section 4.3.

A.6 Hole Transport Materials

Hole transporting materials serve to aid in the transport of positive charge carriers (holes) from the anode into the emissive layer of the OLED. Effective hole transport materials typically have a high ionization energy (greater than than 5 eV) to facilitate charge injection from the anode by matching the work-function of known anode/hole-injection layer materials. They also have high hole mobility values to assist the transport of holes after injection, and a high triplet energy to prevent the diffusion of triplet excitons from the emissive layer of phosphorescent

162

OLED devices. In addition, they also commonly have high thermal stability to withstand resistive Joule heating during device operation and to resist to crystallization. Many hole transport materials are designed to have a low electron affinity (corresponding to a high LUMO level) in order to act as an electron blocking layer. This is to confine electrons to the emissive layer and form excitons.

The most commonly used hole transport materials are triarylamine compounds, such as N,N'-Di-[(1-naphthyl)-N,N'-diphenyl]-(1,1'-biphenyl)-4,4'-diamine (α-NPD) (see Fig. A7) and 1,1-bis-(4-bis(4-tolyl)-aminophenyl)cyclohexene (TAPC) (see Fig. A8). These compounds were initially developed as materials for photoconductive applications such as xerography [36]. They have been used for OLED applications mainly from ready availability and their good electric and thermal stabilities. The hole mobilities of these materials often exceeds the corresponding electron mobilities of most electron transporting materials.
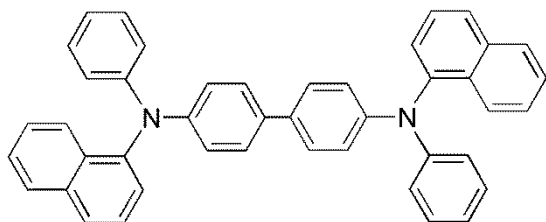

Fig. A7. Chemical structure for hole transporting material N,N'-Di-[(1-naphthyl)-N,N'-diphenyl]-(1,1'-biphenyl)-4,4'-diamine (α-NPD).
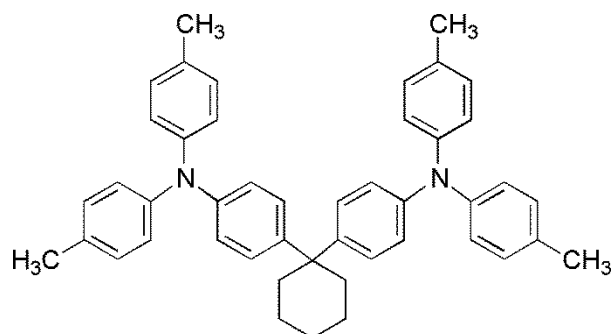
Fig. A8. Chemical structure for hole transporting material 1,1-bis-(4-bis(4-tolyl)-aminophenyl)cyclohexene (TAPC).

A.7 Summary

A brief overview of some of the key materials used in this research has been given in this appendix. Some of their most important electrical parameters are shown in Table 1.

Table A1. Summary of key parameters for various tranport, emissive host, and phosphorescent dopant organic materials used in this research.

Material Name	Typical Role In OLED Devices	HOMO/IE (eV)	LUMO/EA (eV)	Triplet Energy (eV)	Mobility cm^2/V-s (at Given E-Field (V/cm))
TpPyPB	Electron Transport Material	6.66	3.04	2.57	7.9×10^{-3} (6.1×10^5) [20]
TmPyPB	Electron Transport Material	6.68	2.73	2.78	1.0×10^{-3} (6.4×10^5)
CBP	Emissive Layer Host Material	6.1-6.3	2.8-3.0	2.56	$\mu_e = 3.0 \times 10^{-4}$ $\mu_h = 2.0 \times 10^{-3}$ (5.0×10^5) **[37]**
mCP	Emissive Layer Host Material	5.8	2.3	2.65	$\mu_e = 2.0 \times 10^{-4}$ $\mu_h = 3.2 \times 10^{-4}$ (1.6×10^5) [38]
Ir(ppy)₃ [32]	Phosphorescent Dopant	5.47	3.01	2.55	
FIrpic [21]	Phosphorescent Dopant	5.8–6.15	2.9–3.47	2.65	
(Ir(Mphq)₃ [39]	Phosphorescent Dopant	4.66	2.83	2.0	
TAPC	Hole Transport Material	5.4	1.84	2.87	6.3×10^{-3} (2.2×10^6) [40]
α-NPD	Hole Transport Material	5.47	1.52	2.29	1.0×10^{-3} (3.6×10^5) [41]
MoO₃ [32]	Hole Injection Material	9.7	6.7		
HAT-CN [33, 34, 42]	Hole Injection Material	9.5	4.4-6.0		

A.8 References

[1] A.K. Kulkarni, K.H. Schulz, T.S. Lim, M. Khan, Dependence of the sheet resistance of indium-tin-oxide thin films on grain size and grain orientation determined from X-ray diffraction techniques, Thin Solid Films, 345 (1999) 273-277.
[2] S. Choi, W.J. Potscavage, B. Kippelen, ITO-free large-area organic solar cells, Optical Express, 18 (2010) A458-A466.

[3] H. Kim, A. Pique, J.S. Horwitz, H. Mattoussi, H. Murata, Z.H. Kafafi, D.B. Chrisey, Indium tin oxide thin films for organic light-emitting devices, Applied Physics Letters, 74 (1999) 3444-3446.

[4] H. Kim, J.S. Horwitz, A. Piqué, C.M. Gilmore, D.B. Chrisey, Electrical and optical properties of indium tin oxide thin films grown by pulsed laser deposition, Applied Physics A, 69 (1999) S447-S450.

[5] T. Nagatomo, Y. Maruta, O. Omoto, Electrical and optical properties of vacuum-evaporated indium-tin oxide films with high electron mobility, Thin Solid Films, 192 (1990) 17-25.

[6] T. Kawashima, H. Matsui, N. Tanabe, New transparent conductive films: FTO coated ITO, Thin Solid Films, 445 (2003) 241-244.

[7] N.W. Schmidt, T.S. Totushek, W.A. Kimes, D.R. Callender, J.R. Doyle, Effects of substrate temperature and near-substrate plasma density on the properties of dc magnetron sputtered aluminum doped zinc oxide, Journal of applied physics, 94 (2003) 5514-5521.

[8] H. Tomonaga, T. Morimoto, Indium–tin oxide coatings via chemical solution deposition, Thin Solid Films, 392 (2001) 243-248.

[9] M.G. Mason, C.W. Tang, L.S. Hung, P. Raychaudhuri, J. Madathil, D.J. Giesen, L. Yan, Q.T. Le, Y. Gao, S.T. Lee, Interfacial chemistry of Alq3 and LiF with reactive metals, Journal of applied physics, 89 (2001) 2756-2765.

[10] L.S. Hung, C.W. Tang, M.G. Mason, Enhanced electron injection in organic electroluminescence devices using an Al/LiF electrode, Applied Physics Letters, 70 (1997) 152.

[11] S.E. Shaheen, G.E. Jabbour, M.M. Morrell, Y. Kawabe, B. Kippelen, N. Peyghambarian, M.F. Nabor, R. Schlaf, E.A. Mash, N.R. Armstrong, Bright blue organic light-emitting diode with improved color purity using a LiF/Al cathode, Journal of Applied Physics, 84 (1998) 2324-2327.

[12] M.A. Baldo, S.R. Forrest, Interface-limited injection in amorphous organic semiconductors, Physical Review B, 64 (2001) 085201.

[13] J. Kido, T. Matsumoto, Bright organic electroluminescent devices having a metal-doped electron-injecting layer, Applied Physics Letters, 73 (1998) 2866-2868.

[14] G. Chimed, F. Masamichi, A Lithium Carboxylate Ultrathin Film on an Aluminum Cathode for Enhanced Electron Injection in Organic Electroluminescent Devices, Japanese Journal of Applied Physics, 38 (1999) L1348.

[15] G. He, M. Pfeiffer, K. Leo, M. Hofmann, J. Birnstock, R. Pudzich, J. Salbeck, High-efficiency and low-voltage p-i-n electrophosphorescent organic light-emitting diodes with double-emission layers, Applied Physics Letters, 85 (2004) 3911-3913.

[16] X. Zheng, Y. Wu, R. Sun, W. Zhu, X. Jiang, Z. Zhang, S. Xu, Efficiency improvement of organic light-emitting diodes using 8-hydroxy-quinolinato lithium as an electron injection layer, Thin Solid Films, 478 (2005) 252-255.

[17] K.A. Higginson, X.-M. Zhang, F. Papadimitrakopoulos, Thermal and morphological effects on the hydrolytic stability of aluminum tris (8-hydroxyquinoline)(Alq3), Chemistry of Materials, 10 (1998) 1017-1020.

[18] J.D. Anderson, E.M. McDonald, P.A. Lee, M.L. Anderson, E.L. Ritchie, H.K. Hall, T. Hopkins, E.A. Mash, J. Wang, A. Padias, Electrochemistry and electrogenerated chemiluminescence processes of the components of aluminum quinolate/triarylamine, and related organic light-emitting diodes, Journal of the American Chemical Society, 120 (1998) 9646-9655.

[19] R.G. Kepler, P.M. Beeson, S.J. Jacobs, R.A. Anderson, M.B. Sinclair, V.S. Valencia, P.A. Cahill, Electron and hole mobility in tris(8-hydroxyquinolinato)aluminium, Applied Physics Letters, 66 (1995) 3618-3620.

[20] S.-J. Su, T. Chiba, T. Takeda, J. Kido, Pyridine-Containing Triphenylbenzene Derivatives with High Electron Mobility for Highly Efficient Phosphorescent OLEDs, Advanced Materials, 20 (2008) 2125-2130.

[21] S.-J. Su, H. Sasabe, T. Takeda, J. Kido, Pyridine-containing bipolar host materials for highly efficient blue phosphorescent OLEDs, Chemistry of materials, 20 (2008) 1691-1693.

[22] K. Goushi, R. Kwong, J.J. Brown, H. Sasabe, C. Adachi, Triplet exciton confinement and unconfinement by adjacent hole-transport layers, Journal of Applied Physics, 95 (2004) 7798-7802.

[23] H. Kanai, S. Ichinosawa, Y. Sato, Effect of aromatic diamines as a cathode interface layer, Synthetic Metals, 91 (1997) 195-196.

[24] C. Adachi, R.C. Kwong, P. Djurovich, V. Adamovich, M.A. Baldo, M.E. Thompson, S.R. Forrest, Endothermic energy transfer: A mechanism for generating very efficient high-energy phosphorescent emission in organic materials, Applied Physics Letters, 79 (2001) 2082-2084.

[25] R.J. Holmes, S.R. Forrest, Y.J. Tung, R.C. Kwong, J.J. Brown, S. Garon, M.E. Thompson, Blue organic electrophosphorescence using exothermic host–guest energy transfer, Applied Physics Letters, 82 (2003) 2422-2424.

[26] W.H. Kim, A.J. Makinen, N. Nikolov, R. Shashidhar, H. Kim, Z.H. Kafafi, Molecular organic light-emitting diodes using highly conducting polymers as anodes, Applied Physics Letters, 80 (2002) 3844-3846.

[27] S.A. Van Slyke, C.H. Chen, C.W. Tang, Organic electroluminescent devices with improved stability, Applied Physics Letters, 69 (1996) 2160.

[28] F. Nuesch, M. Carrara, M. Schaer, D.B. Romero, L. Zuppiroli, The role of copper phthalocyanine for charge injection into organic light emitting devices, Chemical Physics Letters, 347 (2001) 311-317.

[29] Z.B. Deng, X.M. Ding, S.T. Lee, W.A. Gambling, Enhanced brightness and efficiency in organic electroluminescent devices using SiO2 buffer layers, Applied Physics Letters, 74 (1999) 2227-2229.

[30] C.O. Poon, F.L. Wong, S.W. Tong, R.Q. Zhang, C.S. Lee, S.T. Lee, Improved performance and stability of organic light-emitting devices with silicon oxy-nitride buffer layer, Applied Physics Letters, 83 (2003) 1038-1040.

[31] Z. Zhi-Feng, D. Zhen-Bo, L. Chun-Jun, Z. Meng-Xin, X. Deng-Hui, Organic light-emitting diodes with a nanostructured TiO2 layer at the interface between ITO and NPB layers, Displays, 24 (2003) 231-234.

[32] J. Meyer, S. Hamwi, M. Kröger, W. Kowalsky, T. Riedl, A. Kahn, Transition metal oxides for organic electronics: Energetics, device physics and applications, Advanced Materials, 24 (2012) 5408-5427.

[33] T. Chiba, Y.-J. Pu, R. Miyazaki, K.-i. Nakayama, H. Sasabe, J. Kido, Ultra-high efficiency by multiple emission from stacked organic light-emitting devices, Organic Electronics, 12 (2011) 710-715.

[34] Y.-K. Kim, J. Won Kim, Y. Park, Energy level alignment at a charge generation interface between 4, 4′-bis (N-phenyl-1-naphthylamino) biphenyl and 1, 4, 5, 8, 9, 11-hexaazatriphenylene-hexacarbonitrile, Applied Physics Letters, 94 (2009) 063305-063305.

[35] B. Bröker, O.T. Hofmann, G.M. Rangger, P. Frank, R.P. Blum, R. Rieger, L. Venema, A. Vollmer, K. Müllen, J.P. Rabe, Density-dependent reorientation and rehybridization of chemisorbed conjugated molecules for controlling interface electronic structure, Physical Review Letters, 104 (2010) 246805.

[36] A.M. Horgan, Composite layered imaging member for electrophotography, Google Patents, 1977.

[37] J.-W. Kang, S.-H. Lee, H.-D. Park, W.-I. Jeong, K.-M. Yoo, Y.-S. Park, J.-J. Kim, Low roll-off of efficiency at high current density in phosphorescent organic light emitting diodes, Applied Physics Letters, 90 (2007) 223508-223508.

[38] J.-H. Jou, W.-B. Wang, S.-Z. Chen, J.-J. Shyue, M.-F. Hsu, C.-W. Lin, S.-M. Shen, C.-J. Wang, C.-P. Liu, C.-T. Chen, High-efficiency blue organic light-emitting diodes using a 3, 5-di (9H-carbazol-9-yl) tetraphenylsilane host via a solution-process, Journal Material Chemistry, 20 (2010) 8411-8416.

[39] D.H. Kim, N.S. Cho, H.Y. Oh, J.H. Yang, W.S. Jeon, J.S. Park, M.C. Suh, J.H. Kwon, Highly Efficient Red Phosphorescent Dopants in Organic Light-Emitting Devices, Advanced Materials, 23 (2011) 2721-2726.

[40] P.M. Borsenberger, L. Pautmeier, R. Richert, H. Bässler, Hole transport in 1, 1-bis (di-4-tolylaminophenyl) cyclohexane, The Journal of Chemical Physics, 94 (1991) 8276.

[41] S. Naka, H. Okada, H. Onnagawa, Y. Yamaguchi, T. Tsutsui, Carrier transport properties of organic materials for EL device operation, Synthetic Metals, 111 (2000) 331-333.

[42] B.B. Diouf, W.S. Jeon, J.S. Park, J.W. Choi, Y.H. Son, D.C. Lim, Y.J. Doh, J.H. Kwon, High hole mobility through charge recombination interface in organic light-emitting diodes, Synthetic Metals, 161 (2011) 2087-2091.

Appendix B: Optics for OLED Characterization

In this appendix, we offer some basic background in photometry and radiometry. An understanding of basic optics needed to fully characterize the inverted top-emitting OLEDs discussed in this thesis is provided.

B.1 Relevant Scales for Emitted OLED Light

Electromagnetic radiation oscillates in waves that vary many orders of magnitudes in wavelength (or frequency) as can be seen in Fig. B1. Visible light falls in the range of 380 to 780 nm (1.59 to 3.26 electron volts, eV, where 1 eV $\approx 1.60 \times 10^{-19}$ J). Immediately outside the range of human perception is ultraviolet radiation (UV) with a wavelength range of 10 to 380 nm (3.26 to 124 eV) and infrared radiation (IR) with a wavelength range of 0.78 to 300 µm (0.004 to 1.59 eV).
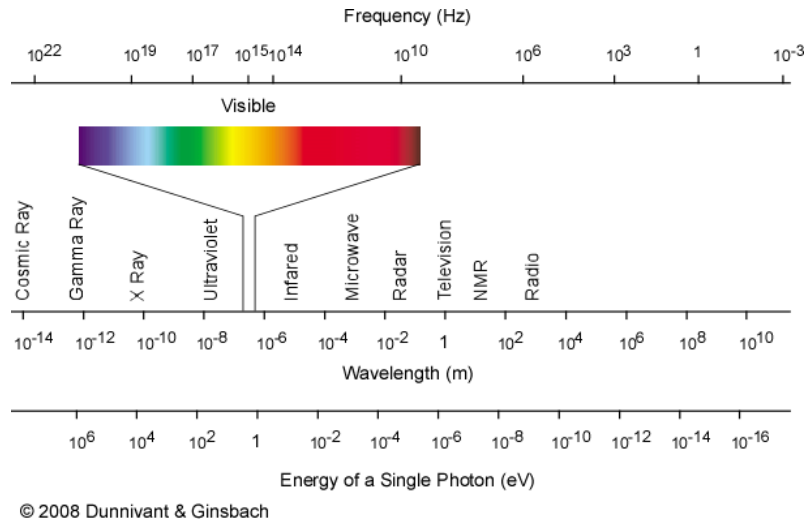
Fig. B1. A diagram showing frequency (in Hz), wavelength (in m), and energy scales (in eV) of the electromagnetic spectrum. Reproduced from [1].

B.2 Perception of the Human Eye

The measurement of light sources (such as OLEDs for display and lighting applications) requires accounting for the perception of the human eye. This entails the use of the photometric equivalents of radiometric quantities. Radiometry is the science of the detection and

measurement of radiation, including visible light. Photometry, on the other hand, is the science of the measurement and detection of only visible light, in terms of its perceived brightness to the human eye.

B.3 Radiometric Characterization of Light

Radiometry characterizes the distribution of radiation's power in space, irrespective of its interaction with the human eye. To conduct the radiometric characterization of OLEDs, several definitions must first be introduced [2].

Radiant flux Φ_e is a measure of the optical power (i.e. radiant energy per unit time) emanating from a light source and is measured in watts [W] (or [J/s]). The subscript e is used to denote energy, which will be used to denote any radiometric quantity. Radiant intensity I_e is defined as radiant flux per unit solid angle Ω.

$$I_e = \frac{d\Phi_e}{d\Omega} \tag{B1}$$

The solid angle is the three-dimensional analogue of an angle that an object subtends at a point. It is measured in units of steradian, [sr]. Radiant intensity therefore has a unit of watt per steradian [W/sr]. In spherical coordniate system, the solid angle can be written as (see Fig. B2):

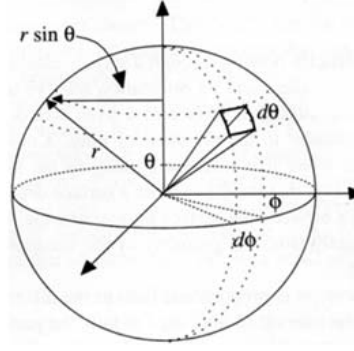$$d\Omega = r \sin\theta \, d\theta d\varphi \tag{B2}$$

Fig. B2. Spherical coordinate geometry for calculating the differential solid angle $d\Omega$. A solid angle equals the area of a segment of unit sphere in the same way a planar angle equals the length of an arc of unit circle.

Radiance measures the quantity of radiation that passes through or is emitted from a surface and falls within a given solid angle in a specified direction. It is the radiant flux per unit solid angle per unit projected area of the radiator (or detector) source area, A_{proj}:

$$L_e = \frac{d^2\Phi_e}{dA_{proj}\,d\Omega} = \frac{d^2\Phi_e}{dA\,d\Omega\cos\theta} \qquad (B3)$$

and is in units of [W/m^2-sr] with θ representing the angle between the normal vector of the projected area plane and the vector normal to the source area plane. When referring to radiance emitted by a source, A_{proj} is the projected area of the source, and Ω is the solid angle into which light is emitted. When referring to radiance falling onto a detector, A_{proj} is the projected area of the detector and Ω to the solid angle subtended by the source as viewed from that detector. Projected area is the rectilinear projection of a surface of any shape onto a plane normal to the unit vector. In differential form it is given by

$$dA_{proj} = \cos\theta\,dA \qquad (B4)$$

where θ is the angle between the local surface normal and the vector pointing in the line of sight. In the approximation of small areas A and Ω (where $\cos\theta$ is approximately constant), radiance can be given by

$$L_e = \frac{I_e}{A \cos \theta} \qquad (B5)$$

Finally, <u>radiant efficiency</u> or <u>wall-plug efficiency</u> is a measurement of the efficiency of converting electrons to photons in a device. It is defined as the ratio of the radiant flux to the input electrical flux $\Phi_{electric}$ from the power source,

$$\eta_{\text{wall-plug}} = \frac{\Phi_e}{\Phi_{electric}} \qquad (B6)$$

and is unitless (i.e. [W/W]).

B.4 Photometric Characterization of Light

The light perceived by the human eye is not the same as the light emitted from a source. The Commission Internationale d'Eclairage (CIE), an organization established in 1913 that sought to produce lighting related technical standards, defined a standard visual response curve of the human eye to specify the average spectral sensitivity of visual perception [3]. This curve allows for a conventionally accepted conversion between radiometric and photometric units (Fig. B3). The human eye has its peak sensitivity in the green at 555 nm, as reflected in Fig. B3.
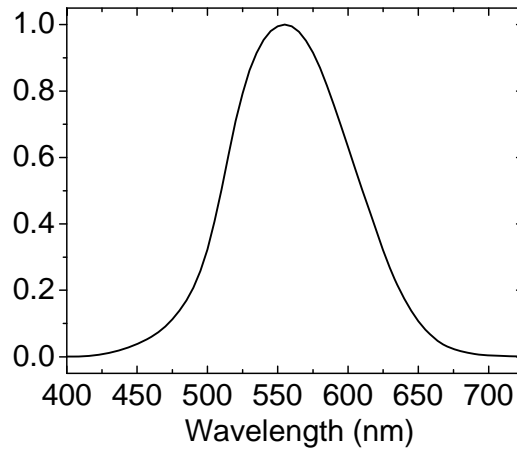

Fig. B3. The 1931 CIE standard visual response curve for characterizing the responsivity of the human eye.

171

In photometry the radiant power at each wavelength is weighted by the visual response of the human eye. The conversion between any given radiometric quantity X_e and its equivalent photometric quantity X_v is given through the formula,

$$X_v = 683 \frac{\text{lm}}{\text{W}} \int_{380\text{nm}}^{780\text{nm}} X_e \cdot V(\lambda) \, d\lambda \qquad (B7)$$

where $V(\lambda)$ is the visual response curve. As can be seen in this formula, the <u>lumen</u> [lm] is a unit that is used to quantify *luminous* flux (in contrast with *radiant* flux which is measured in watts). The lumen is a measure of the light emitted by a source weighed by the response of the human eye. Additionally, 1 lm = 1 cd·sr, where cd refers to a candela. The <u>candela</u> is the luminous intensity, in a given direction, of a source that emits monochromatic radiation of frequency 540×10^{12} Hz and that has a radiant intensity in that direction of 1/683 W/sr. This frequency was chosen to correspond to the corresponding to a wavelength of 555 nm.

In photometry, <u>luminance</u> is the equivalent of radiance in radiometry and is used to formally characterize the brightness of OLEDs. It is given typically in units of [cd/m^2] (also called a nit). A scale of luminance values for common sources of light is given in Fig. B4. Other analogous measurements between radiometric and photometric quantities include radiant efficiency [W/sr-A] as luminous efficacy [cd/A], and wall plug or power efficiency (dimensionless, i.e. [W/W], and therefore reported as a percentage) as luminous power efficacy [lm/W]. A summary of relevant radiometric and photometric measurements and their units is given in table B1.
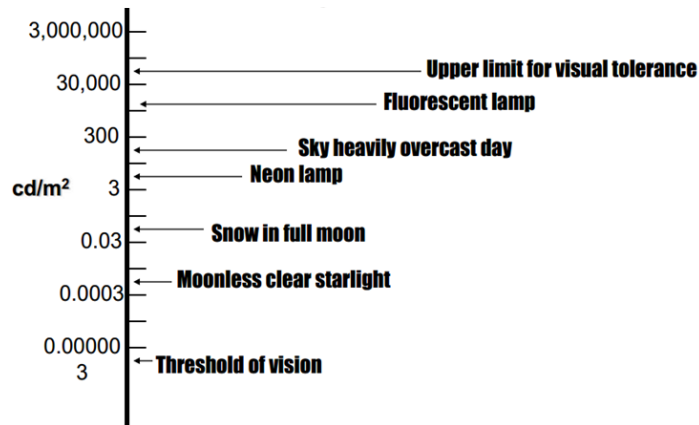
Fig. B4. The luminance values of some common sources of light.

Table B1. Radiometric units and their equivalent photometric units.

Radiometry	Photometry
Radiant flux: watt, [W]	Luminous flux, lumen (cd·sr), [lm]
Radiant intensity: watt per steradian, [W/sr]	Luminous intensity, candela (= lm/sr), [cd]
Radiance: watt per steradian per square metre, [W/m^2-sr]	Luminance, nits, [cd/m^2]
Wall plug efficiency: dimensionless [W/W]	Luminous efficacy, lumens per watt, [lm/W]

B.5 References

[1] F. Dunnivant, J. Ginsbach, Flame Atomic Absorbance and Emission Spectroscopy and Inductively Coupled Spectrometry - Mass Spectrometry, Whitman College, 2009.
[2] A. Parr, R. Datla, J. Gardner, Optical Radiometry, Elsevier Science, 2005.
[3] F. Grum, Radiometry, Elsevier Science, 2012.

Appendix C: Determination of OLED Performance Parameters

In this appendix, the key performance metrics for characterizing OLED light: color coordinates, luminance, and color rendition index are defined and derived.

C.1 Color Coordinate Determination

Visible light has a wavelength between 380 nm and 780 nm. The retina of the human eye has three different color receptors called cone cells. These cells primarily detect light of red, green, and blue colors. When light of a given spectrum enters the eye, it excites all the different cone types. The relative ratio of the cone cell types' spectral responses can be used to characterize the different colors that we observe.
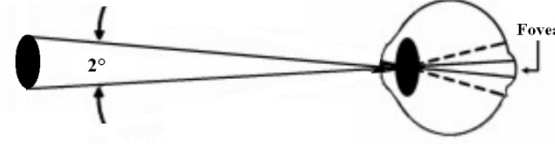

Fig. C1. Diagrammatic depiction of the CIE 1931 2° standard observer. Adapted from [1].

To standardize the spectral response of the average human eye, the CIE committee defined a <u>CIE 1931 2° standard observer</u> [2]. It represents the average chromatic response within a 2° arc inside the fovea of the human eye, where the cones primarily reside (see Fig. C1). So called tristimulus values (X, Y, Z) for this observer are then defined as

$$X = \int_{380}^{780} S_{Test}(\lambda)\bar{x}(\lambda)d\lambda, \ Y = \int_{380}^{780} S_{Test}(\lambda)\bar{y}(\lambda)d\lambda, \ Z = \int_{380}^{780} S_{Test}(\lambda)\bar{z}(\lambda)d\lambda \qquad (C1)$$

where S_{Test} is the spectral power distribution of the light and $\bar{x}(\lambda)$, $\bar{y}(\lambda)$, and $\bar{z}(\lambda)$ are called <u>color matching functions</u>. These functions are the chromatic response functions of the different red, green, and blue cone cells of standard observer and are shown in Fig. C2.
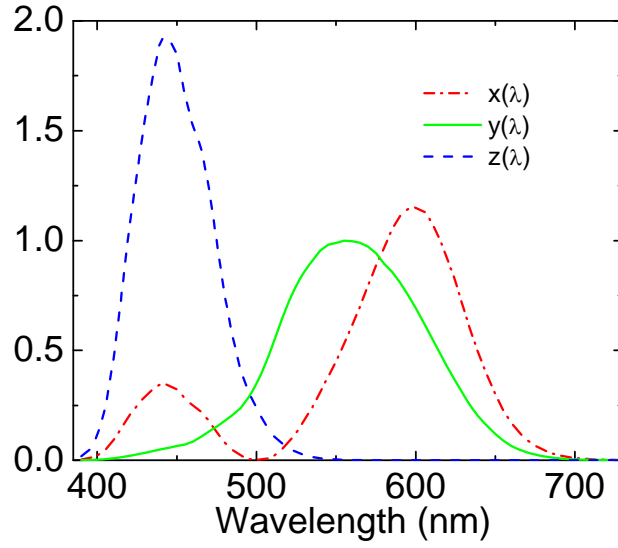
Fig. C2. The CIE 1931 color matching functions $\bar{x}(\lambda)$, $\bar{y}(\lambda)$, and $\bar{z}(\lambda)$, i.e. the chromatic response functions of the different red, green, and blue cone cells of a standard observer.

The tristimulus values (X, Y, Z) form a three-dimensional color space where they represent the amounts of three primary colors in an additive color model. A CIE 1960 color space was designed so that X represents the red response of the cone cells of the human eye, Y represents the green response and also luminosity, and Z represents the blue response. In this color space the brightness of a color is related to its distance from the origin (see Fig. C3a, where a series of colors are plotted in this color space). It is convenient to factor out the brightness from this color space and only plot colors of similar brightness level (see Fig. C3b). This is done by projecting the points in XYZ space onto the $X + Y + Z = 1$ plane, where the point of projection is the origin (see Fig. C3b). This is done by calculating the (x, y) coordinates of a given (X, Y, Z) coordinate:

$$x = \frac{X}{X + Y + Z} \qquad\qquad (C2)$$
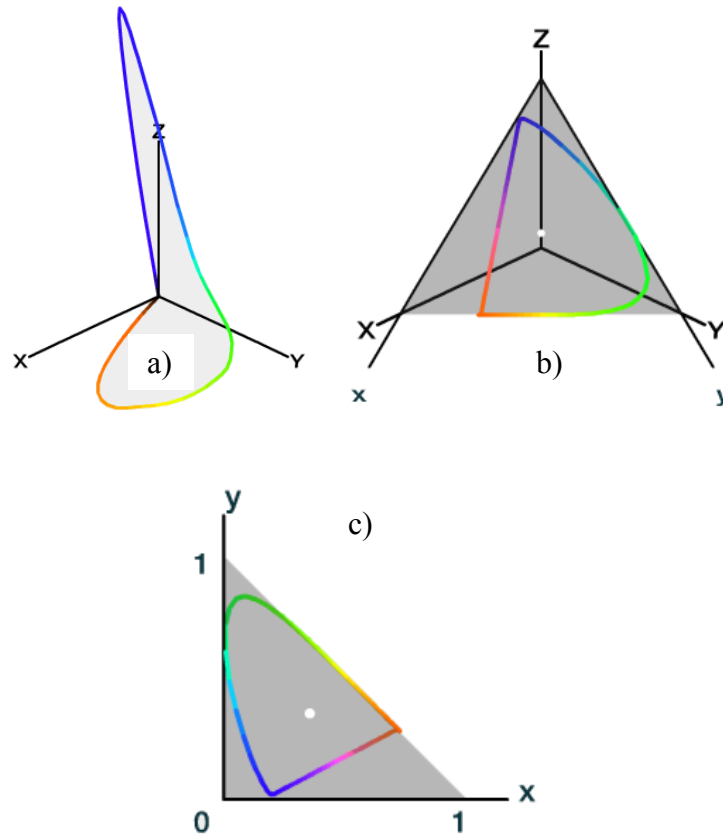
175

$$y = \frac{Y}{X + Y + Z} \tag{C3}$$

Fig. C3. a) A plot of a series of spectrally pure monochromatic colors plotted in three dimensions where the axes represent the tristimulus values (X, Y, Z). b) Plot of the projection of the points in XYZ space onto the $X + Y + Z =1$ plane, where the point of projection is the origin c) The plot in (b) aligned with the traditional x and y two-dimensional axis system, ensuring that the spectral locus is in the positive octant of XYZ color space. This produces the well know 1931 CIE chromaticity diagram. Reproduced from [3].

Since all colors now lie on a plane, chromaticity can be represented using only (x, y), rather than (X, Y, Z). If we align our viewing perspective to the traditional x and y two-dimensional axis system, and ensure that the spectral locus is in the positive octant of XYZ color space, we obtain the 1931 CIE chromaticity diagram (sown in Fig. C3c, and reproduced with more detail in Fig. C4). However, it must be kept in mind that to represent the brightness of a

given color on the chromaticity diagram, not only do the (x, y) coordinates need to be given but also one of the tristimulus values, usually the Y value, also must be specified (see Fig. C5).
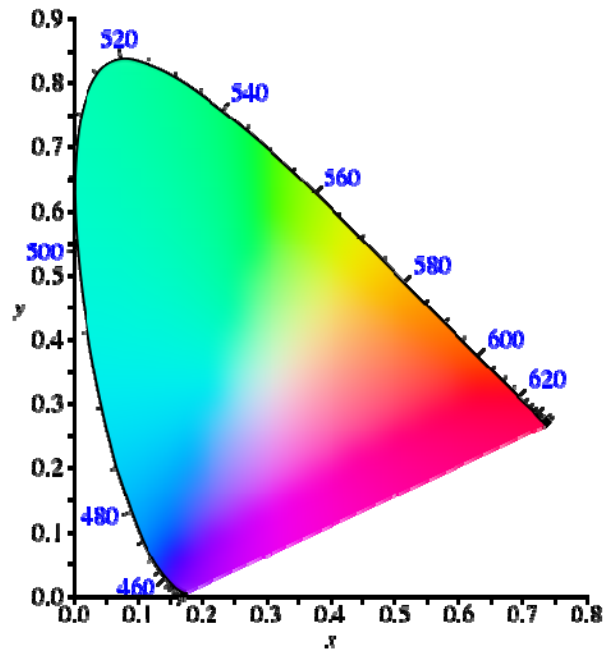

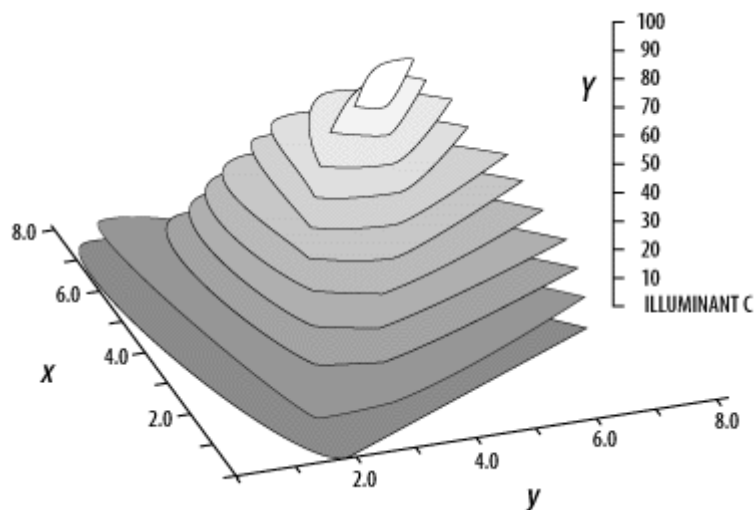
Fig. C4. 1931 CIE chromaticity diagram in greater detail.

Fig. C5. The brightness of a color is lost in the Chromaticity diagram. For this the (x, y) coordniates need to be given in addition to the tristimulus Y value. Reproduced from [4].

On the chromaticity diagram, colors of monochromatic light trace out a locus of points that looks like the top half horseshoe, with the violet end (400 nm) of the spectrum on the lower left and the red end (700 nm) of the spectrum on the lower right. The straight line connecting the violet end to the red end of the horseshoe represents colors that are a mixture of red and blue, and cannot be realized with monochromatic light. Less saturated colors appear in the interior of the figure with white at the center. The outer curved boundary is the spectral locus. The diagram represents all of the chromaticities visible to the average person. These are shown in color and this region is called the gamut of human vision.

If one chooses any two points of color on the chromaticity diagram, then all the colors that lie in a straight line between the two points can be formed by mixing these two colors. It can be seen that, given three real sources, these sources cannot cover the gamut of human vision. These lead to considerations for the design of RBG pixels in OLED displays to cover as broad of a gamut as possible.

C.2 Luminance Determination

Luminance is used to characterize the light emitted from OLED sources. Luminance is a photometric measure of the luminous intensity per unit area of light travelling in a given direction. The units for luminance are candela per square meter (cd/m^2). For reference, typical computer display emits between 50 and 300 cd/m^2.

The luminance measured in our detector setup as shown in Fig. 3.12 of Chapter 3 is given by:

$$L_v = \frac{V_{det}}{R \cdot R_{det}} \frac{\Phi_v'}{S_0} \frac{d^2}{A_{det}} \qquad (C4)$$

where V_{det} is the detected voltage [V] from the photodiode/amplifier detector circuit,

R Feedback resistor [Ω], R_{det} is the responsivity [A/W] of the photodiode detector, Φ_v is a luminous flux scaling factor [lm/W], S_0 is the OLED area [m^2], d is the distance between the OLED and the photodiode detector [m], and A_{det} is the area of the photodiode detector [m^2].

To derive this expression for the measured luminance of an OLED from a photodiode detector, we first start with the general definition of radiance (see Appendix B3),

$$L_{e,OLED} = \frac{d^2\Phi_{e,det}}{ds_0 d\Omega \cos\theta} \tag{C5}$$

where $ds_0 \cos\theta$ is the projected differential area of the OLED), Ω is the solid angle from the photodiode to the OLED and $\Phi_{e,det}$ is the radiant flux of the OLED measured by the detector in [W]. Now we turn to the photodiode which has an area of da (and a projected area of $da = a_0 \cos\psi$) and is located at a distance away from the OLED. If this distance is at least 10 times further away than the maximum dimension of the OLED, the differential solid angle as observed from the photodiode point-of-view can be approximated by

$$d\Omega \approx d\frac{da}{R^2} = \frac{da_0 \cos\psi}{R^2} \tag{C6}$$

Thus solving for $d^2\Phi_{e,det}$ we have

$$d^2\Phi_{e,det} = L_{e,OLED} \frac{ds_0 \cos\theta \, da_0 \cos\psi}{R^2} \tag{C7}$$

This expression can be integrated to obtain the total radiant flux [W] that falls on the detector.

$$\Phi_{e,det} = \int_{S_0} \int_{A_0} L_{e,OLED} \frac{ds_0 \cos\theta \, da_0 \cos\psi}{R^2} \tag{C8}$$

If we make the approximation the radiance of the OLED is constant over the area of the OLED we can pull out $L_{e,OLED}$ from the integral. Also if the source and the detector are facing one another then $\cos\theta = \cos\psi = 1$. Therefore, we can write

$$\Phi_{e,det} \approx \frac{L_{e,OLED}}{d^2} \int_{S_0} \int_{A_0} ds_0 \, da_0 = \frac{L_{e,OLED}}{d^2} S_0 A_0 \qquad (C9)$$

where S_0 is the total area of the OLED, and A_0 is the total area of the photodetector.

Turning now to the electrical properties of the photodetector, the spectral responsivity of the photodiode is given by

$$R_{det,\lambda}(\lambda) = \frac{I_{det,\lambda}(\lambda)}{\Phi_{det,\lambda}(\lambda)} \qquad (C\ 10)$$

where $I_{det,\lambda}$ is the measured photocurrent [A] at wavelength λ, $\Phi_{det,\lambda}$ is the spectral radiant flux [W/nm], and $R_{det,\lambda}$ is measured in [A/W-nm]. From this we can calculate the weighted detector response [A/W]

$$R_{det} = \int_{\lambda=380}^{780} R_{det,\lambda}(\lambda) \frac{I_{OLED,\lambda}(\lambda)}{\int_{\lambda=380}^{780} I_{OLED,\lambda}(\lambda')d\lambda'} \, d\lambda \qquad (C\ 11)$$

where $I_{OLED,\lambda}(\lambda)$ is the absolute spectral irradiance (or radiant flux density) in [W/m^2-nm]. This parameter then allows us to connect the spectral radiant flux of the detector $\Phi_{det,\lambda}$ to the current of the detector through the relationship

$$\Phi_{e,det} = \frac{I_{det}}{R_{det}} \qquad (C\ 12)$$

If we consider that

$$V_{det} = R I_{det} \qquad (C\ 13)$$

by Ohm's law, then

$$\Phi_{e,det} = \frac{I_{det}}{R_{det}} = \frac{V_{det}}{R_{det} R} \qquad (C\ 14)$$

Therefore,

$$L_v = \frac{\Phi_{e,det} \Phi'_v d^2}{S_0 A_0} = \left(\frac{V_{det}}{R_{det} R} \right) \Phi'_v \frac{d^2}{S_0 A_0} \qquad (C\ 15)$$

Where Φ_v' is the luminous flux scaling factor [lm/W] and is calculated by the formula

$$\Phi_v' = 683 \frac{lm}{W} \frac{\int_{380}^{780} V(\lambda) S_{OLED,\lambda}(\lambda)}{\int_{380}^{780} S_{OLED,\lambda}(\lambda)} d\lambda \qquad (C\ 16)$$

C.3 EQE Determination

  To measure the EQE parameter that was described in section 3.3.2 with our photodiode setup we first calculate the expected photon energy (eV) coming from the spectral irradiance (or radiant flux density) of the OLED spectrum at a fixed luminance. This is given by

$$\bar{E} = \frac{hc}{\langle \lambda \rangle} \qquad (C\ 17)$$

where $\langle \lambda \rangle$ is the expected value of wavelength of light from the OLED. Expected wavelength is a weighted average of all the wavelengths of visible light multiplied by each wavelength's contribution to the OLED absolute spectral irradiance $I_{OLED,\lambda}(\lambda)$.

$$\langle \lambda \rangle = \left(\frac{\int_{380}^{780} I_{OLED,\lambda} \lambda(\lambda)}{\int_{380}^{780} I_{OLED,\lambda}(\lambda)} \right) \qquad (C\ 18)$$

Hence the EQE can be given as

$$EQE = \frac{n_{ph}}{n_e} \times 100\% = \frac{\Phi_{OLED}/\bar{E}}{I/e} \times 100\% \qquad (C\ 19)$$

where Φ_{OLED} is the radiant flux of the OLED

$$EQE = hc \frac{\Phi_{OLED}}{I} \left(\frac{\int_{380}^{780} I_{OLED,\lambda}(\lambda)\,\lambda d\lambda}{\int_{380}^{780} I_{OLED,\lambda}(\lambda) d\lambda} \right) \times 100\% \qquad (C\ 20)$$

In practice, we calculate

$$L_v = \frac{\Phi_{e,det}\Phi_v' d^2}{S_0 A_0} = \left(\frac{V_{det}}{R_{det} R} \right) \Phi_v' \frac{d^2}{S_0 A_0} \qquad (C\ 21)$$

and

$$EQE = \frac{hc}{I} \frac{V_{det} d^2 \pi}{R_{det} RA_{det}} \frac{\sum_k \lambda_k I_{OLED,\lambda}(\lambda)}{\sum_k I_{OLED,\lambda}(\lambda)} \times 100\% \qquad (C\ 22)$$

C.4 Color Rendition Index (CRI) Determination

The color rendition index (CRI) of a light source is a measure of the ability of that source to faithfully reproduce the colors of various objects as compared with a defined source or a natural light source such as the sun [5]. For reference, the CRI perfect blackbody radiator is 100. Incandescent lamps have CRI values that are close to 100 as well. Fluorescent lights range from about 50 for the basic types, up to about 90 for the most advanced tri-phosphor types. Typical LEDs have a CRI of around 80, while some new, specialty LEDs have achieved up to 98 CRI.

A flowchart of the way to calculate the CRI is shown in Fig. C6. The CRI is determined by comparing the color rendering of the test source to that of a black body radiator for sources with correlated color temperatures (CCT) less than 5000 K. The color temperature of a light source is the temperature of a Planckian radiator having the same chromaticity. If the light source has coordinates that are not on the Planckian locus, then one can only define a correlated color temperature of the closest Planckian radiator.
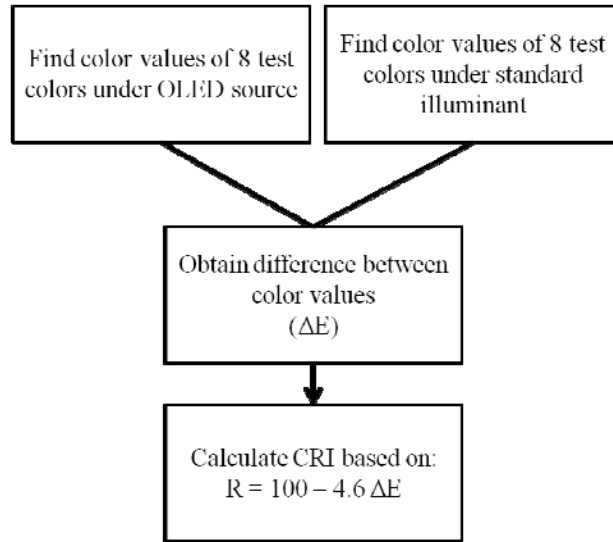
Fig. C6. An overview of the method to calculate the CRI coordinates of a given illumination source, such as a white OLED.

A procedure to determine the CRI will now be discussed [6]. As a first step, one calculates the chromaticity coordinates of the test source in the CIE 1960 color space and covert them into the (u, v) coordinates (which define an alternate two-dimensional color-space) from the (x, y) system. This can be done through the use of the following equations [7]

$$u = \frac{4x}{12y - 2x + 3} \qquad\qquad (C\ 23)$$

$$v = \frac{6y}{12y - 2x + 3} \qquad\qquad (C\ 24)$$

Next one must find the CCT of the test source by finding the closest point to the Planckian locus on the (u, v) chromaticity diagram. The Planckian locus is the path that the color of an incandescent black body would take in a particular chromaticity space as the blackbody temperature changes (see Fig. C7) [8]. It can be determined by substituting into equations for the tristimulus values for a given temperature $T = t$

$$X_t = \int_{380}^{480} I(\lambda, T)\bar{x}(\lambda)\,d\lambda, \; Y_t = \int_{380}^{480} I(\lambda, T)\,\bar{y}(\lambda)d\lambda \,, Z_t = \int_{380}^{480} I(\lambda, T)\bar{z}(\lambda)\,d\lambda \qquad (C\ 25)$$

where $\bar{x}(\lambda)$, $\bar{y}(\lambda)$, and $\bar{z}(\lambda)$ are the color matching functions, and the black body spectral

radiance is given by Planck's law,

$$I(\lambda, T) = \frac{2\pi hc^2}{\lambda^2}\left(e^{\frac{hc}{\lambda kT}} - 1\right)^{-1} \qquad (C\ 26)$$

and then finding the corresponding x and y coordinates (x_t, y_t)

$$x_t = \frac{X_t}{X_t + Y_t + Z_t} \qquad (C\ 27)$$

$$y_t = \frac{Y_t}{X_t + Y_t + Z_t} \qquad (C\ 28)$$

and finally converting to the corresponding $(u_t, v_{t)}$. This calculation can be approximated in

many tabulated sources, derived this cubic approximation

$$CCT(x, y) = -449n^3 + 3525n^2 - 6823.3n + 5520.33 \qquad (C\ 29)$$

where

$$n = \frac{x - x_e}{y - y_e} \qquad (C\ 30)$$

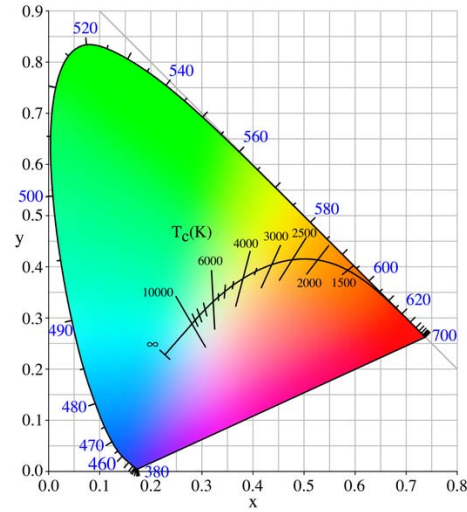where $(x_e, y_e) = (0.3320, 0.1858)$ [9].

Fig. C7. The 1931 chromaticity diagram, showing the Planckian locus for ideal blackbody radiators.

Next if the test source CCT < 5000 K, a black body for reference source, otherwise use CIE standard illuminant D. This standard illuminant is a theoretical source of visible light with a spectral power distribution which is published [10]. The D series of illuminants are constructed to represent natural daylight (see Fig. C8).
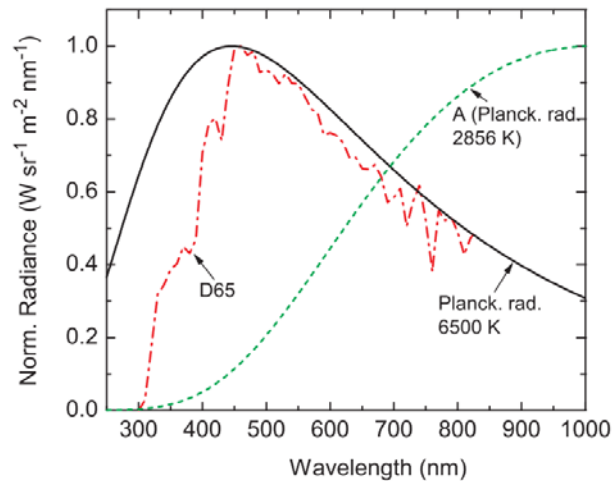

Fig. C8. The D series of illuminants are constructed to represent natural daylight, as can be seen the red curve. It closely matches a blackbody Planckian radiator at 6500 K. Reproduced from [11].

185

Since the CRI is only defined for light sources that are approximately white, it must be ascertained that the chromaticity distance (DC) of the test source to the Planckian locus is under 5.4×10^{-3} in the CIE 1960 UCS color space, where

$$DC = \Delta_{uv} = \sqrt{(u_r - u_t)^2 + (v_r - v_t)^2} \qquad (C\ 31)$$

Next one illuminates eight standard samples alternately using both sources with the spectra shown in Fig. C9.
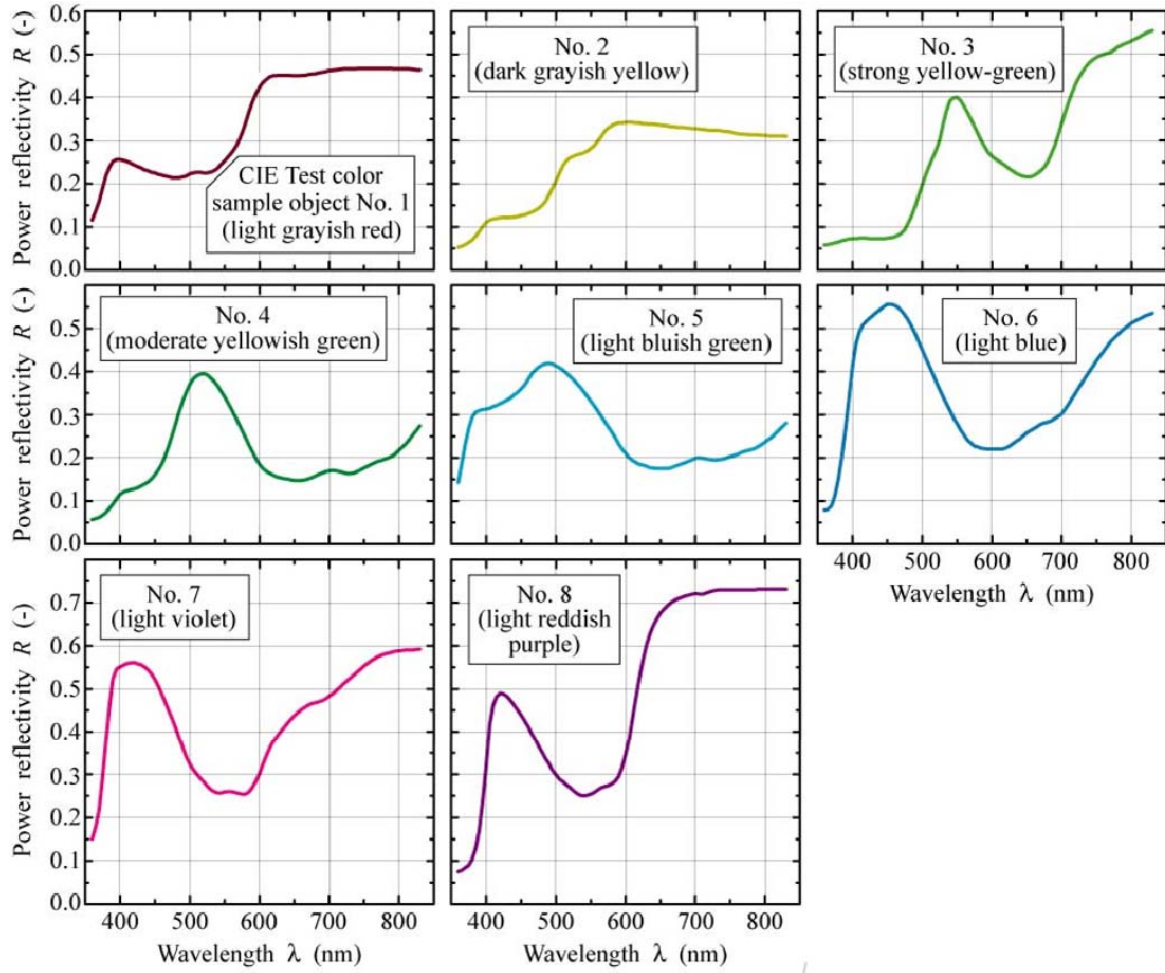

Fig. C9. The eight standard CIE standard samples that must be illuminated by the source. Reproduced from [5].

Then one finds the coordinates of the light reflected by each sample in the CIE 1964 color space by chromatically adapting each coordinate by a so-called von Kries transform [10] to

find the corresponding color $(u_{c,i}, v_{c,i})$ for each sample in 1964 space. Chromatic adaptation accounts for a distortion in the human visual system where the peak sensitivity of the human eye shifts toward the blue end of the spectrum at lower light levels. To correct this source of error, a gain is applied to each of the human cone cell spectral sensitivity responses so as to keep the adapted appearance of the reference white constant. Mathematically it can be achieved by calculating the parameters $u_{c,i}$ and $v_{c,i}$ [6]

$$u_{c,i} = \frac{10.872 + 0.404 \left(^{C_t}/_{c_t}\right) c_{t,i} - 4 \left(^{d_r}/_{d_t}\right) d_{t,i}}{16.518 + 1.481 \left(^{C_t}/_{c_t}\right) c_{t,i} - \left(^{d_r}/_{d_t}\right) d_{t,i}} \qquad (C\ 32)$$

$$v_{c,i} = \frac{5.520}{16.518 + 1.481 \left(^{C_t}/_{c_t}\right) c_{t,i} - \left(^{d_r}/_{d_t}\right) d_{t,i}} \qquad (C\ 33)$$

where (t, i) refer to the inner product of the test illuminant spectrum and the spectral reflexivity of sample i and

$$c = \frac{4.0 - u - 10.0v}{v} \qquad (C\ 34)$$

$$d = \frac{1.708v - 1.481u + 0.404}{v} \qquad (C\ 35)$$

Now, for each sample, one must calculate the distance ΔE_i between the pair of coordinates $(u_{c,i}, v_{c,i})$ and (u, v):

$$\Delta E_i = \sqrt{\left(u_{c,i} - u\right)^2 + \left(v_{c,i} - v\right)^2} \qquad (C\ 36)$$

This allows for the calculation of the particular CRI R_i for each sample using the formula [12]

$$R_i = 100 - 4.6\Delta E_i \qquad (C\ 37)$$

Finally, the general CRI (R_a) can then be calculated by the arithmetic mean of the particular

CRIs:

$$R_a = \frac{1}{n}\sum_{i=1}^{n} R_i \qquad\qquad (C\ 38)$$

C.5 References

[1] CIE Standard Observers, 2013.
[2] G.A. Klein, Industrial Color Physics, Springer, 2010.
[3] K. Dektar, M. Levoy, Chromaticity diagrams, 2010.
[4] A.S. Incorporated., Technical Guides: Color Models, 2000.
[5] E.F. Schubert, Light-Emitting Diodes, Cambridge University Press, 2006.
[6] I. International Commission on, Method of Measuring and Specifying Colour Rendering Properties of Light Sources: CIE 13.3-1995, Commission internationale de l'éclairage, CIE Central Bureau, 1995.
[7] D.L. Macadam, Projective Transformations of I. C. I. Color Specifications, J. Opt. Soc. Am., 27 (1937) 294-297.
[8] J.P. Dakin, R.G.W. Brown, Handbook of Optoelectronics (Two-Volume Set), Taylor & Francis, 2010.
[9] C.S. McCamy, Correlated color temperature as an explicit function of chromaticity coordinates, Color Research & Application, 17 (1992) 142-144.
[10] H.R. Kang, Computational Color Technology, Society of Photo Optical, 2006.
[11] Schwartz, G. "Novel Concepts for High-Effciency White Organic Light-Emitting Diodes," TU Dresden (Dissertation) (2007).
[12] J. Schanda, The concept of colour rendering revisited, Society for Imaging Science and Technology, pp. 37-41.